Universität Bielefeld
Fakultät für Physik

Gas permeation of carbon nanomembranes

Dissertation submitted in partial fulfillment
of the requirements for the degree of
Doktor der Naturwissenschaften
submitted by M.Sc.

Vahe Chinaryan

Bielefeld, Germany
August 2017

Declaration:

I hereby declare that the work in this thesis is my original work. None but the indicated resources were used.

Committee:

1. Prof. Dr. Armin Gölzhäuser
2. Prof. Dr. Dario Anselmetti
3. Prof. Dr. Peter Reimann
4. Prof. Dr. Karl-Josef Dietz

Printed on non-ageing paper ISO 9706

Table of contents

Chapter1

Introduction to the basics of membrane gas separation

1.1 Introduction to membrane separation

Since the beginning of the twenty-first century the fields of diffusion, sorption and permeation are of great interest due to an essential role in applications in several important areas of engineering and industry. These applications include protective coatings, such as paints and varnishes, electronic devices and cable materials, packaging materials for foods and vegetables, biomedical devices, filtration of liquids, gas separation, etc. Among these phenomena, transport studies are of great importance for problems, such as designing a barrier material for transporting liquids and gases [1].

Recently, advanced technologies with the combination of progressive economics have resulted in membrane production, which opens a new era in the commercial use of membranes for liquid and gas separations. The advantages of membrane separation over conventional process consists of reduced capital cost, lower energy consumption, smaller size and light weight, lower installation costs and simplified operations. Membrane separation techniques have already been used in industrial applications, such as desalination of brine, salt manufacturing from sea-water, and oxygen enriched air [1].

Undoubtedly, one of the main reasons for the great interest in the field of permeation, sorption, and diffusion is global warming, which is one of the world's major environmental issues. The desire for complete prevention of anthropological global warming is one of the biggest global problems, which seems to be impossible to overcome. Nevertheless, it is possible to soften the impacts of mankind on global warming. One of the ways to mitigate global warming is through the reduction of greenhouse gas emissions via the capture of CO_2 from flue gases followed by underground sequestration**.** Flue gas is the gas exiting to the atmosphere from a fireplace, oven, furnace, boiler or steam generator. Flue gas is also the combustion exhaust gas produced by power plants. It usually consists of mostly N_2 that is derived from the combustion of air, CO_2 and water vapor, as well as, excess O_2. The CO_2 gas emitted from power plants is considered to have a significant impact to the global warming of climate. In order to decrease the effect of CO_2 on global warming, CO_2 can be captured in flue gas and sequestered underground. The conventional process to capture CO_2 is by reversible solvent absorption that is energy intensive and requires high heating utility in the stripper.

Membrane technology is an attractive and competitive alternative to conventional absorption technology [2].

1.2 Historical review of gas separation membranes

Membrane separation is a well-established and proven technology, widely used in numerous industrial, medical, and biological applications [3]. A variety of materials are used in membranes including polymers, inorganic crystals, and carbon materials of different origins [4]. Among all separation processes membrane gas separation plays a crucial role in modern life. It prevents pollution of nature and avoids increase of greenhouse gases in natural gas production, which itself has an effect on climate change, among other benefits.

The origin of membrane materials for gaseous separations can be dated back to nearly two centuries. It is considered that the foundation of gas separation was laid by Thomas Graham, a Scottish chemist and father of membrane science, who studied diffusion of gases and liquids through various media. He discovered that certain substances, such as glue, gelatin, and starch pass through a barrier more slowly than others, such as inorganic salts, leading to establishing a distinction between the two types of particles made by the separating media or barrier [5]. In 1855, Fick, studied gas transport through a nitrocellulose membrane and postulated the concept of diffusion, which is well-known as “Fick's first law”, a quantitative description of material transport through barriers. Through the nineteenth and early twentieth centuries, membranes had no industrial or commercial uses, but were used as laboratory tools to develop physical and chemical theories.

The breakthrough in membrane separation came in the early 1960s, when Loeb and Sourirajan developed defect-free, high-flux, anisotropic reverse-osmosis membranes, which consist of ultrathin, selective surface film on a much thicker, but much more permeable microporous support that provides the mechanical strength. It had a big impact on the development of the gas separation industry. Since then, membranes for gas separation for large industrial application have been introduced to the market. First one was Prism membrane by Permea (Monsanto) for hydrogen separation from the purge gas

stream of ammonia plants. Within a few years, Dow was producing systems to separate nitrogen from air, and Cynara and Separex were producing systems to separate carbon dioxide from natural gas. Milestones in the development of the gas separation industry are presented in Figure 1 [5].

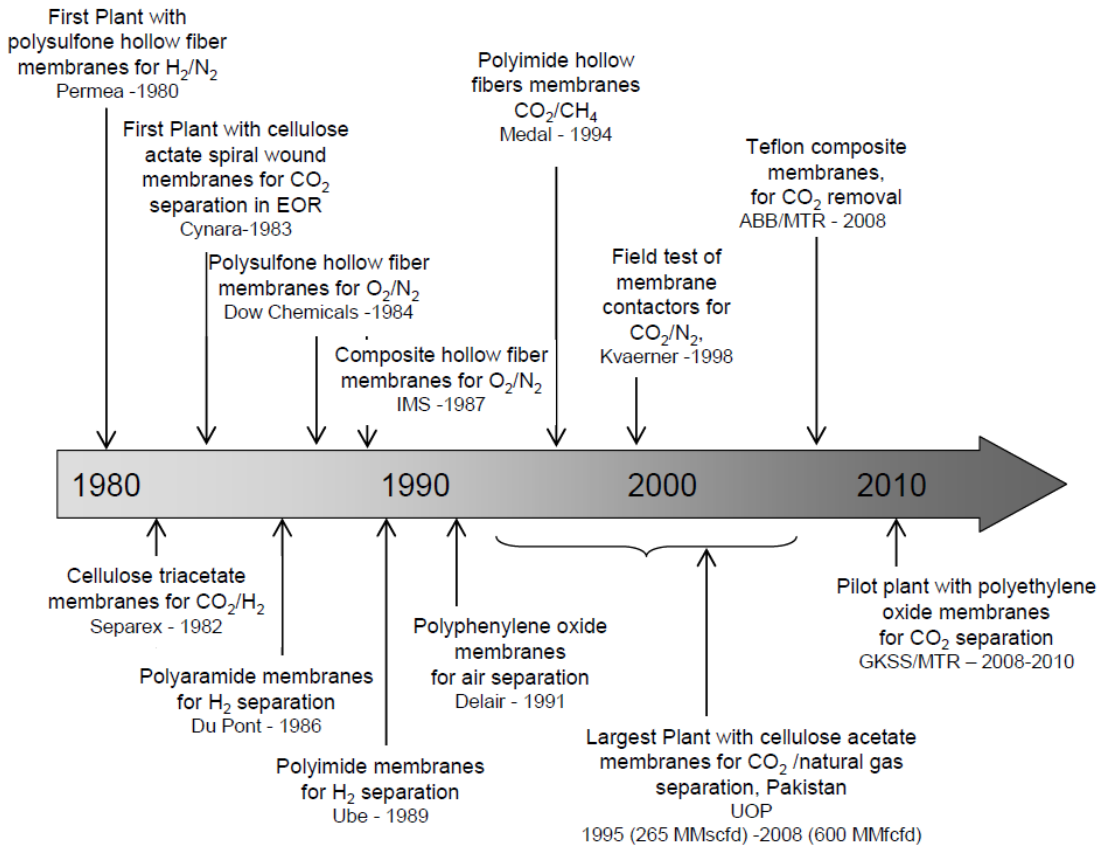

Fig.1 Milestones in the industrial application of membrane gas separation systems [5].

1.3 Membrane material

Gases can be effectively separated by synthetic membranes. Most of the commercially utilized synthetic membranes in the separation industry are made of polymeric structures. Polymeric membranes lead the membrane separation industry market because they are very competitive in performance and economics. Membranes are made of variety of polymers such as polyethylene, polyamides, polyimides, cellulose acetate, polysulfone, polydimethylsiloxane, etc.

1.4 Mechanisms of membrane gas separation

Gas separation membranes can be classified into two types: porous and non-porous membranes. Based on the type of membrane, the mechanism of gas permeation, therefore gas separation, is different.

1.4.1 Mechanisms of porous membranes

Porous membranes typically have big voids with randomly distributed interconnected pores significantly larger than the molecular diameters of gases passing through them. Mechanisms of gas permeation differ based on the pore size. Separation of solutes by porous membranes is mainly a function of molecular size and pore size distribution [6].

Poiseuille flow

In general, when pores are much larger than gas molecules, viscous flow occurs, thus separation doesn't occur (Fig.2a).

Knudsen diffusion

Knudsen diffusion dominates in the membrane for gas separation when pore diameter is smaller than 50 nm, which means free path of gases becomes bigger than the pore size (Fig.2b). Gas molecules interact with the pore walls much more frequently than colliding with one another. As there is less number of collisions among gas molecules than pore walls, each molecule will move independently of others. Therefore, separation takes place due to differences in velocities of gas molecules, which itself depends on molecular weight of the gases. The driving force for Knudsen diffusion is the partial pressure gradient, which is equivalent to the total pressure gradient in a single gas system. Transport of molecules, particularly gases through membranes, is described by Fick's first law of diffusion:

$$\mathrm{J} = -\mathrm{D}\frac{\partial \mathrm{c}}{\partial \mathrm{x}} \tag{1}$$

where J is the flow rate of transfer of molecules through membrane, c is the concentration of molecules, and D is the diffusion coefficient, which is the measure of mobility of

molecules. Flow rate of gases in Knudsen diffusion is proportional to the velocity of the gas molecule and inversely proportional to the square root of the molecular weight of the gas molecule:

$$D \sim -\frac{d}{3}\sqrt{\frac{8\,R\,T}{\pi\,M}} \qquad (2)$$

M is molecular weight, T is temperature, R is gas constant, and d is pore diameter. Thus, permeation of gases decreases when the molecular weight is increased [6] (Fig.3). Knudsen diffusion membranes have been used to separate gas isotopes that are difficult to separate by other methods, for example tritium from hydrogen, $C^{12}H_4$ from $C^{14}H_4$ and most importantly $U^{235}F_6$ from $U^{238}F_6$.

Capillary condensation

Gas separation can take place due to condensation of some component of a mixture of the gases, with the exclusion of the others, and subsequent transport of the condensed molecules across the pore (Fig.2c).

Surface diffusion

Adsorption of more strongly absorbed components of the gas mixture onto the pore walls and subsequent surface diffusion across the pore walls can facilitate separation of the gases (Fig.2d).

Molecular sieving:

When the pore diameter of a membrane is between those of the gas molecules to be separated, only the smaller gas can permeate and perfect separation will be achieved. Thereby, separation of the mixture of the gases via molecular sieving is based on the size exclusion (Fig.2e).

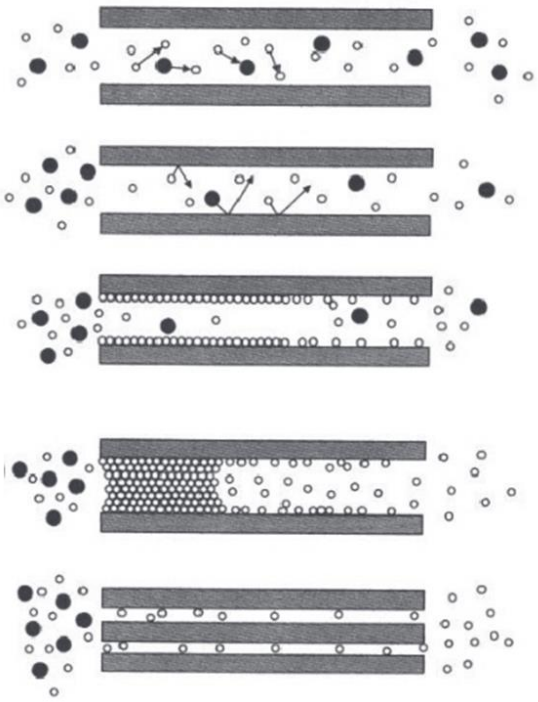

a)
Viscous flow (Poiseuille): pore size > 50 nm
Mean free path is bigger than pore size

b)
Knudsen diffusion: pore size <50 nm
Mean free path is bigger than pore size

d)
Surface diffusion:
Adsorption and diffusion

c)
Capillary condensation:

e)
Molecular sieving: pore size < 0.5 nm
Size exclusion

Fig.2 Schematic representation of mechanisms for gas permeation in porous membranes [6].

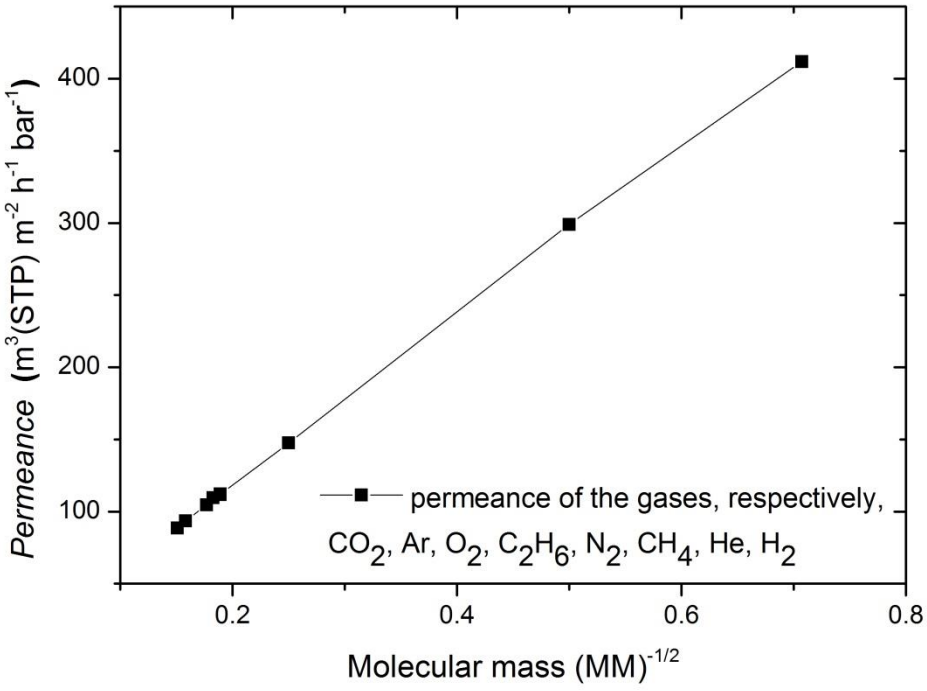

Fig.3 Example of Knudsen diffusion in the case of PAN porous membrane. It indicates that permeation is inversely proportional tothe mass of thepermeate molecule (the heaviest gas is CO_2, the lightest is H_2).

1.4.2 Mechanism of non-porous, dense membranes: Solution-diffusion mechanism

The mechanism of membrane gas separation for non-porous membranes is completely different compared with porous membranes. Non-porous membranes consist of a dense film through which permeants pass through by diffusion under the driving force of pressure, concentration, or electrical potential gradient. The separation of gas mixture is related directly to their transport rate within the membrane, which is determined by their diffusivity and solubility in the membrane material [5]. Thus, non-porous membranes can separate gases of similar size if their concentration in the membrane differs significantly.

The mechanism, which operates in non-porous membranes for gas separation is solution-diffusion. Solution-diffusion mechanism can be described within three steps: gas adsorbs at the interface of the membrane; it diffuses (solubility) through the membrane; and finally, it desorbs from the permeate side of the membrane (Fig.4).

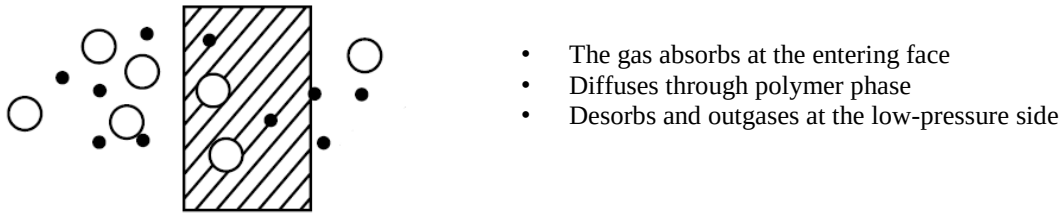

Fig.4 Schematic representation of solution-diffusion mechanism.

Diffusion, the basis of solution-diffusion model, is a process by which gas molecules permeate through material due to driving forces. Fick's law is the simplest description of gas diffusion through a non-porous structure.

$$\mathrm{J} = -\mathrm{D}\frac{\partial \mathrm{c}}{\partial \mathrm{x}} \tag{3}$$

where J is flow rate through membrane, D is diffusion coefficient and driving force, $\frac{\partial \mathrm{c}}{\partial \mathrm{x}}$ is the concentration gradient across the membrane. Concentration of gases can be described by Henry's law, which states that a linear relationship exists between the concentration inside the membrane and partial pressure of the gas outside the membrane:

$$c = S\,p \tag{4}$$

where c is concentration of the gases, p is partial pressure of the gas, and S is solubility of the gas passing through the membrane. Substituting Eq.4 into Eq.3 yields

$$J = -P\frac{dp}{dx} \tag{5}$$

where P is the permeability coefficient: the product of the coefficients of solubility and diffusivity:

$$P = S\,D \tag{6}$$

Permeability is the main parameter characterizing gas permeation through dense membranes. In another word, selectivity of two gases through the dense membrane can be defined by the ratio of the permeability of two gases.

$$\alpha_{ij} = \frac{D_i}{D_j}\frac{S_i}{S_j} \tag{7}$$

Most of the dense membranes used today in gas separation industry are polymeric membranes. Transport of the gases varies from one polymer to another. Transport properties depend on free volume and on segmental mobility of polymer chains. Segmental mobility itself depends on the crystallinity of the polymer, the degree of crosslinking of the polymer, and packing defects. Free volume is an intrinsic property of the polymer matrix and arises from the gaps left between entangled polymer chains. Free volume in the membrane can be described also as a tiny space between polymer chains caused by thermal motion of the polymer molecules [1].

In all polymer materials, the diffusion coefficient decreases with increasing molecular size because large molecules interact with more segments of the polymer chain than do small ones [5]. If polymers operate below their glass transition temperature, they are glassy polymers. If the material is below the glass transition temperature, polymer chains are essentially fixed and do not rotate. The glassy polymers are tough and rigid. When the polymer material operates above glass transition temperature, it is called rubbery polymer and the segments of the rubbery polymer chains have sufficient thermal energy to allow limited rotation around the chain backbone. This motion changes the mechanical properties of the polymer dramatically. Mobility of gases, as characterized by their

diffusion coefficients, differs significantly in rubbers and glasses, as illustrated in Figure 5 [5].

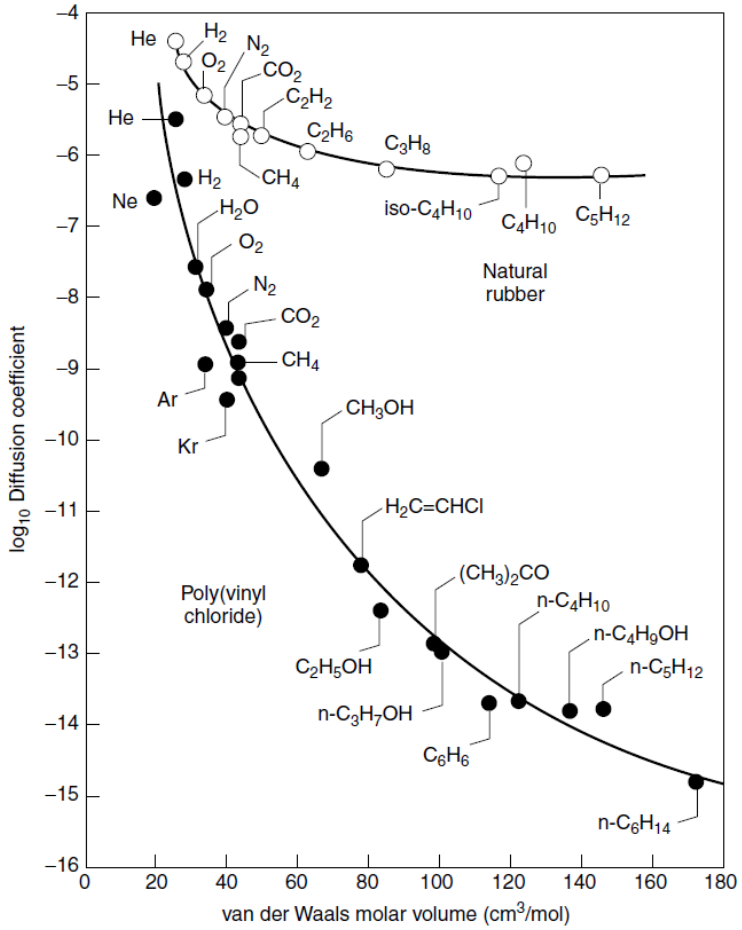

Fig.5 Diffusion coefficient as a function of molar volume for a variety of permeants in natural rubber and in poly-(vinyl-chloride), a glassy polymer [5].

As can be seen from Figure 5, diffusion coefficients in glassy materials decrease much more rapidly with increasing permeate size than diffusion coefficients in rubbers. Regarding solubility coefficient of gases and vapors, the opposite effect was observed. Solubility increases with increasing molecular diameter, as large molecules are normally more condensable than smaller ones and, therefore, soluble in the polymers, see Figure 6 [5]. However, the difference between the sorption coefficients of permeants in rubbery and glassy polymers is far less marked than the difference in the diffusion coefficients.

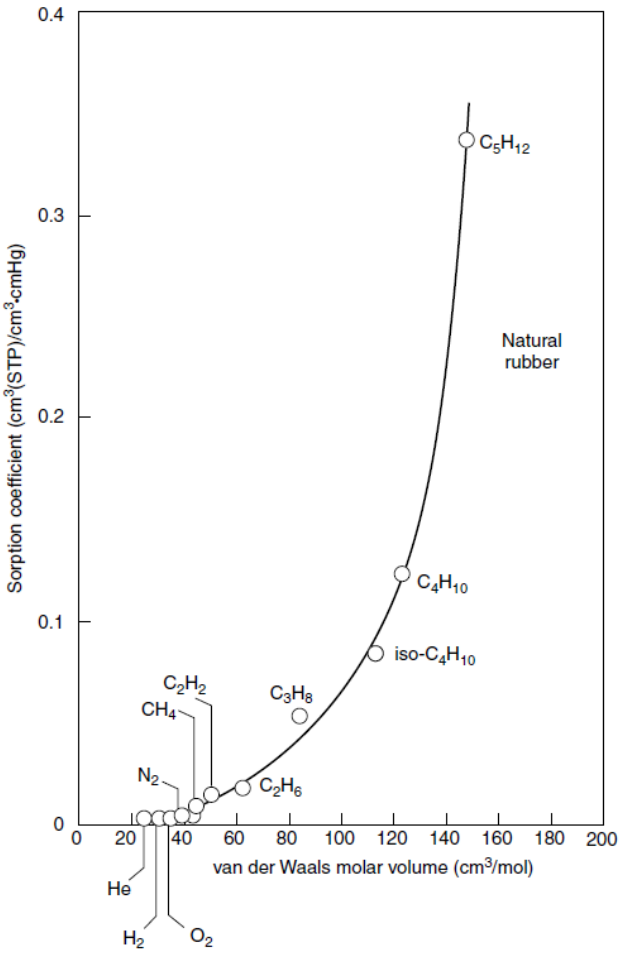

Fig.6 Gas solubility coefficient as a function of molar volume for natural rubber membranes. Larger permeants are more condensable and have higher solubility coefficients [5].

Abovementioned arguments show that the balance between solubility and diffusivity in Eq.6 differs for glassy and rubbery polymers. In glassy polymers, the diffusion term is usually dominant, which means permeability falls with increasing permeate size. In rubbery polymers, the solubility is usually dominant, therefore permeability increases with increasing permeate size, and larger molecules permeate preferentially (Fig.7) [5].

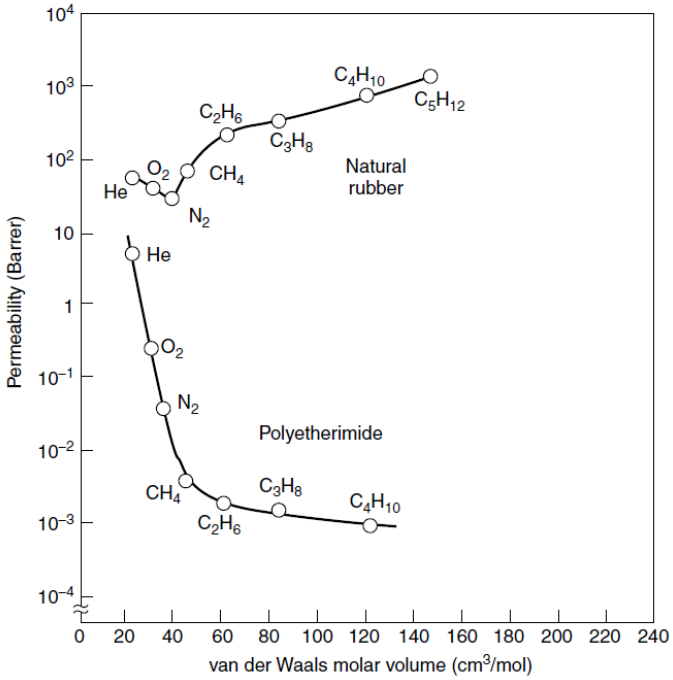

Fig.7 Permeability as a function of molar volume for a rubbery and a glassy polymer, illustrating the different balance between sorption and diffusion in these polymer types [5].

The results in Figure 7 indicate that glassy polymers are preferred for separation of small gases and rubbery polymers are preferred for separation of organic vapors.

There is a strong inverse relation between flux and selectivity. Membranes with higher selectivity have lower permeability [5]. It was first demonstrated by Robeson, who showed that there is a so called "upper bound" for polymeric membranes from different materials. It shows a trade-off between permeability and selectivity of membrane materials. This dependence also illustrates that during the last decades there was a shift to higher values for the so called "upper bound" (see Fig.8). Similar shifts in the upper bound were also achieved for other gas pairs [7].

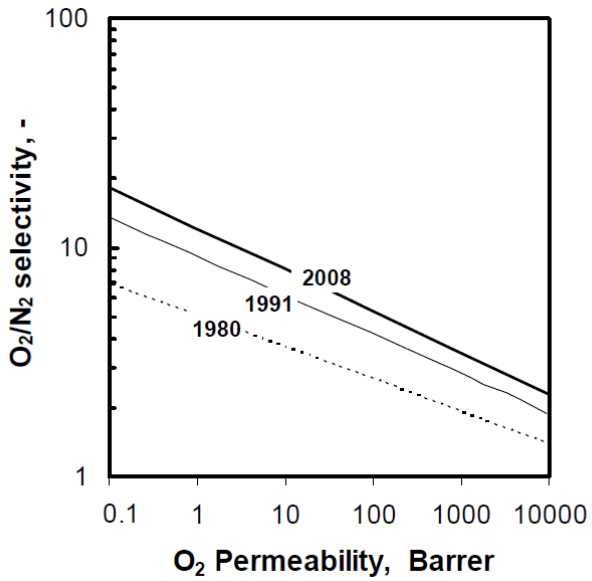

Fig.8 Time evolution of the upper bound for O_2/ N_2 separation [7].

Permeability is a material's property that changes consistently with thickness. Nevertheless, when the thickness of the membrane is unknown, permeance is used, which is the flux per unit pressure difference between the two sides of the membrane.

1.5 Anisotropic membranes

Membrane gas separation processes need high selectivity and high gas fluxes for economic reasons. In order to satisfy both requirements, particularly high fluxes, the membrane should be as thin as possible, since the transport rate of a species through a membrane is inversely proportional to the membrane thickness. For this reason a method

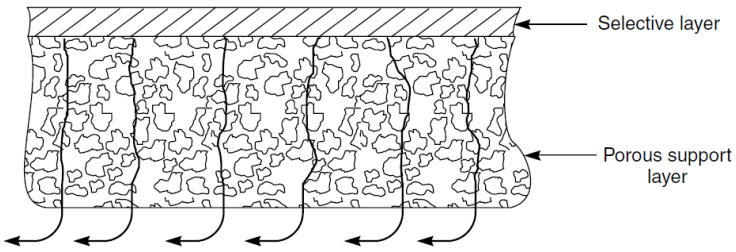

Fig.9 Thin-film composite membrane formed by coating a thin layer of a selective polymer on a microporous support that provides mechanical strength.

was developed at the 1960's of last century for fabrication of anisotropic membranes. The idea is to have a highly selective thin layer, which is supported by a highly permeable porous support layer (Fig.9). In thin-film anisotropic composite membranes, layers are usually made from different polymers. Separation properties and permeation rate are defined exclusively by surface thin layer. The porous support layer functions as mechanical support. The advantages of the higher fluxes provided by anisotropic membranes are so great that almost all commercial processes use such membranes [5].

Chapter 2

Introduction to carbon nanomembranes (CNMs)

2.1 2D materials and CNMs

In the last 50 years, the development of technology has achieved miniaturization of devices. The main benefits of that are the reduction of cost, weight, size, and enhancement of performance of those devices. For membrane gas separation, the material flow through a membrane is restricted by the thickness of the membrane. Therefore, in order to obtain high gas fluxes and enhance selectivity of gases through separation media with a precisely controlled pore sizes, two-dimensional (2D) materials can be employed as a membrane for gas separation.

2D nanomembranes, with a thickness below few nm and pores tuned to act as molecular sieves, are predicted to be ideal separation membranes with many advantages over bulk membranes [14]. The main advantage is comparatively high permeance in comparison with bulk membranes due to the thickness. Extremely thin carbon-based nanomembranes are considered to be ideal separation media for gas and chemical purification [15].

Although thin 2D materials might have a crucial role in gas flow rate due to thickness, they should be mechanically stable, stiff and able to resist stress caused by pressure and thermal changes. Graphene is one of the examples of such 2D material and can be employed as size-selective membrane for gas separation. Nevertheless, there are drawbacks in utilizing graphene as a membrane. Graphene is chemically inert and, thus, hard to be functionalized. Additionally, pristine single layer graphene is impermeable to all gases [8-10]. Therefore, pores should be induced into graphene sheets for permeation. Thus, several attempts were reported to use graphene-based materials as a separation barrier. For example, small pores were generated to graphene sheets by ultraviolet-induced oxidative etching, which resulted in a significant rise of the selectivity of hydrogen over nitrogen, as well as, methane [11]. Moreover, preparation of ultrathin graphene oxide (GO) membranes by facile filtration process was reported, with thickness approaching 1.8 nm. These membranes showed mixture separation selectivity as high as 3400 and 900 for H_2/CO_2 and H_2/N_2 mixtures, respectively, through selective structural defects on GO [12]. Another example is the fabrication of large area graphene sheets of about 100 mm^2 by chemical vapor deposition. A combination of pressure-driven and diffusive transport measurements provides evidence of size-selective transport. It reveals that graphene sheets have pores with diameters ranging from 1 to 15 nm. The results

demonstrated that it is possible to achieve selective molecular transport through macroscopic areas of single sheets of CVD graphene [13].

Another promising approach to fabricating functional 2D nanomembranes is to exploit the self-assembly of molecules. Highly-ordered self-assembled monolayers (SAMs) provide a molecular-thickness limit in 2D materials, which has a thickness of only one molecule, particularly the length of the precursor-molecule. Mechanical stability and properties of 2D materials can be enhanced by modification of SAMs or by changing precursor–molecules. The mechanical stability, however, can be enhanced by cross-linking a monolayer, which was first described by Gee in 1935 [16, 17]. SAMs can have particular spatial arrangement, which can be exploited to induce pores in a nanosheet to improve gas selectivity.

The carbon nanomembranes (CNMs) fabricated by self-assembly of aromatic molecules have mechanical stability, tunable optical properties, and has been already tested for gas permeation [18]. As shown in the work of Min Ai et al., the CNMs made of NBPT and BPT precursor molecules were examined for single gas permeation. The XPS and AFM investigations show that NBPT- and BPT-CNMs are successfully transferred onto the PDMS-TFC support, and after transfer the root mean square (RMS) roughness of PDMS-TFC decreases with increasing number of CNM layers on bare PDMS-TFC. It was discovered that after transfer of CNM on PFMS-TFC, the ideal gas selectivity increases towards small gas molecules, which is consistent with molecular sieve-like properties of CNMs. In the case of multilayer CNMs, it was proposed that additional lateral diffusion may be involved in between individual CNMs. Lateral diffusion of gas molecules may be described by Knudsen-like diffusion or by condensation and surface flow of gas molecules among CNMs. The results obtained for single and three-layer NBPT- and BPT-CNM showed almost identical outcomes (Fig.10). The only difference between these two CNM types is the amino groups on the upper part of each NBPT-CNM. These groups do not exist in BPT-CNM. It is notable that the CNM permeance for CO_2 is independent of the presence of amino groups. This indicates that no facilitated gas transport takes place across the CNMs [18].

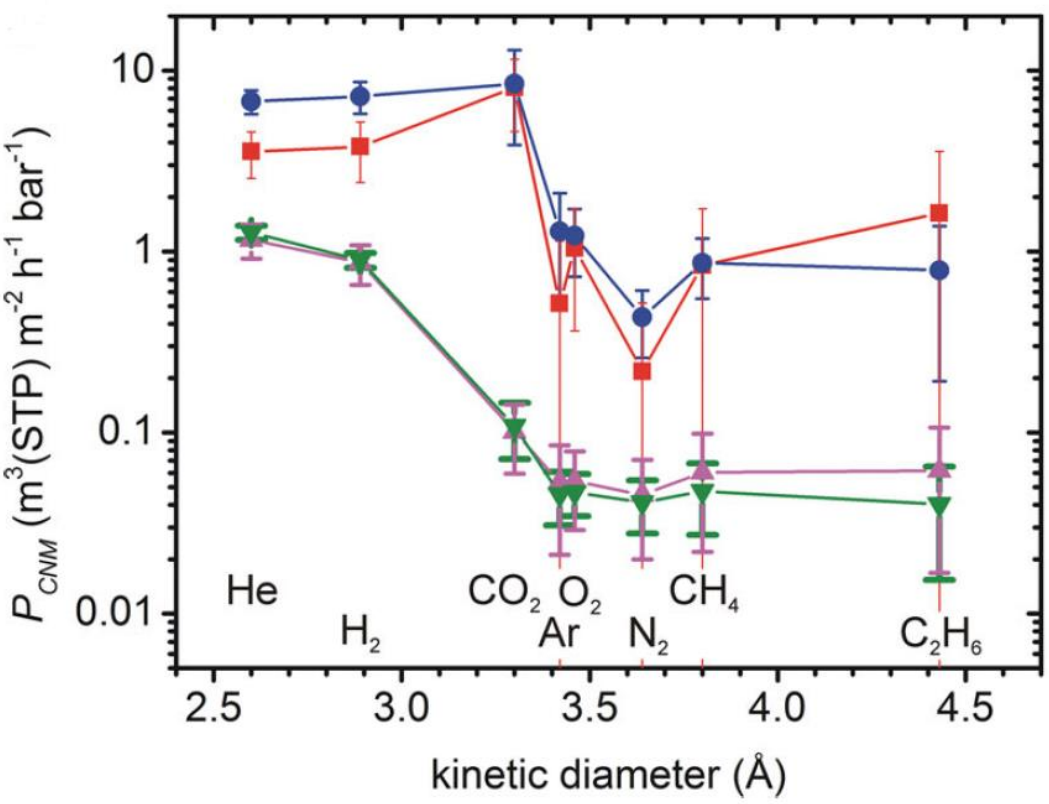

Fig.10 Intrinsic permeances of single- and three-layer NBPT- and BPT-CNM in relation to the kinetic diameter of the gases [18].

Taking into consideration properties of SAMs, CNMs, and preliminary results on gas permeation for NBPT- and BPT-CNM, different types of CNMs will be examined for gas permeation and will be modified to increase gas selectivity.

2.2 Self-assembled monolayers (SAMs)

Bare surfaces of metals and metal oxides tend to adsorb organic materials because these adsorbates lower the free energy of the interface between the metal or metal oxide and the ambient environment [19]. These adsorbates also alter interfacial properties and can have a significant influence on the stability of nanostructures of metals and metal oxides. Self-assembled monolayers are organic assemblies that are formed due to absorption of organic molecules onto the surface of metals and metal oxides from solution or the gas phase. Highly-ordered self-assembled monolayers can be formed by exploiting the self-assembly of molecules from amphiphilic molecules on a solid substrate [20-22]. These

molecules are chemically bounded on a solid surface via weak intermolecular interactions between the chemisorbed molecules. The molecules that form SAMs consist of three parts, schematically depicted in Figure 11: (a) a head functional group, which can be chemically absorbed on a metal substrate and has high affinity for the surface, (b) a terminal functional group, which determines the surface properties of SAMs, (c) in between there is a molecular backbone, so called spacer, which provides a well-defined thickness, mechanical stability, electronic conductivity, and optical properties. So far, many different SAMs have been prepared and investigated. The assembly of alkanethiol molecules on metal are apparently the most studied ones [23-37]. Nuzzo and Allara studied a method to self-assemble organic disulfides molecules on gold surfaces, which has stimulated the research of thiolate SAMs on metals [24]. The preparation of such SAMs was simple. Once a gold surface is immersed in thiol solution, a densely-packed molecular monolayer immediately forms within a few hours. After immersing a gold surface in a thiol solution, the SH groups form covalent Au–S bonds with the surface upon hydrogen release [22, 41, 42]. In the following step, intermolecular interactions induce a lateral ordering. The structure and kinetics of thiol SAM formation has been studied in great detail by many groups [25, 38, 43-48]. The high affinity of thiols for the metal surfaces makes it possible to form well-defined organic monolayer at the exposed interface [27, 28].

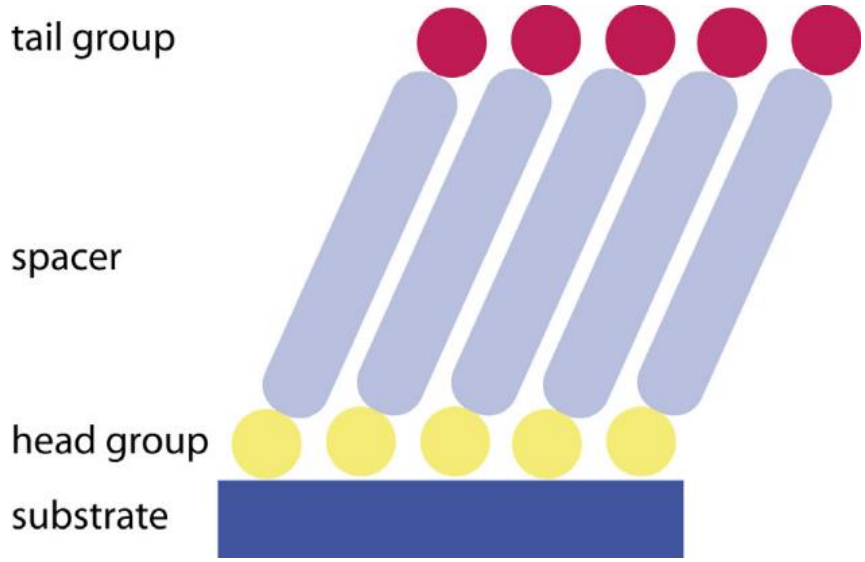

Fig.11 Schematic diagram of SAMs on a metal surface.

Nevertheless, the formation of the SAMs is not a single process. The investigation of SAM of N-alkanethiol by nonlinear vibrational spectroscopy indicates few steps for SAM formation. The formation of SAM consists of three steps: (1) fast initial adsorption, which results in the coverage of 80-90% during few minutes (throughout the process, head groups of molecules are chemisorbed into a metal surface indicating Au-S bond formation), (2) the process of straightening of hydrocarbons or spacers, (3) and the process of reorientation of terminal groups [38].

The intermolecular interactions are dependent on the nature of the spacer of the precursor molecule. It was found that the speed of self-organization of alkane thiols increases with increasing chain length [34].

The SAMs made from aromatic molecules have also been investigated. It has been shown that highly-oriented and densely-packed SAMs are formed from aromatic molecules with thiol head group on metal surfaces, like gold and silver [39].

The molecular orientation of aromatic molecules depends on the number of aromatic rings, the substrate, and the rigidity of the aromatic system. The tilting angle of the molecules in the SAMs with aromatic molecules is less tilted with increasing length of the aromatic chain. The same has been detected for the SAMs made of alkanethiol molecules, particularly the tilting angle is decreasing with increasing alkane chains. However, the difference in the tilt angles for aromatic SAMs on gold and silver is smaller than has been observed in the aliphatic films [39].

SAMs with alkane chains or phenyl rings are stabilized by van-der-Waals forces. The spacer group basically regulates the intermolecular packing and the degree of order in the film, while the terminal group defines surface properties. It also allows surface modification via chemical functionalization of terminal groups (NH_2, NO_2, CH_3,OH, COOH….). Properties of the surface can be altered by surface modification. Therefore SAMs can be used to control wetting, corrosion, lubrication, adhesion, etc. [40].

2.3 Aromatic SAMs

The SAMs with aromatic spacers were firstly introduced by Rubinstein and co-workers [45]. There has been increasing interest in aromatic SAMs in the last decade and many studies have been done. The formation of aromatic SAMs from various precursor

molecules on various metal substrates were studied by spectroscopic, microscopic, and diffraction techniques, which includes STM, XPS, NEXAFS, GIXD, IR spectroscopy, LEED, TDS, as well as, by quantum chemical calculations [41, 48-74]. It has been revealed that SAMs made of aromatic molecules have polymorphic structure, unlike SAMs with N-alkanethiol molecules [49, 50]. This flexibility to adjust the characteristics of aromatic SAMs, such as surface density and structure by varying molecular precursors, opens numerous possible functional applications of aromatic SAMs in surface materials science. One of the most appealing properties of the aromatic SAMs is the response to electron irradiation.

2.4 Electron-induced modification of SAMs

Since the 1990s, methods have been developed for patterning SAMs [22, 75]. The methods are based on two different schemes. The first method uses controlled deposition of molecules on the substrate in order to form SAM in predefined locations or using lithographical tools partially to modify SAMs. Dip-Pen-Nanolithography (DPN) is the most popular method for controlled deposition of molecules [76]. Patterned SAMs can be fabricated via the DPN method by depositing molecules with the tip of an atomic force microscope (AFM), achieving a lateral resolution of 10 nm. The second method of SAM patterning is nanolithography, which is done by ionizing radiation (photons, electrons or ions) [77-82]. The lithographic processes are widely available and well-established. Modifications of SAMs have been studied with the lithographical techniques [83-86].

The response of the SAM to electron irradiation depends on the structure and type of the precursor molecules. In particular, SAMs made of alkanethiols and aromatic molecules have completely different modifications due to electron irradiation:

a) In aliphatic SAMs, like alkane thiols, the electrons induce a cleavage of C–H bonds, which leads to an orientational and conformational disorder of the chains, desorption of material, and formation of C=C double bonds in the fragments that remain on the surface (Fig.12). Low electron irradiation of alkanethiols with high doses can lead to complete desorption of material from the surface [87].

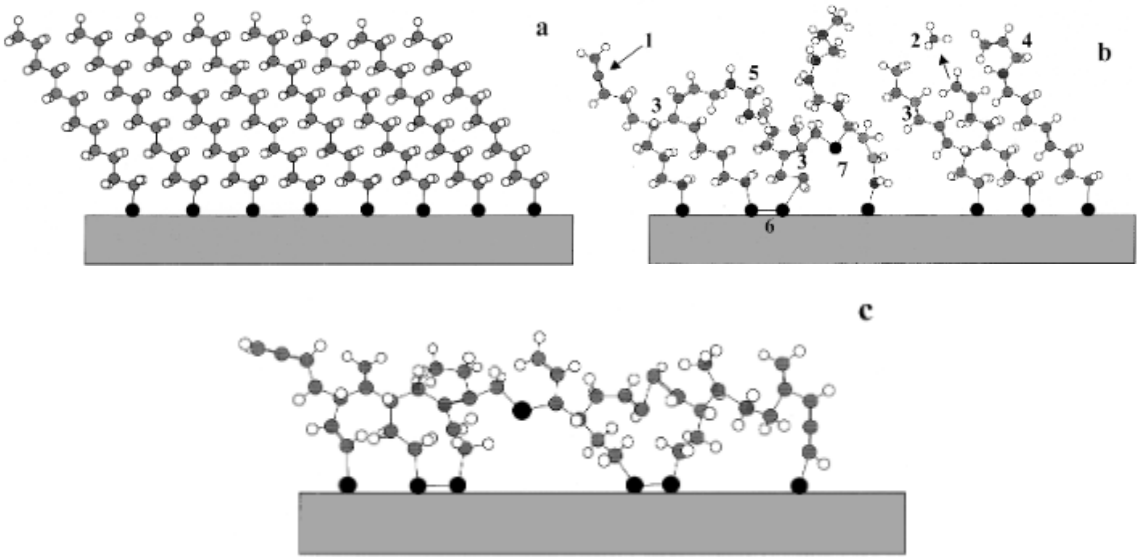

Fig.12 Schematic representation of electron irradiation of alkanethiol SAM: (a), (b), and (c) represent the pristine and slightly/strongly irradiated SAMs, respectively. Different irradiation-induced defects are marked in (b): 1 - cleavage of C-H bond; 2 - cleavage of C-C bond and desorption of the cut fragment; 3- the appearance of C-C/C=C crosslinks; 4 - a conformational defect; 5 - chain reorientation; 6 - formation of disulfide; 7 - incorporation of sulfur in alkyl matrix [87].

b) In contrast to the alkanethiols, when aromatic SAMs are exposed to electrons irradiation or to UV lights, they are laterally cross-linked via phenyl rings of neighboring molecules after cleavage of the C-H bonds on the aromatic rings (Fig.13a). During this process, cross-linked molecules maintain their preferred orientation and almost no material desorbs [60, 88].

In nitro-terminated aromatic SAMs, the C–H cleavage occurs as well, which additionally results in the reduction of nitro groups to amino groups (Fig.13b). Thus, SAMs can be further chemically modified so that functionalization of solid surfaces with molecular nanostructures of desired chemical composition and shape is possible. In summary, electron irradiation converts the terminal functionality of SAMs, while the aromatic rings are dehydrogenated and cross-linked. Additionally, surface regions that are cross-linked followed by conversion of amino-groups into nitro-groups can be used as a template for molecular immobilization. This process has been named chemical lithography, as the lithographic exposure directly affects the surface chemistry of the SAM [83, 88].

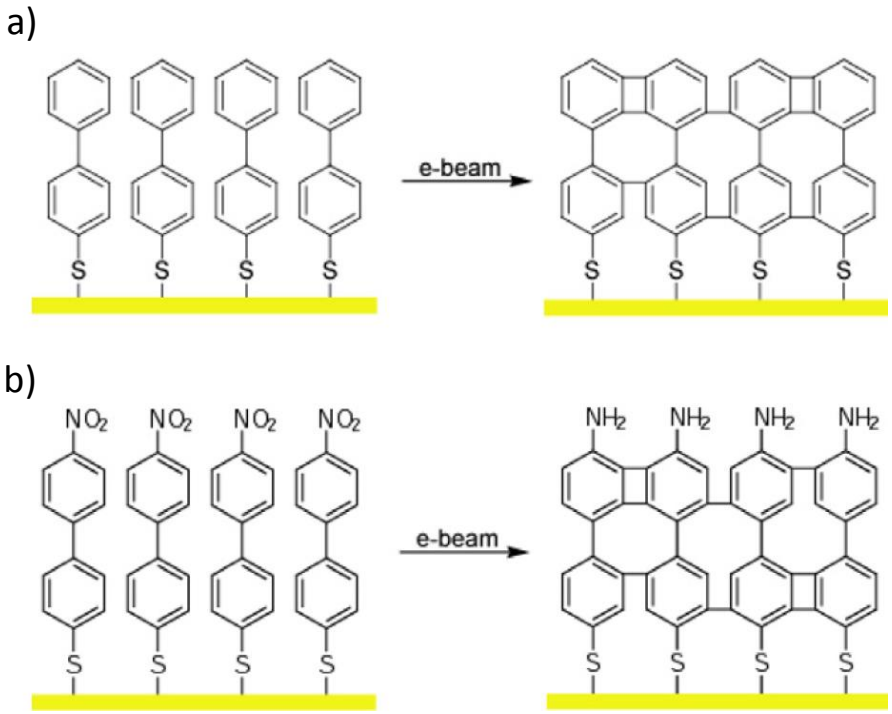

Fig.13 Electron beam induced modification of aromatic SAMs: (a) aromatic SAMs; (b) nitro-group terminated aromatic SAMs [40].

2.5 Cross-linking of aromatic SAM

A very detailed model of electron-induced crosslinking in aromatic SAMs based on the experimental and theoretical analysis has been presented by Turchanin on the example of electron-irradiated BPT-SAMs on gold [70]. The first step that leads to the formation of a cross-linked monolayer is the impact of an incident electron on a molecule, which leads to the cleavage of a C–H bond (Fig.14 a, c). It has been shown that ~650 primary electrons per molecule are necessary in order to create the cross-linked molecular network.

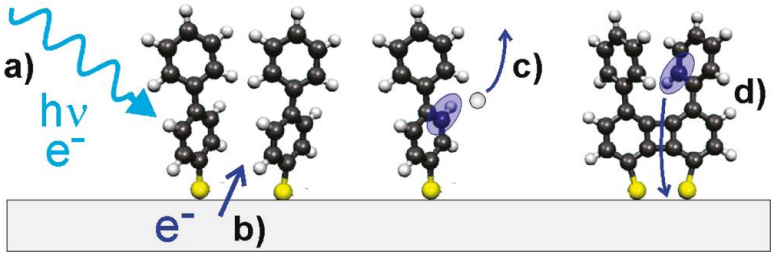

Fig.14 Schematic representation of the different steps involved in the cross-linking of aromatic SAMs: (a) irradiation, (b) emission of secondary electrons, (c) dissociation of C-H bonds, (d) self-quenching of electronically excited partially linked molecules [70].

Additionally, it has been shown that secondary electrons that are emitted from the substrate also cause a C-H bond breaking in BPT, which results in SAM cross-linking (Fig.14b). The partially dehydrated molecules relax by forming single- and double-links (C-C bonds) between adjacent phenyl rings by forming a 2D network. Moreover, changes during crosslinking take place at the sulfur/gold interface of a BPT-SAM. It was detected that besides the thiolate SAM species with an S2p3/2 binding energy of 162.0 eV, a new sulfur species with a binding energy of 163.5 eV form in a cross-linked SAM. It was interpreted by the presence of new organsulfide species [70].

The maximum degree of cross-linking is ~ 90%, which is achieved by a 50 mC/cm^2 radiation dose. A 100% cross-linking of all phenyl rings within the monolayer film is sterically hindered due to the molecular packing motifs in the pristine SAM.

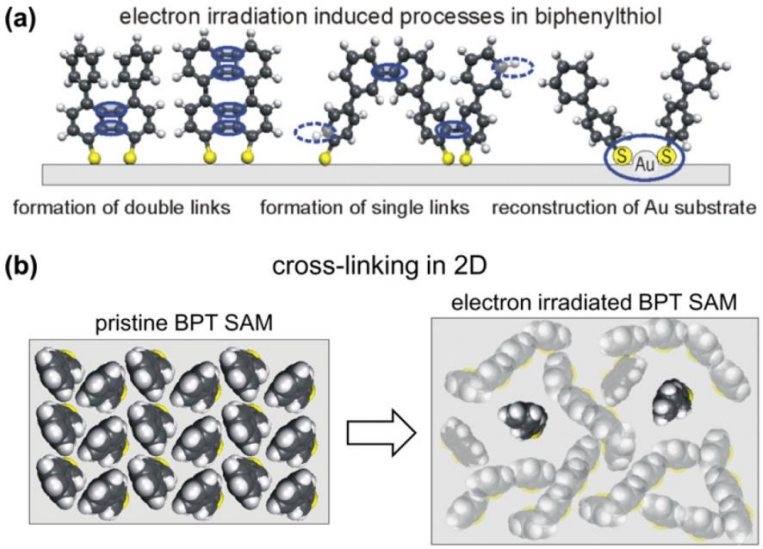

Fig.15 Schematic representation of the structural properties of pristine and cross-linked BPT-SAMs. (a) Molecular species formed upon e-beam irradiation. (b) Conversion of a pristine BPT-SAM into cross-linked BPT-SAM [70].

It was also demonstrated that some molecules within organothiol-SAMs form pairs, which are stabilized by an additional gold atom between neighboring sulfur atoms, as depicted schematically in Figure 15a, right. The phenyl rings can be stabilized by additional links at the upper phenyl rings, as shown in Fig.15a. To realize a crosslinking in two dimensions and the formation of CNM, it is important to consider the molecular packing motifs adopted in the pristine BPT-SAM (Fig.15b, left). Isolated BPT molecules reveal a characteristic twisting between the upper and lower phenyl rings. Within the

SAM, both phenyl rings may not be coplanar, but still have a substantial twisting. The intermolecular distances within the pristine film are given by Van der Waals dimensions of molecules, while the irradiation induced additional carbon links enable shorter distances. The density of the cross-linked films increases locally and may lead to the formation of "nano-voids," containing isolated, non-linked molecules with reduced coordination (denoted as dark molecules in the scheme in Fig.15b, right) [70].

In addition, it has been demonstrated that pristine SAMs have limited thermal stability, which completely desorbs from the surface at temperatures above 400 K. This mechanism is confirmed by the appearance of a metal sulfide species in the XPS data, which remains on the surface, while the carbon signal of the aromatic backbone completely disappears upon heating [70]. Unlike SAMs, a cross-linked BPT-SAM exhibits a thermal stability up to 1000 K [89]. SAMs become more stable with an increasing degree of cross-linking. This process saturates at a dose of 50 mC/cm^2 with 50 eV electrons.

2.6 Carbon Nanomembranes (CNMs)

As it is described above, SAMs are cross-linked if they are exposed to low energy electron irradiation or extreme UV light. A CNM is 2-dimensional monolayer that inherits properties from the SAM. Thickness, chemical composition, and density of the original SAM determine the properties and composition of the resulting CNM. The mechanical, optical, and electrical properties of CNMs are, thus, to a large extent determined by the initial molecular monolayer. A CNM can be fabricated from a variety of aromatic molecules [90]. The thickness of a CNM is approximately equal to the length of the precursor molecule, which it is made of. The mechanical stiffness of a CNM can be enhanced when it is exposed to the low energy electron irradiation with doses from 30 mC/cm^2 up to 50 mC/cm^2. Further increase of an electron irradiation dose, particularly higher than 50 mC/cm^2, does not enhance the mechanical stiffness and elasticity of a CNM. Taking into consideration the mechanical properties of CNMs, a free-standing CNM can be obtained by releasing it from the initial substrate and transferring it onto transmission electron microscopy (TEM) grids or porous support [91].

A freely suspended CNM is about as thick as the original SAM and can span large areas of more than 500 x 500 μm^2.

CNMs can be released from the initial substrate and transferred onto an arbitrary substrate by dissolving the underlying substrate [91]. The procedure of transferring of a CNM onto an arbitrary substrate is presented in Figure 16. The basic idea is quite simple. When a SAM is cross-linked and a CNM is prepared, the underlying substrate is dissolved. Before dissolution of the underlying substrate, a much thicker polymeric layer is spin-coated onto a CNM in order to preserve its shape and to not induce ruptures and folding during the entire process (thickness of polymeric support layer is about 500 nm). Afterwards, a CNM with a supportive polymeric layer is placed onto another substrate. Finally, by dissolving the supportive polymeric layer, the transfer of a CNM onto another substrate is accomplished.

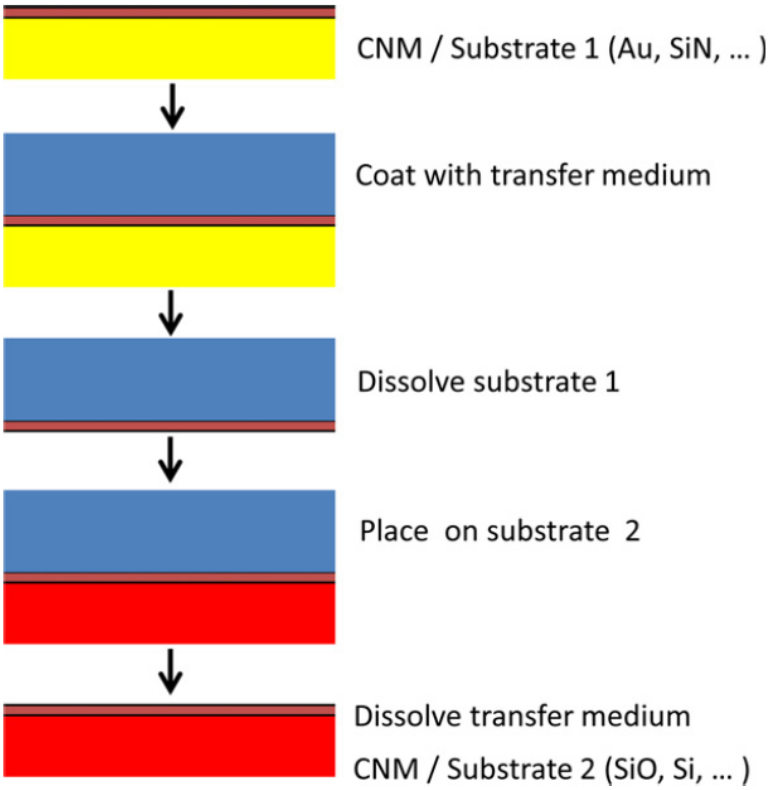

Fig.16 Schematic representation of the transfer procedure of CNMs onto arbitrary surfaces [91].

Moreover, it has been shown that multilayer CNMs can be prepared by stacking, via repeating the transfer procedure of individual CNMs [94]. Additionally, it has been discovered that a CNM can be converted into graphene sheets upon heating it above

1000K [91, 93]. It has been detected that sulfur atoms, which are initially presented in the monolayer, continuously desorb upon heating until they completely vanish at temperatures above 800K. It has been shown that the remaining film is not anchored by thiolate, but is solely stabilized by lateral links within the aromatic network, which is

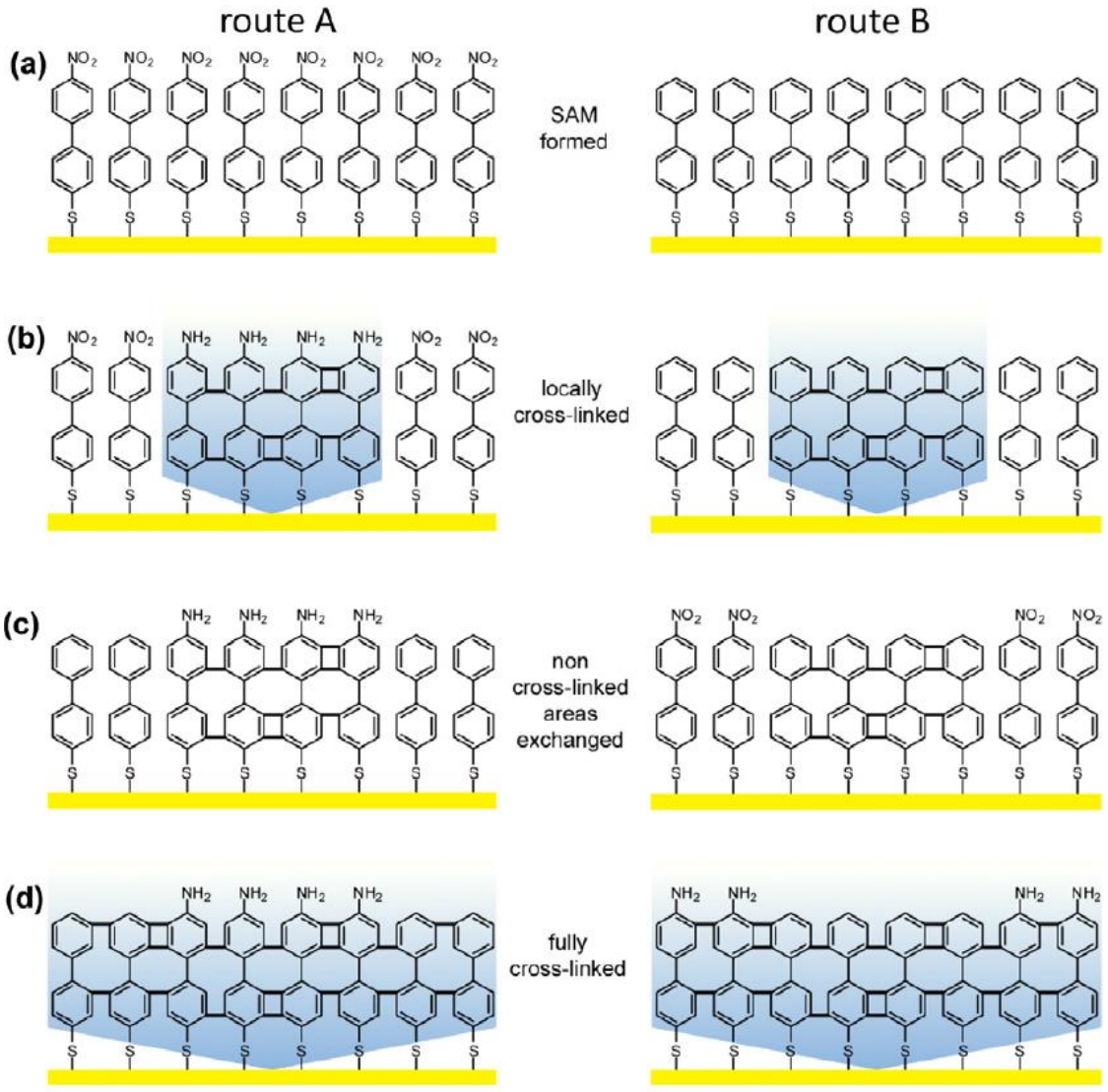

Fig.17 Schemes for the fabrication of CNMs with alternating chemical patterns. (a) A self-assembled monolayer of NBPT for route A and BPT for route B is formed on a gold surface. (b) The SAM is locally irradiated by electrons resulting in a pattern of cross-linked and non-cross-linked biphenyls. (c) In the non-cross-linked parts of the SAM, the thiols are exchanged for other biphenyl-thiols. (d) The complete monolayer is exposed to electrons. This final step results in a fully cross-linked monolayer and converts all nitro groups to amino groups [40].

directly coupled to the gold surface underneath via Van der Waals interactions. This conclusion is well corroborated by the temperature dependent NEXAFS measurements revealing a downward tilting of the aromatic rings [70].

Furthermore, it has been shown [95] that geometrical patterns can be made in a CNM with different chemical functionalities. Fabrication of such patterns is based on the ability of thiol-based SAMs to exchange molecules [22]. The exchange occurs by immersing a SAM of thiol X in a solution of thiol Y for a certain time. But cross-linked SAMs do not exchange molecules in a solution of other thiols [96], as their molecules are laterally strongly bonded, providing high stability. Consequently, molecular patterns are fabricated by an exchange of the non-cross-linked regions of locally cross-linked SAMs and, afterwards, by complete cross-linking of exchanged ones. Hence, a CNM with different chemical functionalities is obtained (Fig.17).

In this chapter, a self-assembled monolayer was presented with regard to its properties. It was shown that a SAM can be converted into an ultrathin free-standing CNM with well-defined thickness and surface functionality when it is exposed to low energy electron irradiation or extreme UV light. Additionally, it was shown that a CNM is a nanosheet with tailored physical, chemical, and biological functions. There can be designed patterns of a CNM in which distinct locations are occupied by different chemical functionalities. The mechanical properties of a CNM allow it to obtain free-standing CNMs with areas of more than 500 x 500 μm^2.The thickness of a CNM is determined by the size and the molecular packing of the SAM. In comparison with synthetic membranes that are commonly used nowadays in filtration, in sensors, or as barriers, CNMs are orders of magnitude thinner. The thinness is their most important property. Taking into consideration the abovementioned properties of SAMs and CNMs and, in particular, the possibility of variation of precursor-molecules and appearances of nanopores in CNMs [90], a CNM is an attractive object to examine for gas permeation and membrane gas separation.

Chapter 3

Analytical techniques for characterization of CNMs

To characterize and control the formation of SAMs and CNMs, analytical techniques, such as XPS (X-ray photoelectron spectroscopy) and HIM (Helium ion microscopy), were employed in this study.

3.1.1 X-ray photoelectron spectroscopy (XPS)

X-ray photoelectron spectroscopy is a technique used for analyzing surfaces of materials. It can provide quantitative and chemical information about the surface of the material being studied. XPS can measure the elemental composition, empirical formula, chemical state, and electronic state of the elements within a material. The mechanism of XPS is based on the photoelectric effect that was first discovered by Hertz in 1887, which describes the ejection of electrons from the atom via bombardment of the surface by photons. However, the technique itself was developed in the 1950s by the Siegbahn team, who was awarded the Nobel Prize for physics in 1981.

XPS spectrum is obtained by irradiating a solid surface with a beam of X-rays while simultaneously measuring the kinetic energy and electrons that are emitted from the top 0 to 10 nm of the material being analyzed. A sample is irradiated under ultra-high vacuum with X-rays that are able to penetrate the sample for several micrometers. If the energy is high enough, an electron is released from the core orbital of an atom by incident X-ray.

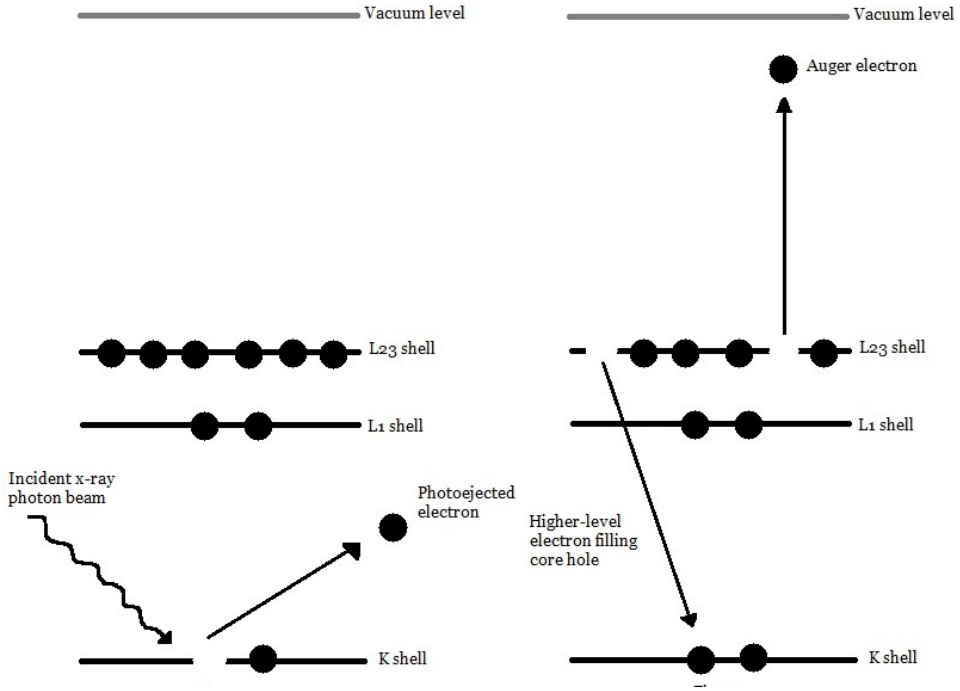

Fig.18 X-ray photoemission and Auger electron emission.

As a second process, an electron from an outer shell can relax to an inner shell by releasing a second electron (Auger electron). Both mechanisms are schematically depicted in Figure 18.

The kinetic energy of an electron is dependent on an incident X-ray and the binding energy of the atomic orbital from which it originated. As the energy of an X-ray with a particular wavelength is known (for Al K_α X-rays, E_{photon}= 1486.7 eV), and the emitted electron's kinetic energies are measured, the electron binding energy of each of the emitted electrons can be determined by using an equation that is based on the work of Ernest Rutherford (1914):

$$E_{binding}=E_{photon}-(E_{kinetic}+\psi) \quad (8)$$

where $E_{binding}$ is the binding energy (BE) of the electron, E_{photon} is the energy of the X-ray photons being used, $E_{kinetic}$ is the kinetic energy of the electron as measured by the instrument and ψ is the work function dependent on both the spectrometer and the material. As can be seen in Figure 19, the ejected photoelectrons are collected and analyzed as a function of their kinetic energy using a photoelectron spectrometer.

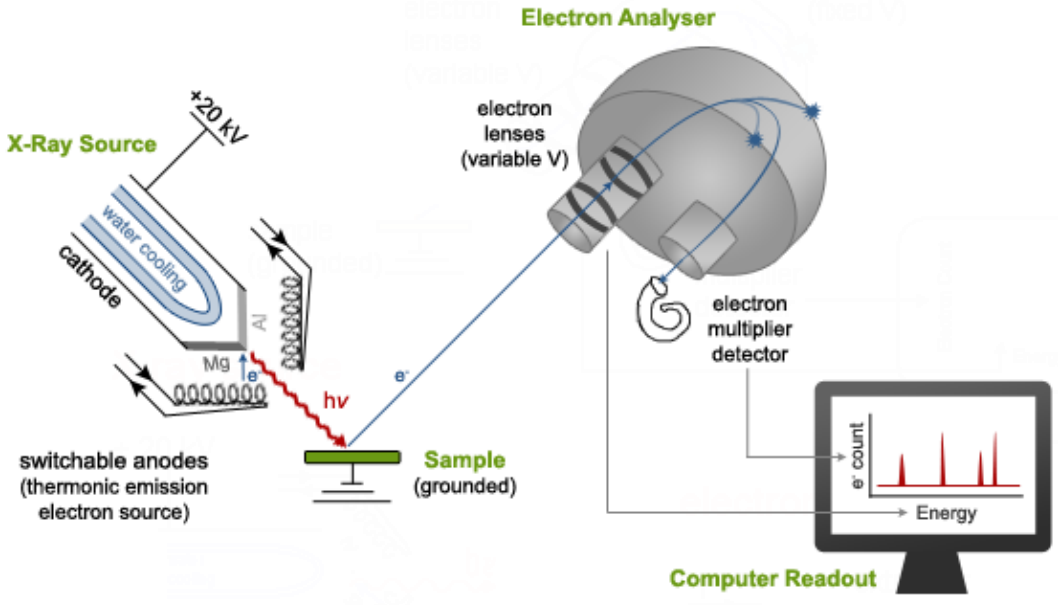

Fig.19 Schematic representation of an X-ray photoelectron spectrometer.

The technique consists of a series of electrostatic lenses and steering voltages to selectively separate electrons and bring them to an electron multiplier where they are

detected (Fig.19). All this takes place under ultra-high vacuum (UHV) conditions of $<10^{-9}$ mbar pressure. Any non-volatile solid sample can be analyzed, although non-conducting materials may require some special techniques to properly analyze, like bombarding the surface of the sample with an electron gun.

XPS detects the electrons that are ejected from the surface of the sample. The emitted photoelectrons ($d < 5\lambda$, d is a thickness of overlayer thin film and λ is a mean free path of the electrons of the thin film layer) won't be captured or trapped into the material in opposite to the ones which are emitted from deep inside of the material due to the limitation of the mean free path of low energy electrons. Figure 20 shows the mean free path of electrons in solids as a function of electron energy [97]. At the minimum of this characteristic fundamental curve, between 40 and 100 eV the maximum surface sensitivity is achieved.

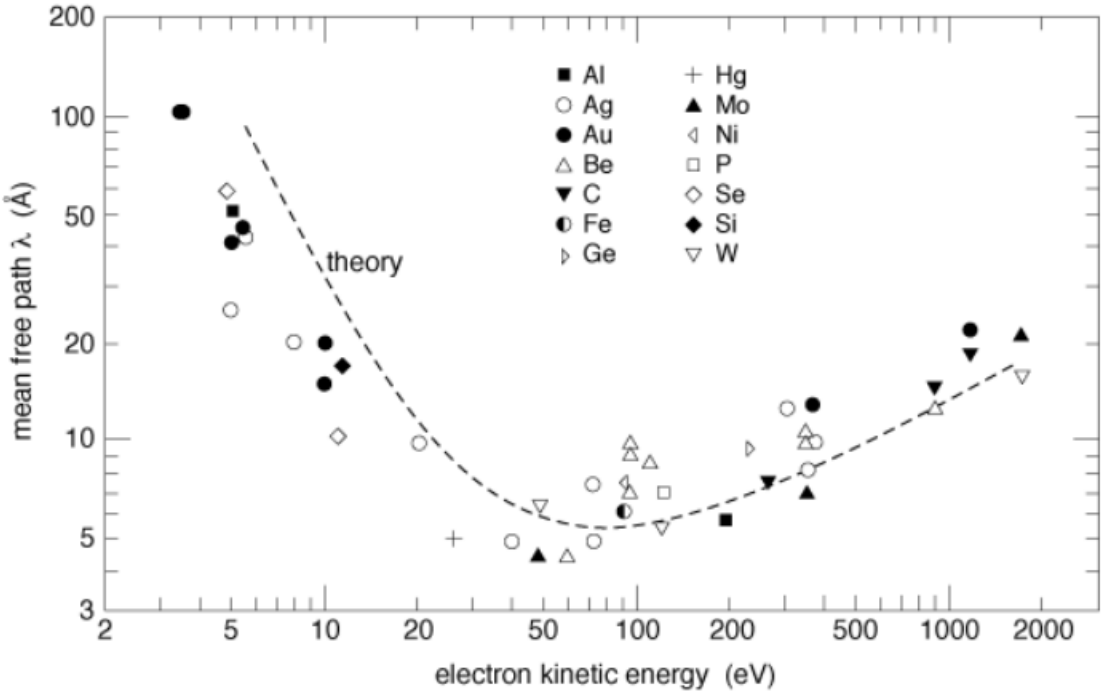

Fig.20 Mean free path of electrons in solids. The dashed curve is the theoretical calculation and the dots are experimental measurements [97].

A typical XP spectrum is a plot of the number of photoelectron intensity as a function of the binding energy. The electron signal includes contributions from both photoelectron and Auger electron lines. The energies and intensities of the photoelectron peaks enable identification and quantification of all surface elements (except hydrogen).

Each element of the material produces a characteristic set of XPS peaks at specific binding energies that distinguish each element, which is on or in the surface of the material being analyzed (Fig.21). These peaks match to the electron configuration of the electrons within the atoms that are 1s, 2s, 2p, 3s, etc. The quantity of detected electrons for the specific peak is directly related to the amount of element that is on the surface of the sample being analyzed.

As the binding energy is independent of the X-ray energy, it becomes easier to compare signals. In addition, the binding energy is dependent on the chemical environment of the element. When the same atom is bonded to a different chemical species, this leads to a change in the binding energy of its core electrons. The variation of binding energy results in a shift of the corresponding XPS peak. This effect is termed as chemical shift, which can be applied to study the chemical status of all elements in the surface (Fig.21). Therefore, XPS is also known as electron spectroscopy for chemical analysis (ESCA).

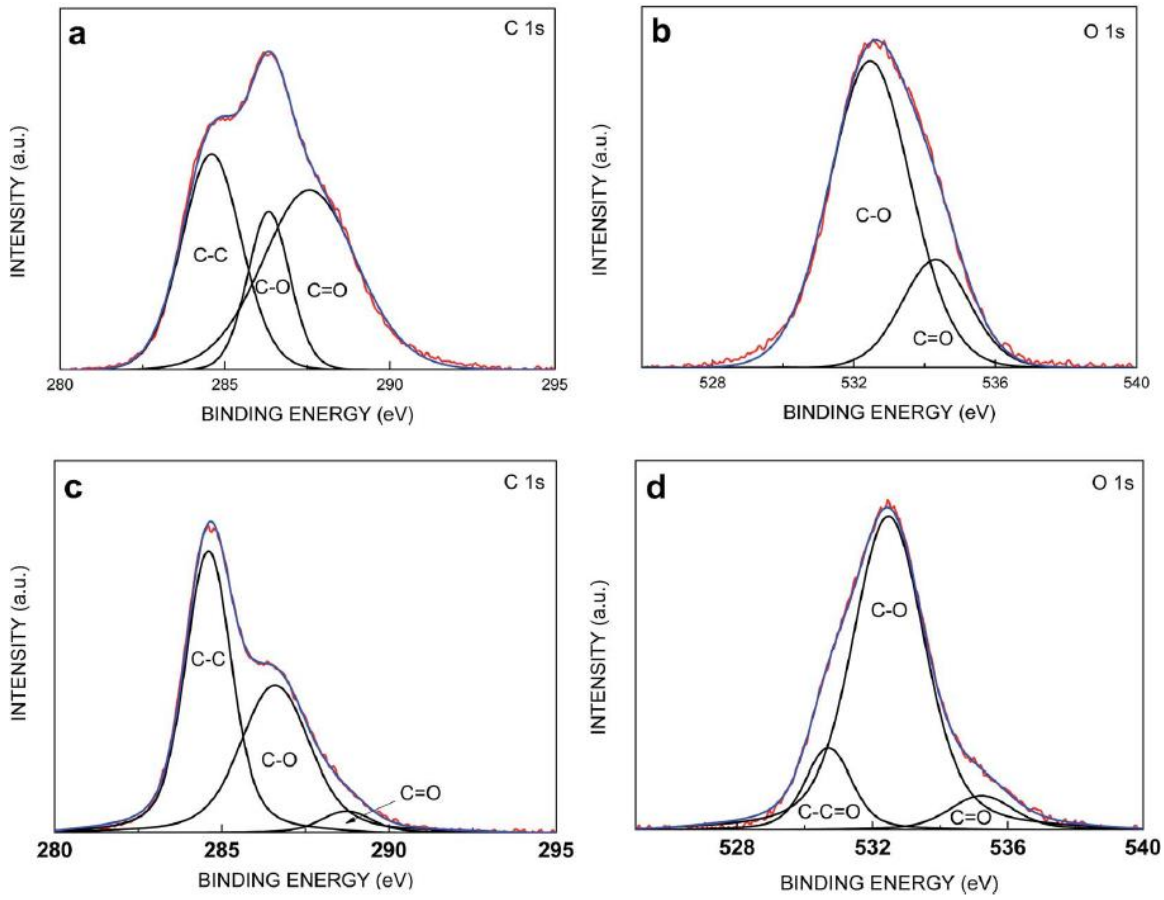

Fig.21 (a) C1s XPS spectra of MGrO (Mildly-oxidized Graphite Oxide); (b) O1s XPS spectra of MGrO; (c) O1s XPS spectra of MGrO–SS (SS-surfactant) and (d) O1s XPS spectra of MGrO–SS [98].

3.1.2 Thickness of thin layer

To determine the thickness of thin film on the substrate, the attenuation of the substrate signal by the adsorbate overlayer can be used. If the attenuation length of electrons could be determined by experiments, the thickness of an overlayer thin film can be determined by comparison of the XPS signal between the clean substrate and that of the specimen according to the equation:

$$I_d = I_0 * e^{-\frac{d}{\lambda * \cos\theta}} \quad (9)$$

where d is the thickness of the overlayer, λ is the attenuation length of electrons from the substrate in the overlayer, θ is the take off angle of the electrons with respect to the surface normal, I_0 and I_d are XPS signals, respectively, from the clean and adsorbate-covered substrate. In accordance with Equation 9, we calculate the thickness d as follows:

$$d = -\lambda * \cos\theta * \ln\left(\frac{I_0}{I_d}\right) \quad (10)$$

3.2 Helium Ion Microscopy (HIM)

Helium Ion Microscope (HIM) is an imaging technique that uses beam of helium ions which is focused and scanned across the sample and produce images with 0.25 nm resolution. It has similarities with the scanning electron microscopy (SEM). In HIM, a focused beam of helium ions with a diameter of less than 0.35 nm is scanned over the sample (Fig.22). The scanned He+ ions generate secondary electrons (SE), and while recording emitted SEs, generate the HIM images. In SE imaging, the topology of the sample produces contrast as more electrons are ejected when the He+ beam hits the sample at glancing incidence. In the case of insulating samples, the imaging may lead to positive charging due to the emission of secondary electrons as well as the exposure to positive He+ ions. A major advantage of HIM is its ability to compensate for sample charging by employing an electron flood gun in an alternating manner. In this way, the sample is exposed to electrons between scans of subsequent image lines or frames.

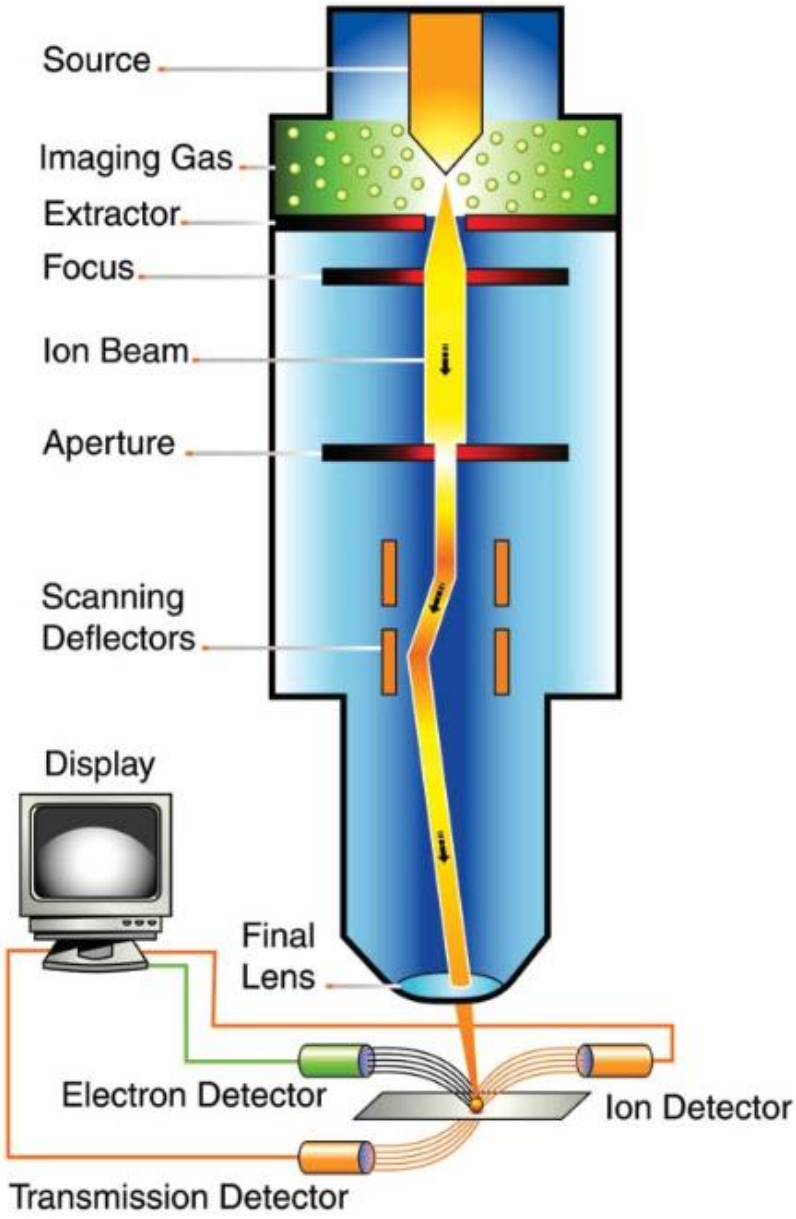

Fig.22 Schematic of the Orion HIM imaging system [99].

Compared to SEM, the energy of the SEs is lower, resulting in higher surface sensitivity. Edge resolutions of 0.24 nm (asbestos fiber) and 0.29 nm (HOPG) are reported [114, 115]. To get high resolution images from scanning beam microscope, one must be able to produce a sufficiently small probe, have a small interaction volume in the substrate, and have plenty of information-rich particles to collect to create the image. A typical SEM is able to meet all of these requirements to some extent. The helium ion microscope based on a Gas Field Ion Source (GFIS) has significant advantages over the SEM in all three categories. A helium ion source offers high brightness and a small energy spread,

therefore, allows the beam to be focused to small probe sizes relative to the SEM. Regarding the interaction in the substrate, the shape and size of interaction volume play, despite the initial beam diameter, an important role in the final resolution and contrast. Helium is much heavier than an electron, thus giving it a momentum that is sufficiently higher. Monte-Carlo simulation shows that near the surface, where secondary electrons can escape, the helium beam produces a very narrow excited volume. Hence the helium image contains surface information about the probed area (Fig.23) [100].

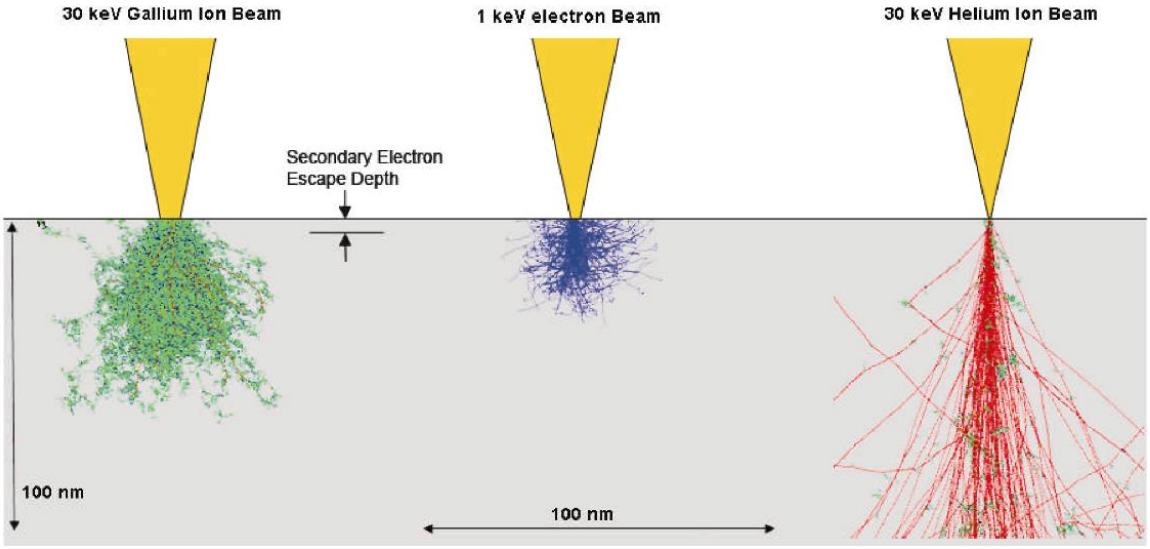

Fig.23 Monte-Carlo simulation results for gallium, helium, and electron beams into silicon [100].

Figure 24 compares simulations of typically used charged particles, Ga-ions, He-ions, and electrons penetrating a solid [101]. Generally, the full interaction volume of helium is bigger than that of electrons, as the ions travel very deep in the material. Gallium beams, on the other hand, interact strongly with a sample. As a consequence, the interaction volume broadens immediately below the point of impact but stays close to the surface. All these interactions produce a number of measurable signals. For imaging, the interaction volume for generating secondary electrons (SE) is most important. From Figure 24, it is visible that the He+ beam stays pretty collimated in the relevant depth of less than 10 nm.

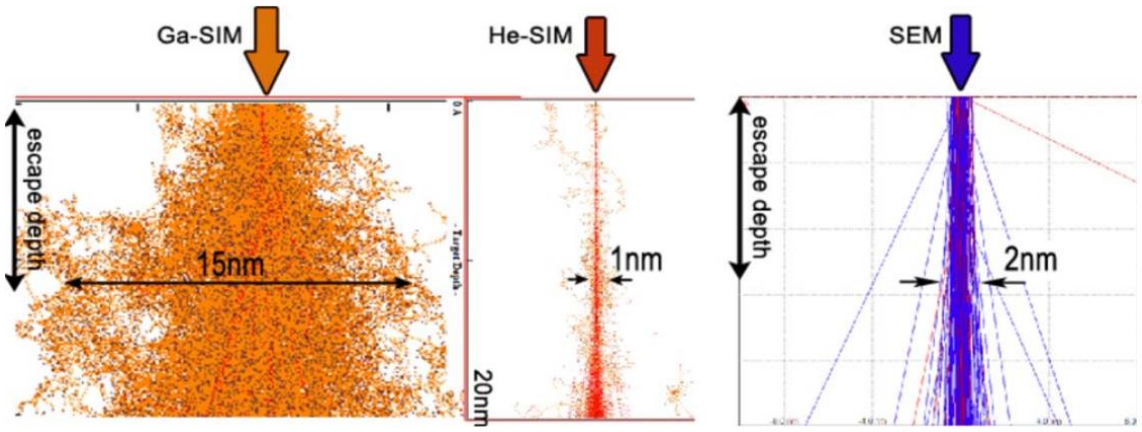

Fig.24 Comparison of simulation of beam-sample interaction of gallium, helium, and electron trajectories hitting a silicon surface with a zoom on the first 20 nm of the sample. The escape depth is taken to be approximately 10 nm, and for each beam the radius of interaction is measured as the maximum width attained above the escape depth [101].

It has been shown that HIM is a good candidate for imaging freestanding CNMs due to its efficient charge compensation tool. Scanning with a beam of helium ions, while recording the emitted secondary electrons, generates the HIM images. The advantages of HIM are high resolution, high surface sensitivity, and large depth of field [102].

Chapter 4

Method of gas permeation measurements

4.1 The working principles of gas permeation setup

Single gas permeation measurements of single- and multi-layer CNMs on different supports were carried out with a constant volume/variable pressure experimental setup [103] (schematically represented in Fig.25). The permeation of a number of gases, such as helium, hydrogen, carbon dioxide, argon, oxygen, nitrogen, methane, and ethane (He, H_2, CO_2, Ar, O_2, N_2, CH_4, C_2H_6) have been observed and their corresponding permeances and ideal gas selectivities were obtained. The permeances for the samples were measured at constant feed pressures of 108 to 500 mbar at room temperature (T=30°C). The feed pressures were chosen to be sufficiently low to employ the ideal gas model in the data evaluation, as well as, sufficiently high to match the sensitivity of the measurement system. Each gas measurement was repeated several times and the result was considered acceptable when the permeance values scattered below 5%. The evacuation time for the membrane degassing was approximately 2 minutes, since the CNM thickness is negligible, and sorption of the gas can only occur on the membrane surface. The supportive layers are relatively thin and can desorb all dissolved gas molecules within the aforementioned time. The membrane permeance was calculated according to the following equation [103]:

$$P_{perm} = V_{m,STP} \frac{V_p}{A_M R T (t_1 - t_0)} ln\left(\frac{P_f - P_p(t_1)}{P_f - P_p(t_0)}\right) \quad (11)$$

where $V_{m,STP}$= 0.022414 m^3(STP)/mol is the molar volume of an ideal gas at standard temperature and pressure (STP); V_p is the permeate volume; A_M the membrane area; R is the gas constant; T is the temperature; $\Delta t=(t_1 - t_0)$ is the time difference between two points (0 and 1) on the pressure increase curve at permeate side (Fig.26); P_f the feed pressure considered constant in the time range Δt, and $P_p(t_0)$ and $P_p(t_1)$ are permeate pressures at time moments 0 and 1, respectively. The ideal gas selectivity was calculated as a ratio of two gas permeances:

$$\alpha(ij) = {P_i}/{P_j} \quad (12)$$

4.2 Gas permeation setup

A schematic diagram of the experimental setup is depicted in Figure 25. The main components of the setup are a cylindrical measurement cell, a turbomolecular vacuum pump, a calibrated volume on the permeate side, a feed side gas bottle, and pressure sensors. All components, except the turbomolecular vacuum pump, are placed within the thermostat zone. They are connected by a number of pipes and pneumatically driven vacuum valves that reduce the risk of gas leakages and ensure instant process control. Feed and permeate pressure sensors on both sides of the membrane cell detect the gas permeation. Measurement accuracy is set by choosing pressure sensors with an upper limit of 200 mbar for feed side and 130 mbar for permeate side. Data is recorded with a sampling rate of 0.5 seconds using a software (National instrument Lab View 2011) combined with a computer.

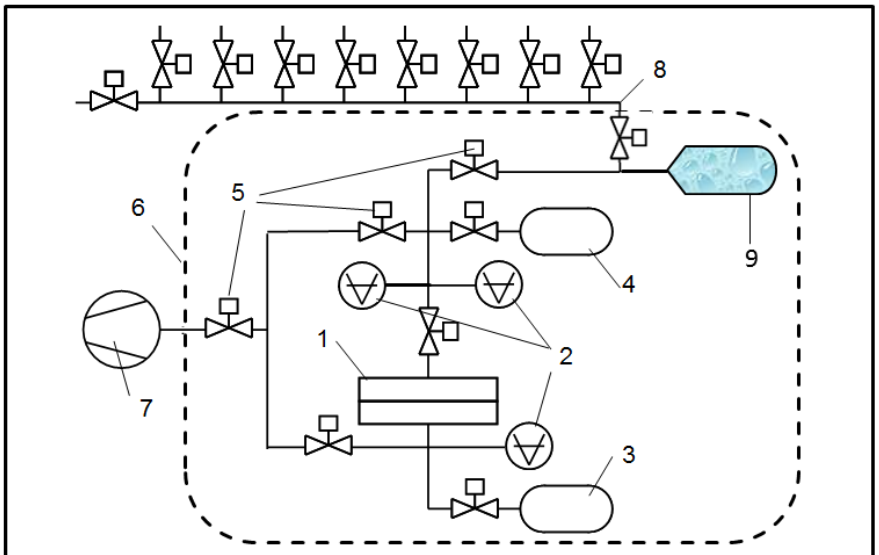

Schematic drawing of the experimental setup:
1 – measurement cell; 2 – feed and permeate pressure sensors;
3 – calibrated volume on the permeate side; 4 – feed side gas bottle;
5 – pneumatically driven vacuum valves; 6 – thermostated zone;
7 – turbomolecular pumping station; 8 – gas supply line with 8 gas inlets
9 – Water vessel

Fig.25 Schematic representation of the experimental setup employed for gas permeation measurement for different types of CNMs [103].

The essential component of the set-up is the cylindrical measurement test cell (Fig.25). To ensure sufficient mechanical stability, the membrane sample is placed on top of a sintered metal filter. The O-ring (EPDM-Ethylene propylene diene monomer), which is below the modified membrane test cell upper part, seals the membrane. The active working area of membrane is ~ 0.89cm^2, which must be taken into account while analyzing the results. The principles of the measurement are the following: a) feed and permeate sides of the setup are evacuated, b) then permeate side (calibrated volume) is sealed, c) afterwards, single gas is introduced at constant feed pressure, and d) eventually, the increase of permeate pressure is detected (Fig.26). Pressure increases in the permeate side of the setup, overtime. By applying a vacuum on the permeate side before the start of a measurement, a time dependent pressure increase can be observed (Fig.26).

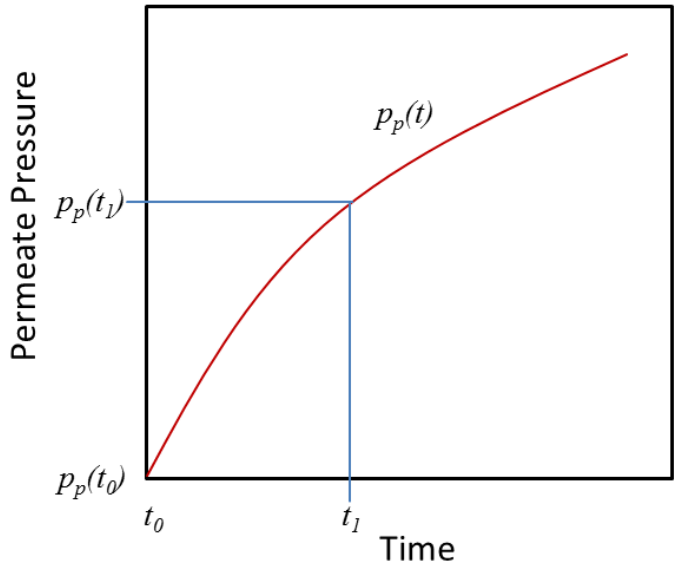

Fig.26 Schematic representation of permeate pressure as a function of time [103].

The permeance of a CNM will then be calculated with the help of Equation 11. It is the flux per unit pressure difference between the two sides of the membrane. It relates to the permeability, which is the intrinsic material parameter that changes consistently with the thickness of a membrane, as follows:

$$P_{permeance} = \frac{P_{permeability}}{l} \quad (13)$$

where l is the membrane thickness. Permeance is usually employed to characterize asymmetric or composite membranes, while permeability is typically used for dense film.

4.3 Thin-film composite membranes as a support for gas permeation of CNMs

The gas permeation of a CNM can be investigated by transferring a CNM onto a support and then conducting the measurements. The ideal way to obtain gas permeation properties of a CNM is to measure a free-standing CNM. In particular, taking into consideration that free-standing CNMs can span macroscopic areas up to 0.5×0.5 mm^2, the intrinsic gas permeation properties of CNMs could be measured by transferring a CNM onto the support with openings [102]. The results will reflect the real picture of gas permeation of a CNM. However, the drawback of gas permeation measurements of free-standing CNMs is appearance of defects that make it impossible to extract intrinsic gas permeation properties of CNMs. Nevertheless, to examine gas permeation of CNMs, dense or porous supports might be employed.

Example of dense polymeric support that has been employed for CNM gas permeation is polydimethylsiloxane (PDMS) thin film composite (TFC) membrane [104]. In the work of Min Ai et al., a PDMS-TFC membrane was employed as a support for gas permeation measurements of single- and triple-layer NBPT-CNMs and BPT-CNMs [18]. PDMS is a very common material applied in microfluidic devices and gas separation, due to its advantages, which include its elastomeric properties, biocompatibility, high gas permeability, optical transparency, and relatively high chemical inertness [105]. However, the most important role of a PDMS is "to seal" CNM defects, which are common in free-standing ones. It decreases the impact of defects on the measured permeance values, in comparison to the defects in the case of free-standing ones, due to the low permeance of PDMS. PDMS-TFC membranes were fabricated at Helmholtz-Zentrum Geesthacht and consist of a smooth flat PDMS film on a porous polyacrylonitrile (PAN), supported by non-woven polyester. The thickness of the PDMS thin layer in a PDMS-TFC membrane varies in the range of several hundred nanometers. A PDMS layer also supports a ~ 1 nm thick CNM and allows homogeneous drainage of the gas permeated through a CNM to the pores of a PAN microporous membrane. PAN is a material with an extremely low gas permeability coefficient, and all transport of gas

molecules occurs only through the membrane porosity, having average pore sizes in the range of 20 nm and surface porosity of 15%.

4.4 The alternative for the dense, non-porous PDMS-TFC support for CNMs

In the work of Min Ai et al. [18], a PDMS-TFC membrane was the only support employed to explore CNMs for gas permeation. In this work, a variety of polymeric membranes were tested as a support for CNMs in order to have a more realistic picture for intrinsic gas permeation properties of CNMs. The following dense polymeric membranes were examined as alternative dense supports for CNMs: PTMSP-TFC and Teflon AF 2400 TFC membranes. Unfortunately, both dense membranes showed dissatisfying results.

The problem with PTMSP-TFC membranes used as support for CNMs was caused by ageing. The PTMSP-TFC membrane showed a significant drop of gas permeance over a period of time. The drop based on the permeance of argon gas is presented in Figure 27.

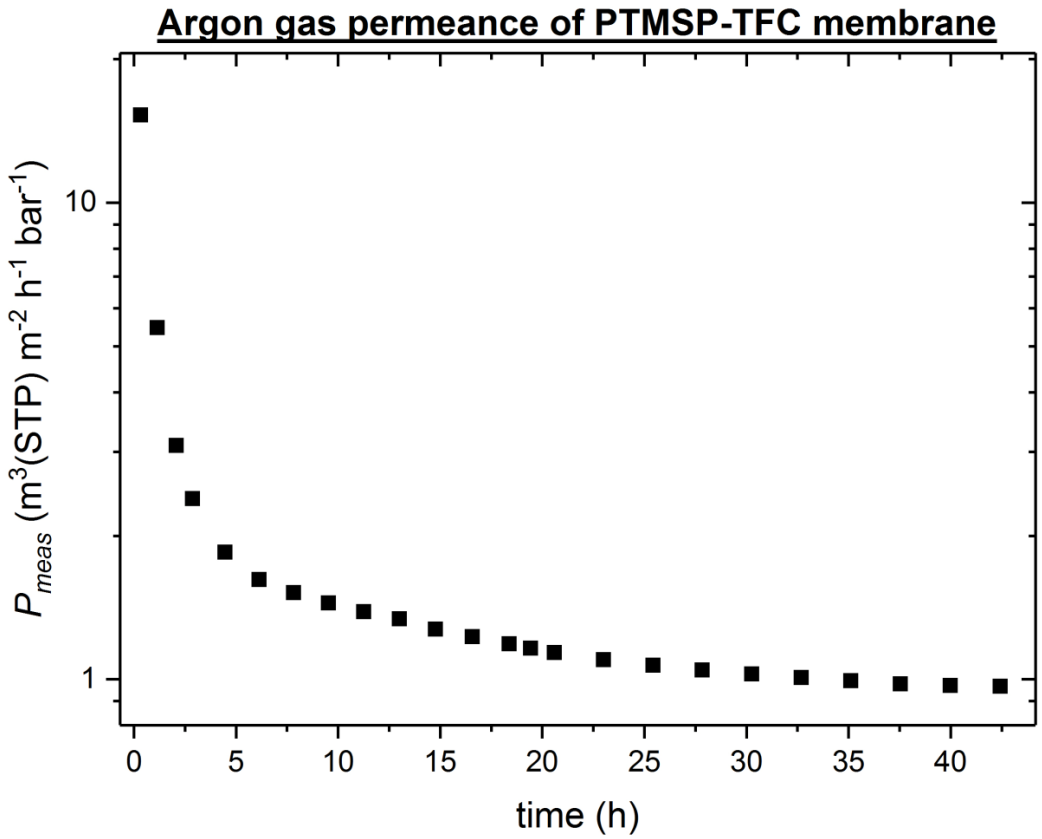

Fig.27 Measured value of gas permeance of argon gas through PTMSP-TFC membrane, over time.

As shown in Figure 27, the gas permeance of argon decreases significantly over time. The same result was observed with nitrogen gas permeance. Therefore, a PTMSP-TFC membrane was not employed as an alternative support for PDMS-TFC for investigation of gas permeation of CNMs. The drawback with Teflon support was weak adhesion to CNMs. It was often observed that CNMs detach from the Teflon surface after transfer onto it. However, successfully transferred CNMs onto Teflon supports were examined for gas permeation, and results confirmed weak adhesion between the supports and the CNMs (Fig.28). As shown in Figure 28, the measured gas permeances of the reference Teflon membrane, single-layer NBPT-CNM on Teflon and three-layer NBPT-CNMs on Teflon are in the same range, and the permeance curves have similar shape as for reference Teflon membrane. This reaffirms the assumption of weak adhesion between a CNM and Teflon.

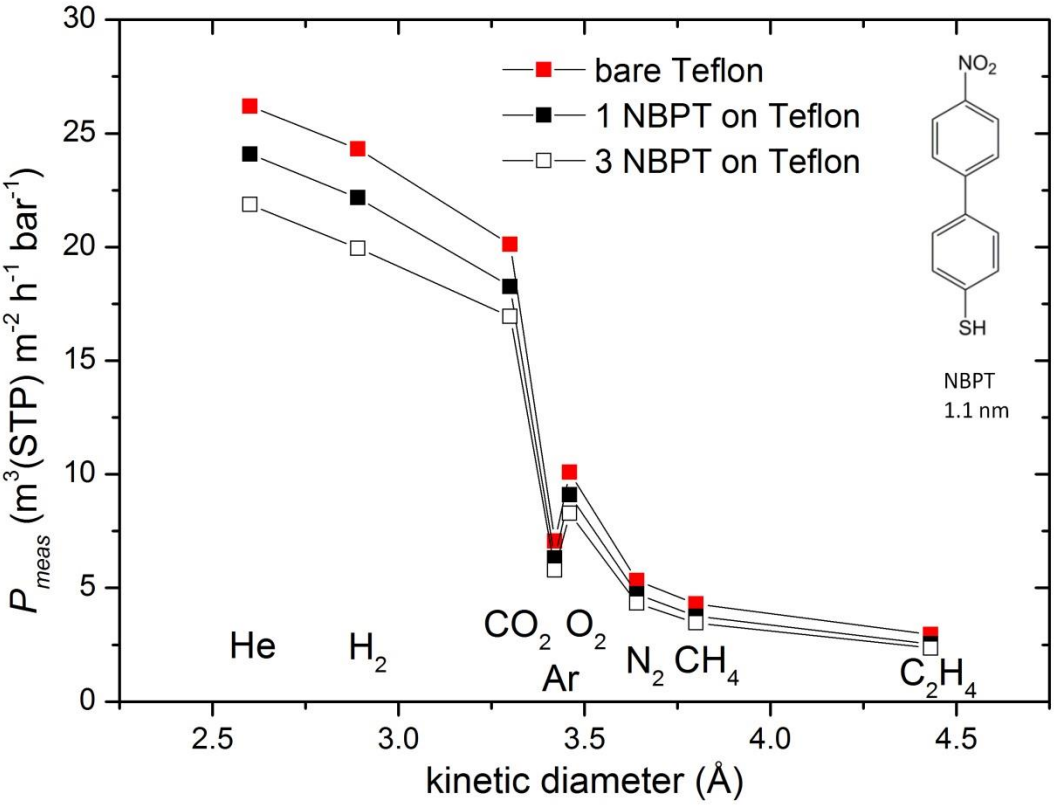

Fig.28 Measured values of gas permeance of single- and three-layer NBPT-CNMs on Teflon support.

4.5 Porous PAN support for CNMs

The idea of implementation of porous support for CNM gas permeation seems very appealing, especially when comparing the results of gas permeance of CNMs based on two different types of supports—non-porous dense PDMS-TFC and porous PAN. As is shown in Chapter 2, CNMs can be transferred onto arbitrary substrates, and, particularly, in the case of TEM grids, a freestanding CNM is obtained [91]. Although it has been shown that CNMs have ultimate tensile strength and exhibit high resistance against creep deformation, the results revealed defects with freestanding CNM, particularly when transferred onto TEM grids [92]. Difficulties in making defect-free CNMs over large areas have also been observed.

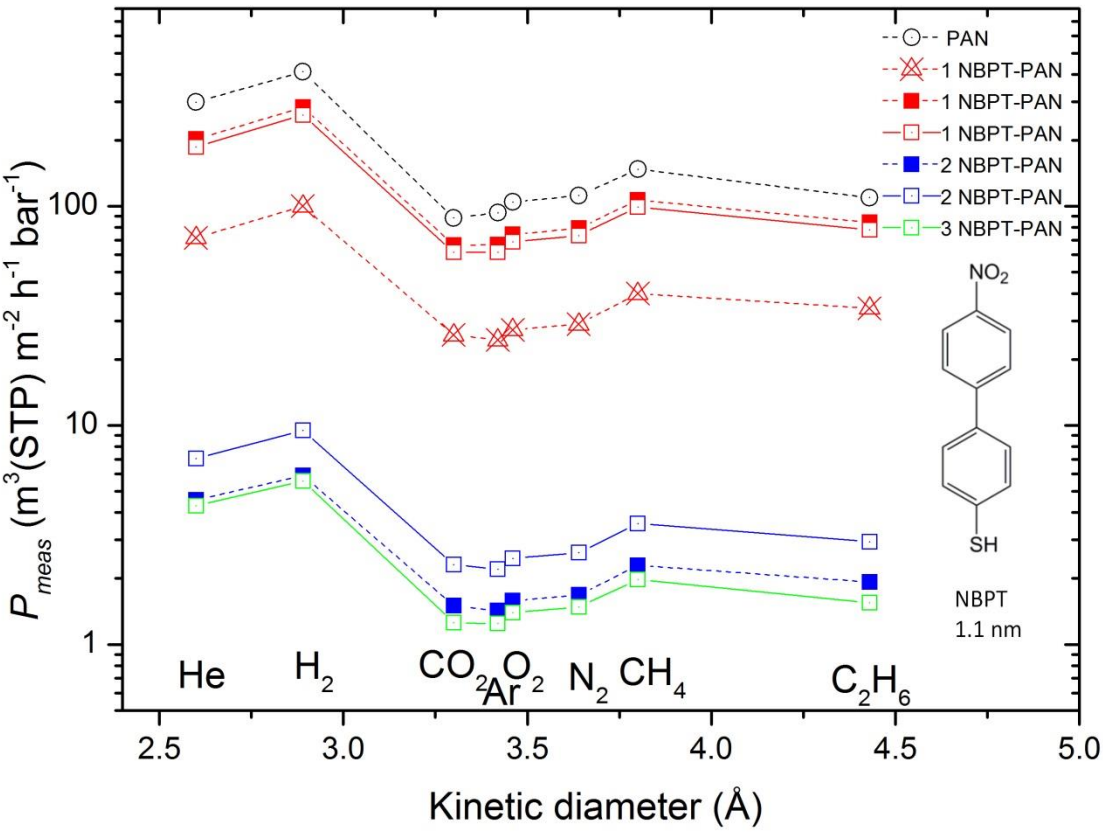

Fig.29 Measured gas permeances of single- and multi-layer NBPT-CNMs on PAN support in relation to the kinetic diameters of gases (He, H_2,CO_2, Ar, O_2, N_2, CH_4, C_2H_6).

Nevertheless, single- and multi-layer NBPT-CNMs were transferred onto a porous PAN and examined for gas permeation. The results are depicted in Figure 29. As is shown in

Figure 29, the curves of measured permeances of single- and multi-layer NBPT-CNMs on a PAN have the same shape as the reference PAN support. In addition, it has been observed that there is big variation in measured permeances for each set of N-layers of CNMs (single-, double- and three-layer) on a PAN support. It can be interpreted by large amount of defects for each sample and the high gas permeance of a PAN compared with a PDMS. Moreover, it has been detected that the gas selectivity of the PAN was almost unchanged after deposition of single- and multi-layer NBPT-CNMs on the PAN. Thus, the transfer of the CNM on the PAN had little effect on the gas permeation characteristics of the CNM-PAN stack. Therefore, it was not possible to extract intrinsic CNM gas permeation characteristics, considering the large impact of PAN permeance in the measured permeance of NBPT-CNM-PAN.

Chapter 5

Results for gas permeation of different CNMs

In order to verify the results of gas permeation of NBPT-CNMs obtained in the work of Min Ai et al. [18], to examine the gas permeation, and to determine the mechanism of gas transport of CNMs, CNMs made of different precursors were fabricated and tested for gas permeation for eight different gases (He, H_2, CO_2, Ar, O_2, N_2, CH_4, C_2H_6). Single gas permeation measurements were conducted for CNMs. The setup for single gas permeation is described in detail in Chapter 4. As has been presented in Chapter 2, gas permeation of a single-layer NBPT-CNM and a single-layer BPT-CNM showed molecular sieve-like properties for the abovementioned gases [18]. On the basis of the results of gas permeation of multilayer CNMs, it was assumed that there is a lateral diffusion between the layers [18]. Despite this, gas permeation of multilayer CNMs show the same molecular-sieve like properties for the two smallest gases, He and H_2 [18]. The interpretation of the results of gas permeation of NBPT-CNMs and the desire to improve gas selectivity of CNMs lead us to fabricate and examine CNMs, which are made of different precursor molecules, for gas permeation. The precursor molecules were chosen based on the structures and characteristics of SAMs. The idea is that the properties of molecules, which are the polarity of molecules, the length of molecules, the packing density of SAMs, and the carbon density of molecules can have an impact on the gas permeation of CNMs. However, we want to initially verify the results of gas permeation of NBPT-CNMs, observed in the work of Min Ai et al. [18].

5.1.1 Gas permeation of an NBPT-CNM on a PDMS-TFC membrane

As was shown in Chapter 2, single-gas permeation measurements were conducted for single- and three-layer NBPT-CNMs on PDMS-TFC support for the following eight gases:He, H_2, CO_2, Ar, O_2, N_2, CH_4, C_2H_6. To verify the results of gas permeation of NBPT-CNMs, single-and three-layer NBPT-CNMs were again fabricated (recipe for the preparation of an NBPT-CNM and the transfer of a CNM onto a support is described in the appendix) and then transferred onto PDMS-TFC support-membranes. These samples were sent to Helmholtz-Zentrum Geesthacht, where, in fact, the single gas permeation of all types of CNMs was examined. In Figure 30, below, one can find gas permeance values of single- and three-layer NBPT-CNMs on a PDMS-TFC membrane, as well as the gas permeance of a bare PDMS-TFC membrane, which was employed as the

reference membrane for the measurements. Additionally, the chemical structure of NBPT molecules is depicted in the inset of Figure 30.

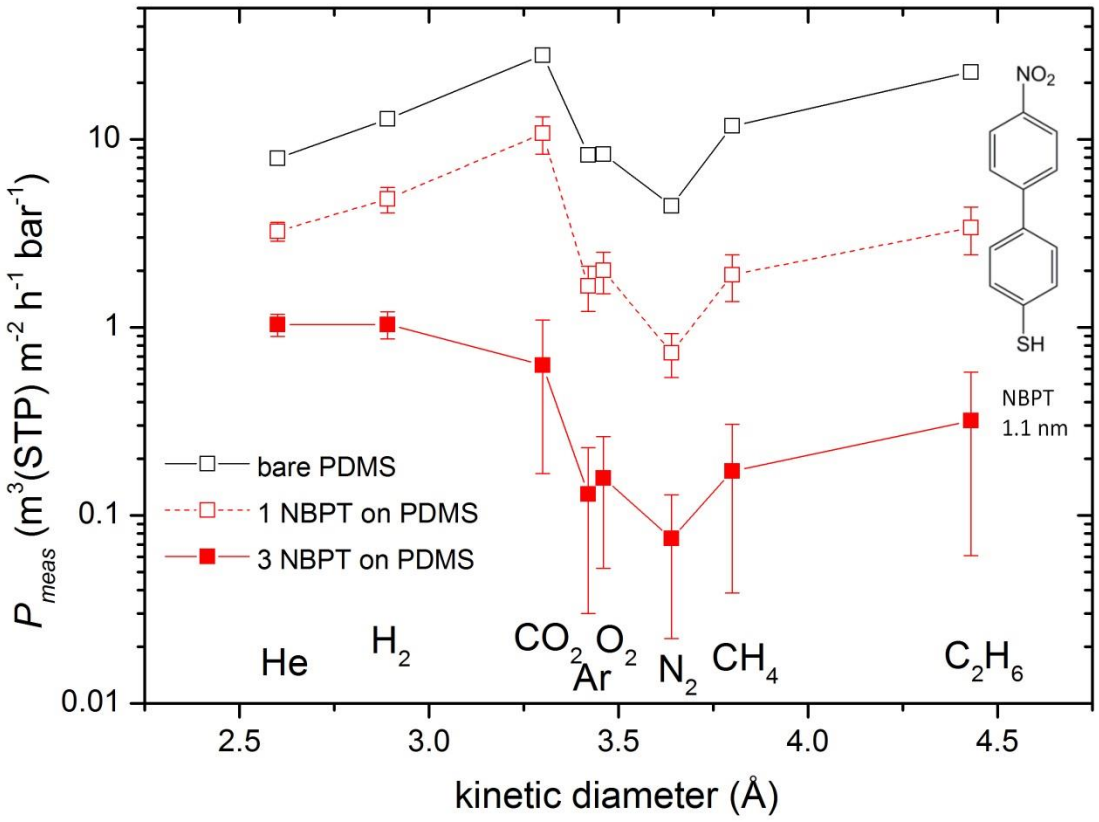

Fig.30 Measured gas permeance of single- and three-layer NBPT-CNM on a PDMS-TFC support in relation to the kinetic diameters of gases (He, H_2, CO_2, Ar, O_2, N_2, CH_4, C_2H_6).

As can be seen in Fig.30, the shape of the permeance curve for a single-layer NBPT-CNM on a PDMS-TFC membrane looks similar to the shape of a bare PDMS. This shows that the gas transport properties of a bare PDMS contribute significantly to the measured permeance of the CNM-PDMS composite membrane. The same features were observed in the work of Min Ai et al. for NBPT-CNMs on a PDMS-TFC membrane [18]. Hence, it is reasonable to consider the changes in permeance of a PDMS-TFC after deposition of NBPT-CNMs, as it was also explored in the work of Min Ai et al. [18]. The relative permeance is presented in Figure 31, which is the ratio of the CNM-PDMS permeances with relation to the reference PDMS-TFC membrane. The deposition of a single-layer NBPT-CNM on a PDMS-TFC reduces the gas permeance of the PDMS to the values ranging from $\sim 80\%$ to $\sim 40\%$. As shown in Figure 31, the decrease of

permeance changes with the kinetic diameter of the gases, and for the smaller gases the decrease lessens. For multilayer CNMs, the decrease of permeance for all gases is much bigger. It varies in the range of ~ 4% to ~ 3% for all gases, except for the two smallest gases—He and H_2. Identical changes in the features of gas permeation were observed in the work of Min Ai et al. [18].

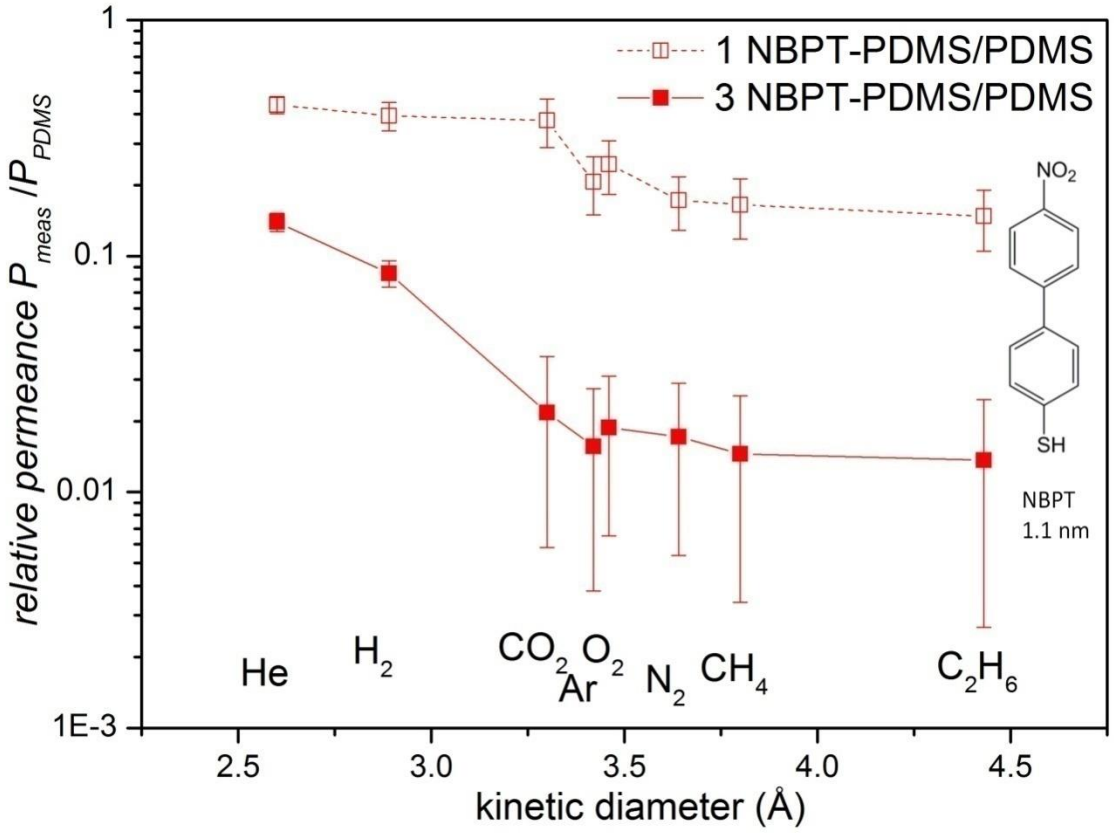

Fig.31 Relative gas permeance of single- and three-layer NBPT-CNMs on a PDMS-TFC compared with a bare PDMS, which is the ratio of the measured permeance values to the corresponding values of the bare PDMS.

The two gases with the smallest kinetic diameters show much higher relative permeances in the case of three-layer NBPT-CNMs in comparison to the larger ones, specifically ~10% for H_2 and ~15% for He. These features cannot be explained as the result of defects as they would increase permeance for all the gases. In addition, it is reproducible for all of the samples. Therefore, it appears that they are related to the intrinsic properties of the CNM, in particular, small gases prefer to permeate through CNMs, and it seems that CNMs show molecular sieve-like behavior. The change in ideal gas selectivity of the PDMS-TFC, after the deposition of NBPT-CNMs onto it, supports the proposed

mechanism of gas transport of CNMs (Table 1, upper part). The ideal gas selectivity is calculated as follows:

$$\alpha_{i/j} = \frac{P_i}{P_j} \tag{14}$$

where P_i and P_j are, respectively, permeances of the single gas measurement for the two gases.

Sample name	H_2/N_2	H_2/CO_2	He/H_2	He/N_2	CO_2/N_2
PDMS	2,81	0,38	0,61	1,72	7,32
single-layer NBPT/CNM on PDMS	7.15±1,11	0.46±0.04	0.68±0.03	4.96±1.02	15.15±0.89
three-layer NBPT/CNM on PDMS	31±13.88	3.78±1.47	1±0.03	31.61±14.03	8.2±1.04
Sample name	H_2/N_2	H_2/CO_2	He/H_2	He/N_2	CO_2/N_2
PDMS	3.05	0.39	0.61	1.86	7.76
single-layer NBPT/CNM on PDMS	5.73±0.16	0.58±0.11	0.71±0.03	4.10±0.28	10.2±1.7
three-layer NBPT/CNM on PDMS	9.9±1.4	1.90±0.13	1.14±0.01	11.4±1.7	5.20±0.48

Table1 Ideal gas selectivity of NBPT-CNM-PDMS-TFC membranes. The results of this study are depicted in the upper section of the table, and the results of Min Ai et al. are presented in the lower section [18].

It has been observed that gas selectivity increases with small gases (He or H_2), which seems to be consistent with molecular sieve-like properties (Table 1, upper part). For instance, He/N_2 and H_2/N_2 gas selectivities of the PDMS-TFC increase after the deposition of a three-layer NBPT-CNM, from 1.72 to 31.61 and from 2.81 to 31, respectively. There is also a slight increase after deposition of single-layer NBPT-CNM onto a PDMS-TFC. Moreover, the increase of He/H_2 gas selectivity of the PDMS-TFC from 0.61 to 1, after the deposition of a three-layer of NBPT-CNM, indicates the assumed molecular sieve-like behavior of NBPT-CNMs. The gas permeation in the case of molecular sieving assumes higher permeance of the smaller He gas, in comparison to the large H_2 gas. The low He/H_2 gas selectivity of the PDMS-TFC, where a solution-diffusion mechanism occurs, is interpreted as follows: the diffusion and/or solubility coefficients of H_2 are higher with respect to He in the PDMS. Hence, the He/H_2 gas selectivity is below 1 for a PDMS, specifically 0.61. Furthermore, the CO_2/N_2 gas selectivity of the PDMS-TFC increases considerably even with the deposition of a single-layer of NBPT-CNM. Surprisingly, after the deposition of a three-layer NBPT-CNM on

the PDMS-TFC, the CO_2/N_2 gas selectivity of the PDMS-TFC decreases to an even lower value. This finding indicates that CO_2 permeation is hindered in the case of multi-layer NBPT-CNMs. The abovementioned features of gas selectivity after the deposition of NBPT-CNMs on a PDMS-TFC were also observed in the work of Min Ai et al. (Table 1, lower part) [18].

The comparison of ideal gas selectivities in Table 1 (upper and lower parts) shows the same changes of gas selectivity characteristics after deposition of NBPT-CNMs on PDMS-TFCs, with the only difference being that the results obtained in this work show slightly higher gas selectivity values, which can be modified by obtaining better samples with less defects.

5.1.2 Extraction of intrinsic gas permeance of CNMs from measured values

So far, the aforementioned analysis and discussion consider changes in the gas permeation properties of bare PDMS-TFC membranes after deposition of single- and three-layer NBPT-CNMs. However, the properties and mechanism of gas permeation through CNMs without PDMS contribution is the key aspect for this study. Therefore, in order to extract the corresponding permeance of a CNM, itself, from the measured values of a CNM-PDMS, a so-called "resistance model" is applied.

5.1.3 Resistance model

The intrinsic gas permeance of a CNM can be extracted from the measured value of the CNM-PDMS composite membrane by considering it as a stack of two individual layers with corresponding permeances P_{CNM} and P_{PDMS}, respectively, for the CNM and PDMS-TFC (Fig.32). These two permeances are related to the measured NBPT-CNM-PDMS-TFC permeance $P_{CNM-PDMS}$ as follows [106]:

$$\frac{1}{P_{CNM-PDMS}} = \frac{1}{P_{CNM}} + \frac{1}{P_{PDMS}} \tag{15}$$

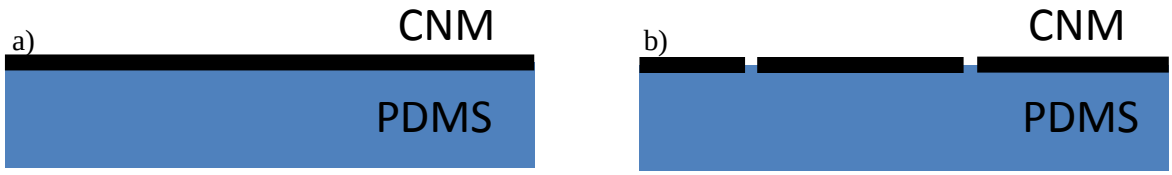

Fig.32 Schematic representation of a CNM-PDMS composite membrane by considering it as a stack of two layers: a) without defects and b) with defects.

Equation 15 is valid only in the case of the absence of any defects in CNMs on a PDMS-TFC. Nevertheless, HIM detects micron-sized defects in CNMs on a PDMS-TFC (Fig.33) [18]. As can be seen from Figure 33, only a small part of the PDMS is not covered by the CNM. Thus, taking into consideration the defects, measured permeance P_{meas} can't be equal to the permeance of $P_{CNM-PDMS}$ in Eq.15. P_{meas} relates to the $P_{CNM-PDMS}$ as follows [18]:

$$P_{meas} = P_{CNM-PDMS}\frac{A_{CNM}}{A_{PDMS}} + P_{PDMS}\left(1 - \frac{A_{CNM}}{A_{PDMS}}\right) \quad (16)$$

where A_{CNM}/A_{PDMS} is the relative surface coverage of a CNM on a PDMS-TFC support. Taking into account these two equations, Eq.15 and Eq.16, P_{CNM} can be defined, which relates to the characteristic permeance of CNM, itself.

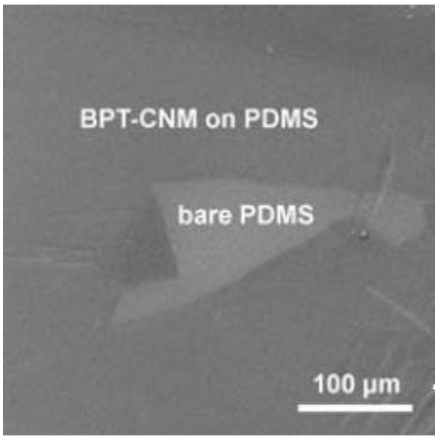

Fig.33 HIM image of a BPT-CNM on a PDMS: it reveals micron-sized defects [18].

The calculation of permeance P_{CNM} requires a value for the relative surface coverage A_{CNM}/A_{PDMS}. The relative coverage A_{CNM}/A_{PDMS} can be estimated for each sample with the following procedure: in the first step, Equations 15 and 16 yield permeance P_{CNM} as a function of relative coverage A_{CNM}/A_{PDMS}:

$$P_{CNM} = \frac{P_{PDMS}^2\left(1 - \frac{A_{CNM}}{A_{PDMS}}\right) - P_{PDMS}P_{meas}}{P_{meas} - P_{PDMS}} \quad (17)$$

In the next step, the permeance P_{CNM} is plotted in relation to the kinetic diameter of the gases for all possible values of A_{CNM}/A_{PDMS} (as shown in Figure 34) [18]. For the assumed perfect CNM coverage on the PDMS-TFC (A_{CNM}/A_{PDMS}= 100 %), the shape of

the P_{CNM} curve is, in part, similar to that of the bare PDMS-TFC profile, which is also displayed as a dashed line in Figure 34. This similarity of the P_{CNM} curve decreases by reducing A_{CNM}/A_{PDMS} to a certain value, which is 96.4% in this case (Fig.34). When A_{CNM}/A_{PDMS} continues to be reduced, it results in an increase of the features in an inverted form, and permeance values also become negative for some gases. It is expected that the correct value for A_{CNM}/A_{PDMS} results in a P_{CNM} curve, which shows the least similarities to the P_{PDMS} profile. The evaluation assumes that the permeance characteristics of a CNM are different from those of a PDMS, in relation to the gas species. This assumption is supported by the change of the relative permeance for different gas types in Figure 31 and by the observed amplification of the ideal gas selectivity, for example, CO_2/N_2 [18].

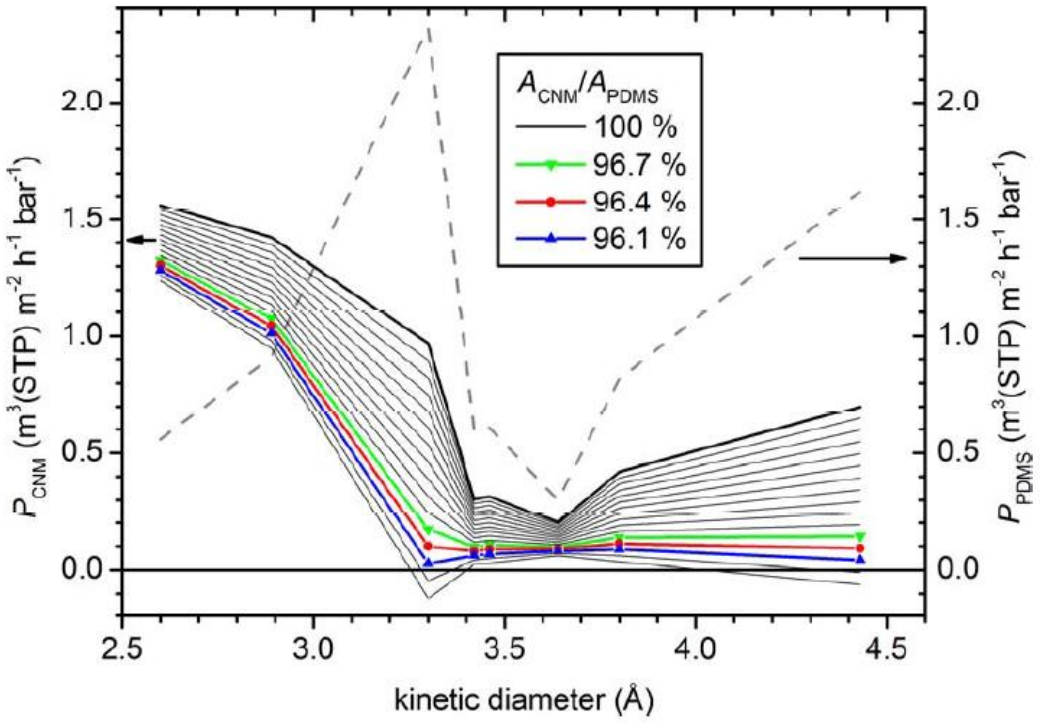

Fig.34 Possible intrinsic permeance values P_{CNM} for an individual three-layer BPT-CNM sample. The displayed values were defined for different relative surface coverages A_{CNM}/A_{PDMS} by applying the measured permeances, as well as, Equation 4. The difference of A_{CNM}/A_{PDMS} between two adjacent curves is 0.03 %. P_{PDMS} is also shown as a dashed line for comparison [18].

Any deviation of this value is expected to result in curves that are more similar to P_{PDMS}. Additionally, the wrong relative coverage will result in a superposition of P_{CNM} and P_{PDMS}. Therefore, the one showing the least similarities between P_{CNM} and P_{PDMS} is

chosen. In this case, P_{CNM} corresponds to A_{CNM}/A_{PDMS} = 96.4% [18]. Upper and lower limits of A_{CNM}/A_{PDMS} are chosen, which correspond to the curves with a recognizable increase in similarities to the P_{PDMS}. These values estimate the uncertainty of A_{CNM}/A_{PDMS}. The relative surface coverage A_{CNM}/A_{PDMS} for this sample is estimated to be 96.4±0.3% [18]. To conclude, the method of evaluation of relative coverage is based on the minimization of PDMS-TFC characteristics on the final permeance P_{CNM}. Therefore, P_{CNM} corresponds to the permeance of defect-free CNM patches without a support layer.

5.1.4 The intrinsic properties of gas permeation of NBPT-CNM

If the resistance model is applied to the measured gas permeance values of an NBPT-CNM on a PDMS-TFC, it gives the following results for the intrinsic gas permeance of an NBPT-CNM, depicted in Figure 35.

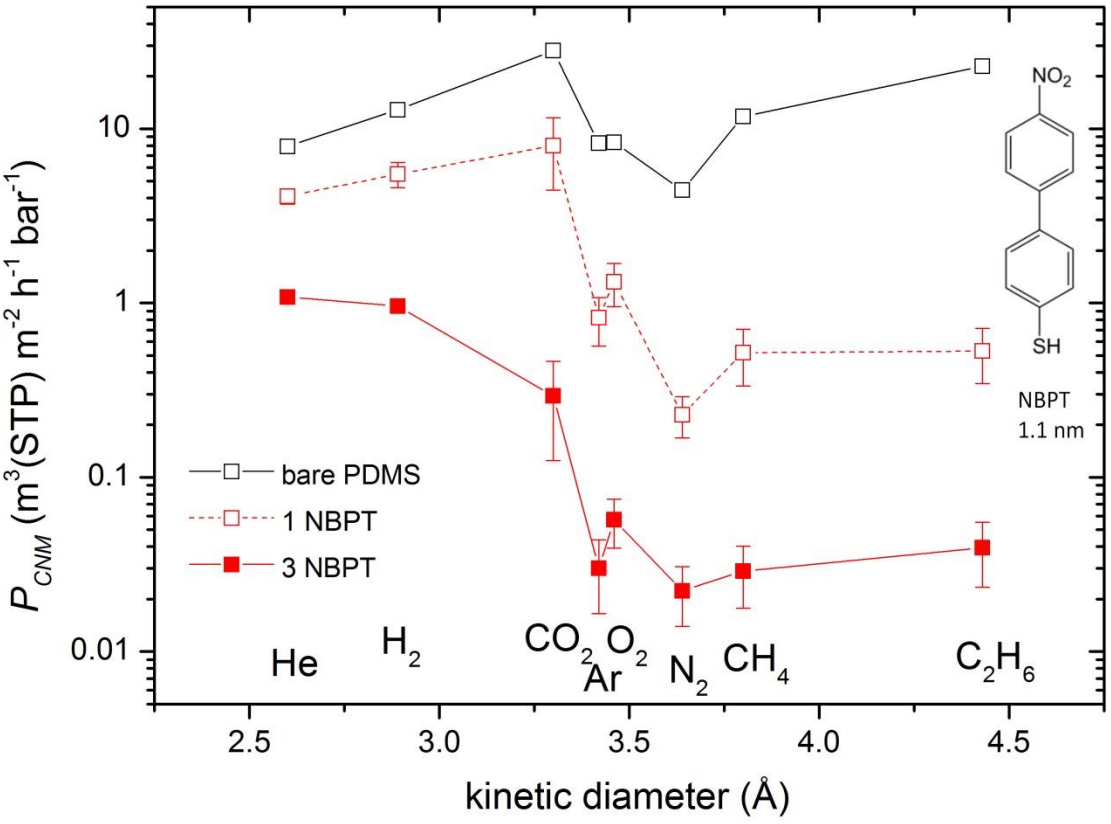

Fig.35 Intrinsic gas permeance values of P_{CNM} for single- and three-layer NBPT-CNMs estimated by applying the resistance model.

The results in Figure 35 show that the three-layer NBPT-CNM performs very low gas permeance for all gases, with the exception of two gases with the smallest kinetic diameters (He and H_2). This show more than one order of magnitude higher permeance compared with the other gases. These features reinforce the assumption that high gas permeance is the intrinsic property of an NBPT-CNM, which is consistent with molecular sieving-like behavior.

For single-layer NBPT-CNM, in addition to He and H_2, gas permeance of CO_2 is also much higher compared with the other gases (Fig.35). These findings again coincide with the results in the work of Min Ai et al. (Fig.10). It can be assumed that there are molecular-sized channels in the CNMs, and they dominate the gas permeation (Fig.36a) [18]. Therefore, the small gases (He, H_2, CO_2) permeate through CNMs and bigger gases are blocked. This interpretation of the gas permeation property of an NBPT-CNM is also consistent with the increase of gas selectivity towards small gases after deposition of single-layer of an NBPT-CNM onto a PDMS-TFC membrane (Table 1).

The presumed "openings" or "channels" may form during the cross-linking process, due to its statistical nature, which results in a random variation of intermolecular distances [18]. Moreover, the result for a single-layer NBPT-CNM shows no chance of Knudsen diffusion occurring in a single-layer CNM. As for single-layer CNMs, the permeance of methane and ethane are quite similar, despite their difference in the molecular weight. Additionally, the heaviest gas molecule, CO_2, shows much higher permeance than Ar, O_2, N_2, CH_4, C_2H_6 gases [18].

For three-layer NBPT-CNMs, unlike single-layer NBPT-CNM, the gas permeance of CO_2 is not high (Fig.35). As it is less likely that the proposed openings are found at the same places in the case of multi-layer CNMs, the gases will need to permeate horizontally between the layers after passing vertically through the proposed channels in a single-layer CNM (Fig.36b) [18]. The assumption of lateral diffusion between the layers of multi-layer CNMs, which was offered in the work of Min Ai et al. [18], is consistent with the results obtained in this work. Both possible mechanisms, which were suggested for transport of gases between the layers, prefer the transport of smaller gases (Knudsen-like diffusion or condensation and surface flow of gases) [18]. The diffusion of the smallest gases (He and H_2) is higher compared with the larger gases, including CO_2.

The proposed mechanism is also consistent with the increase of CO_2/N_2 gas selectivity of a PDMS-TFC after the deposition of a single-layer NBPT-CNM, and the absence of this increase after the deposition of a three-layer NBPT-CNM.

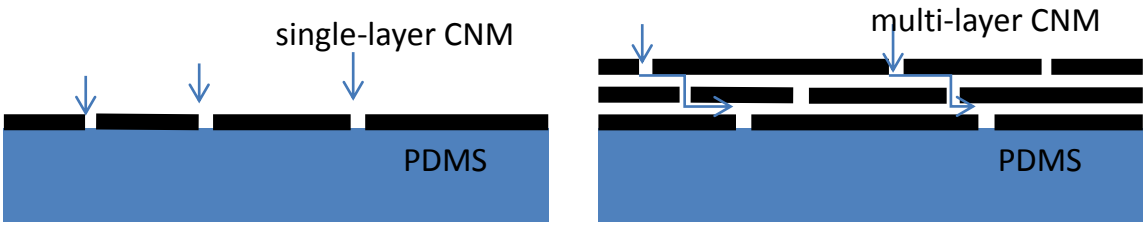

a) b)

Fig.36 Schematic representation of a) the proposed model of gas permeation through a single-layer CNM. The single-layer CNM shows molecular sieving-like properties. b) Proposed model of gas permeation through multi-layer CNMs. Lateral diffusion may additionally be involved.

To sum up, the reproducibility of gas permeation measurements for single- and three-layer NBPT-CNMs on a PDMS-TFC verifies the results and conclusions related to the proposed mechanisms and properties of gas permeance through NBPT-CNMs, presented in Chapter 2 [18].

5.2 Gas permeation of CNMs made from different precursors

The mechanism of gas permeance of CNMs has been proposed based on the results of gas permeance of NBPT- and BPT-CNMs on a PDMS-TFC membrane, which says that single-layer CNMs show molecular sieving-like properties, and for multilayer there is lateral diffusion of gases in between the CNMs [18]. Reproducibility of the results, as shown above, has confirmed the abovementioned hypothesis regarding the mechanism of gas permeation of CNMs. Based on the assumed origin of the “channels” in CNMs, new precursors for the fabrication of SAMs were chosen with the assumption of a variation in intermolecular distances and properties of SAMs. Thus, it might have an effect on the gas permeation characteristics of CNMs.

Freestanding CNMs with thicknesses between 0.6 and 1.7 nm, made from SAMs of different polyaromatic precursors via low-energy electron-induced cross-linking, can be formed, as shown in the work of Angelova et.al [90]. The properties of the resulting CNMs can be flexibly adjusted. It has been reported that SAMs from 1-terpheny-4-thiol

(TPT) and naphthalene-2-thiol (NPTH) form densely packed ($\sqrt{3}\times\sqrt{3}$) unit cell of adsorption sites [90]. In addition, the carbon density of SAMs has been measured from the thicknesses of SAMs and the area per molecule. It showed high carbon density for NPTH- and TPT-SAMs (Table 2) [116]. Moreover, it has been presented that the area per molecule is the smallest for NPTH- and TPT-SAMs.

precursor molecules	thickness of SAM [Å]	structure of SAM	area per molecule [$Å^2$]	carbon density [nm^{-3}]	Young's modulus [GPa]
BPT	10	2×2	28.7	42	9.9
TPT	12	$\sqrt{3}\times\sqrt{3}$	21.6	64	9.0
NPTH	6	$\sqrt{3}\times\sqrt{3}$	21.6	77	18.6
2MP	9	n.a.	n.a.	n.a.	15.2
HPB	8	n.a.	n.a.	n.a.	17.5
HBC	19	n.a.	n.a.	n.a.	12.9

Table 2 Thickness, structure, and carbon density of pristine SAMs and Young's Modulus of CNMs [116].

The first example of new precursor molecules that will be examined is TPT. The chemical structure of the TPT molecule and the thickness of the TPT-CNM are depicted in the inset of Figure 37.

5.3 Gas permeation of TPT-CNMs

As shown in Table 2, SAMs made of TPT molecules are more densely-packed, and the carbon density is higher compared with BPT-SAMs. Hence, in the case of TPT-SAMs, the proposed molecular–sized channels, which are presumably formed after crosslinking, might be smaller and may improve gas selectivity of CNMs. Therefore, single- and three-layer TPT-CNMs were fabricated and then transferred onto PDMS-TFC membranes to test for single gas permeation. Afterwards, the samples were sent to Helmholtz-Zentrum Geesthacht for single gas permeation measurements. The measured gas permeances of a TPT-CNM-PDMS-TFC in relation to the kinetic diameters of the gases are presented in Figure 37.

The shape of the permeance curve for the measured single-layer TPT-CNM on the PDMS looks similar with the shape of the bare PDMS, particularly for the gases larger than CO_2. The deposition of the single-layer TPT-CNM onto the PDMS-TFC reduces the gas

permeance of the PDMS-TFC to values ranging from ~ 5 % to ~ 25 %. In the case of small the gases (He, H_2 and CO_2), the permeances are much higher compared with the

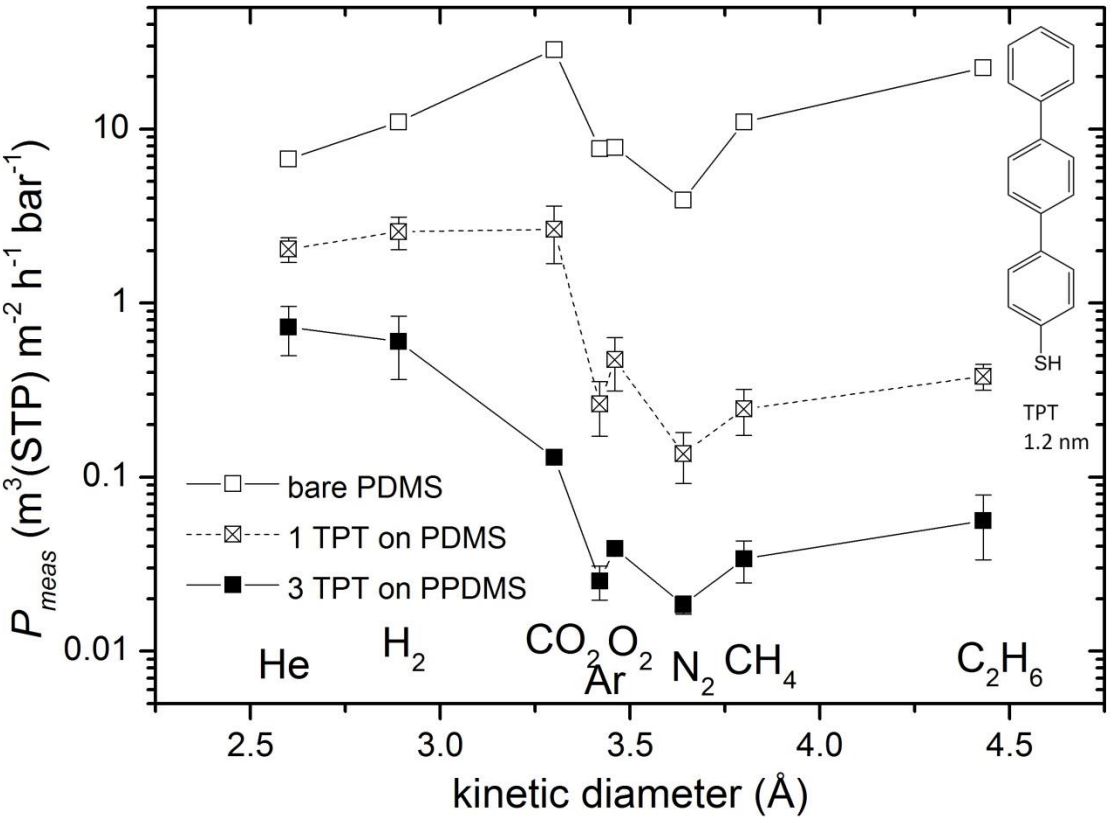

Fig.37 Measured gas permeance of single- and three-layer TPT-CNMs on a PDMS support in relation to the kinetic diameters of gases (He, H_2, CO_2, Ar, O_2, N_2, CH_4, C_2H_6).

larger gases, and the values are almost in the same range. This indicates that after the deposition of a single-layer TPT-CNM on a PDMS-TFC, the stack of CNM-PDMS membranes show preferences in gas transport towards small gases. Moreover, before applying the "resistance model" in order to obtain the intrinsic properties of a TPT-CNM, it is noticed that after the deposition of a single-layer TPT-CNM onto a PDMS-TFC, the stack of membranes indicate molecular sieving-like behavior. Nevertheless, for three-layer TPT-CNMs the decrease of permeance is much bigger. In particular, the permeance decreases to the values in the range of ~ 1% for all the gases, except for the two smallest gases (He and H_2). The two gases with the smallest kinetic diameters show much higher relative permeances for three-layer TPT-CNMs, with ~5% for H_2 and ~10% for He. In addition, the ideal gas selectivity of a bare PDMS-TFC increases with small gases after

the deposition of a TPT-CNM. This behavior is also consistent with molecular sieving-like properties (Table 3).

Sample name	H_2/N_2	H_2/CO_2	He/H_2	He/N_2	CO_2/N_2
PDMS	3.05	0.39	0.61	1.86	7.76
single-layer TPT/CNM on PDMS	19.68 ± 2.41	1.03 ± 0.17	0.8 ± 0.04	15.87 ± 2.74	19.16 ± 0.84
three-layer TPT/CNM on PDMS	34.29 ± 16.71	4.72 ± 2.05	1.25 ± 0.11	41.51 ± 17.42	7.07 ± 0.50

Table 3 Ideal gas selectivity of TPT-CNM-PDMS membranes.

In particular, H_2/N_2 and He/N_2 gas selectivity of a bare PDMS-TFC increases to higher values after deposition of a TPT-CNM. Moreover, taking into consideration that He/H_2 gas selectivity exceeds 1, the proposed mechanism of gas transport becomes more apparent. As shown in Chapter 5.1.1, the value 0.61 is consistent with the solution-diffusion mechanism in the case of the bare PDMS-TFC. Furthermore, He/H_2 gas selectivity becomes higher than 1 after deposition of the three-layer TPT-CNM, which is expected in the case of molecular sieving. These two factors are consistent with the proposed hypothesis that TPT-CNMs act as molecular sieves, as it was also assumed for NBPT-CNMs.

In fact, the intrinsic properties of gas permeation of TPT-CNMs are of great interest, as they show the actual performance of TPT-CNMs. Thus, the intrinsic gas permeance for single- and three-layer TPT-CNMs was obtained after applying the "resistance model" to the measured values of the TPT-CNM-PDMS. As can be seen in Figure 38, the intrinsic gas permeance of the single-layer TPT-CNM shows more than one order of magnitude higher permeance for gases with the smallest kinetic diameter (He, H_2 and CO_2) in comparison with the larger gases (Ar, O_2, N_2, CH_4 and C_2H_6). This might be an indication of a molecular sieving effect, which seems to occur in the case of single-layer of TPT-CNMs. For three-layer TPT-CNMs, the permeance for He and H_2 gases is significantly higher in comparison with other gases, including CO_2. This finding once again indicates that single-layer TPT-CNMs shows molecular sieving-like properties. For three-layer TPT-CNMs, there is a lateral diffusion in between the layers. Therefore, the conclusion is the same, as it is for the three-layer NBPT-CNM.

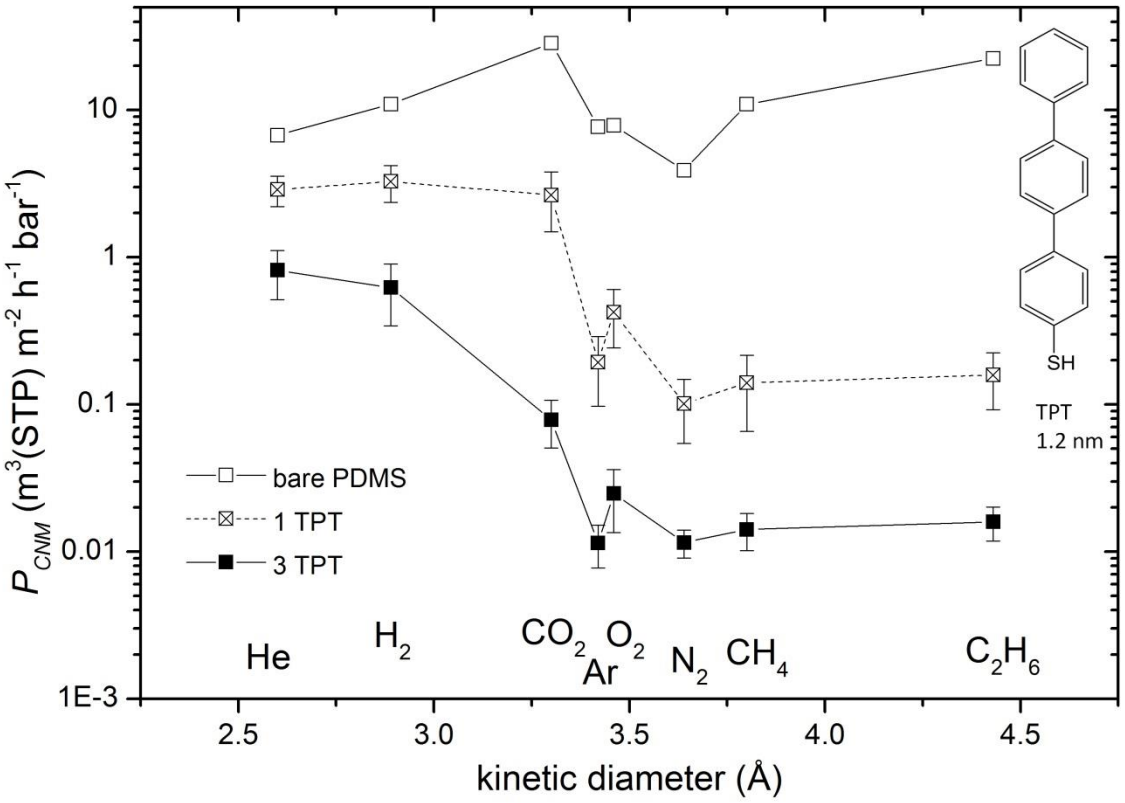

Fig.38 Intrinsic gas permeance values of P_{CNM} for single- and three-layer TPT-CNMs defined by applying the resistance model.

Taking into consideration the results obtained for CNMs made from two different precursors that are NBPT and TPT, one can see that both CNMs show the same characteristics for gas permeation, though SAMs made from these molecules show different properties regarding packing density and carbon density [90]. The difference is that the intrinsic gas permeance of CNMs is shifted to the lower values with the increase in the thickness of CNMs (Fig.39). The shift of gas permeance might be interpreted due to the thickness difference, as the permeance of a thinner CNM is supposed to be higher. Additionally, if we compare the gas selectivity of these two CNMs (Table 1 and Table 3), the selectivity of the CNM-PDMS composite membrane shows a bit higher values in the case of the TPT-CNM, which has a more densely-packed SAM structure.

To sum up, gas permeance of two different CNMs made from different precursors, shows the same gas permeation characteristics, with the only difference being that the gas permeance is shifted with respect to the thickness of the CNM. In particular, if the thickness of the CNM is increased by changing the precursor molecule, the absolute

value of gas permeance decreases, as one can see in Figure 39 in the case of the NBPT-CNM and the TPT-CNM.

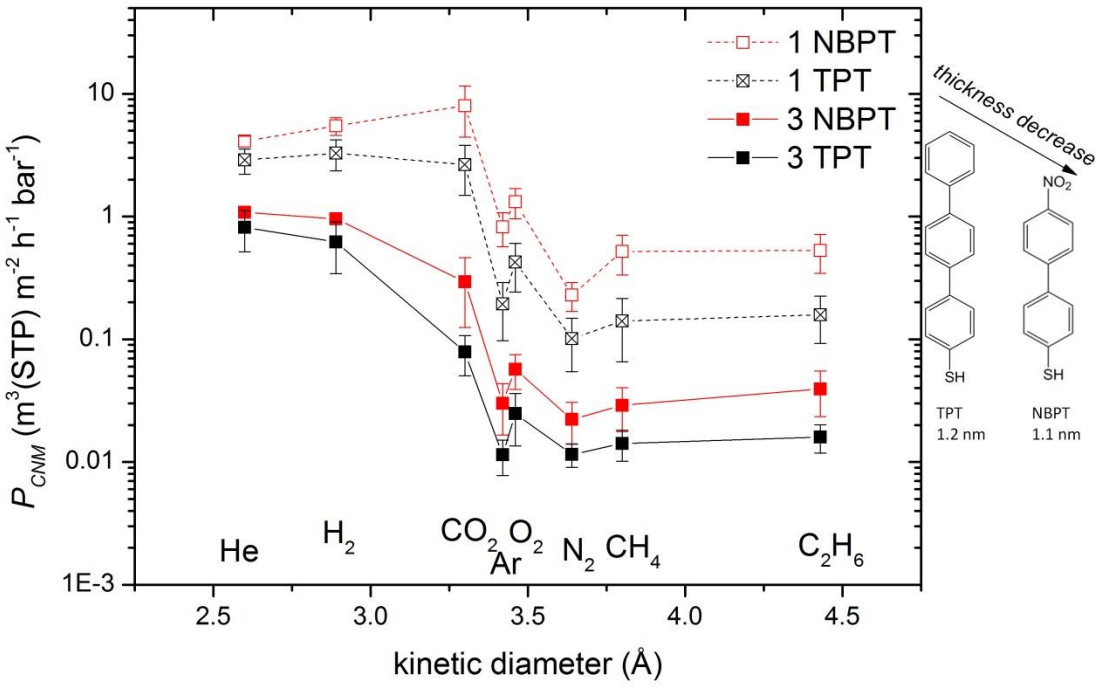

Fig.39 Comparison of intrinsic gas permeances P_{CNM} between TPT-CNMs and NBPT-CNMs.

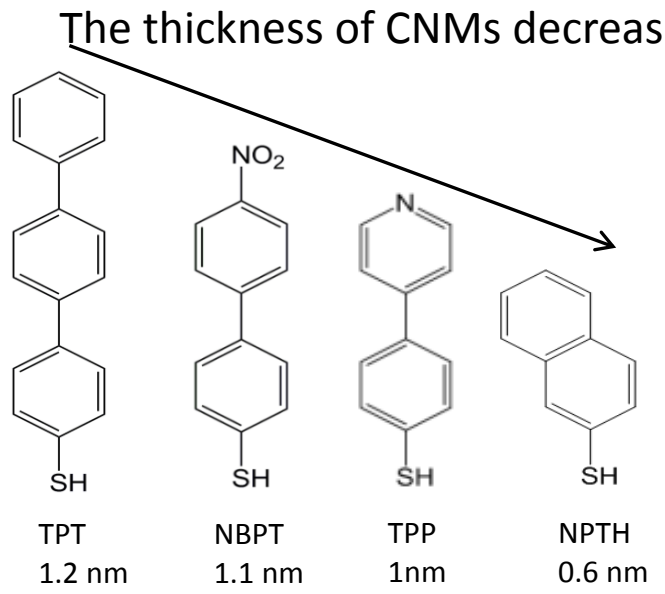

Fig.40 The chemical structures of the different precursor molecules for CNM fabrication are depicted here. The CNMs are examined for single gas permeation measurements. Below each chemical structure of the molecules, the thickness of each CNM can be found.

5.4 Fabrication and gas permeation of TPP-CNMs

Another approach to enhance gas selectivity of carbon nanomembranes (CNMs) is fabrication of a CNM from nitrogen-doped aromatic molecule TPP (4-(4-thiophenyl)pyridine), which is depicted in Figure 40. It is expected that the nitrogen atom, which is doped in a phenyl ring, will change the polarity of the precursor molecule and will influence the gas permeation of the CNM due to the interaction between the N-atom and gas molecules: dipole-quadrupole interaction. Therefore, the changes in polarity will probably enhance gas selectivity. The first step of this approach is to check whether it is possible to form the SAM, and then the CNM from it.

To investigate the possible formation of a TPP-SAM in a solution, ~10 mM solutions of a TPP molecule in dry and degassed chloroform and dimethylformamide (DMF) were prepared. Afterwards, the gold/mica substrates were immersed into the solutions in sealed flasks under nitrogen. The samples were removed after 24 and 72 hours, an XPS was employed to explore the possible SAM formation. For the samples immersed in chloroform solution, no sign of sulfur and nitrogen peaks were detected, which yields to the absence of the formation of a TPP-SAM in the chloroform solution. In the case of the DMF solution, XPS spectrum of N1s, C1s, and S2p showed identical results for the two immersion time periods (Fig.41). The sulfur signal consists of a doublet with S2p3/2 and binding energy of 162.0 eV, which demonstrate the formation of sulfur-gold bonds (Fig.41, left side). The SAM is formed due to the strong bonds between the sulfur and gold atoms that are accompanied by Van der Waals interactions between the carbon atoms. Aromatic carbon contributes to the C1s signal at BEs of ~284.2 eV (Fig.41). After the irradiation of TPP-SAM in a high vacuum (<5×10-7 mbar), with an electron flood-gun at electron energy of 100 eV and 50 mC/cm^2 dose, the S2p signal shows the formation of a second doublet at higher binding energies (ca. 163.5 and 164.7), which is indicative of the formation of sulfide or disulfide in the cross-linked TPP-SAM (Fig.41, right side). Since the sample that was immersed for 24 hours in the DMF solution showed an identical XPS spectrum as sample immersed for 72 hours, the 24 hours immersion time seemed to be sufficient for the TPP-SAM formation (Fig.41, left side). Using attenuation of gold peak, the thickness of the TPP-SAM was calculated. The thickness of

the TPP-SAM was 1.1 nm, and after irradiation with a 50 mC/cm^2 dose, the TPP-CNM thickness became 1 nm.

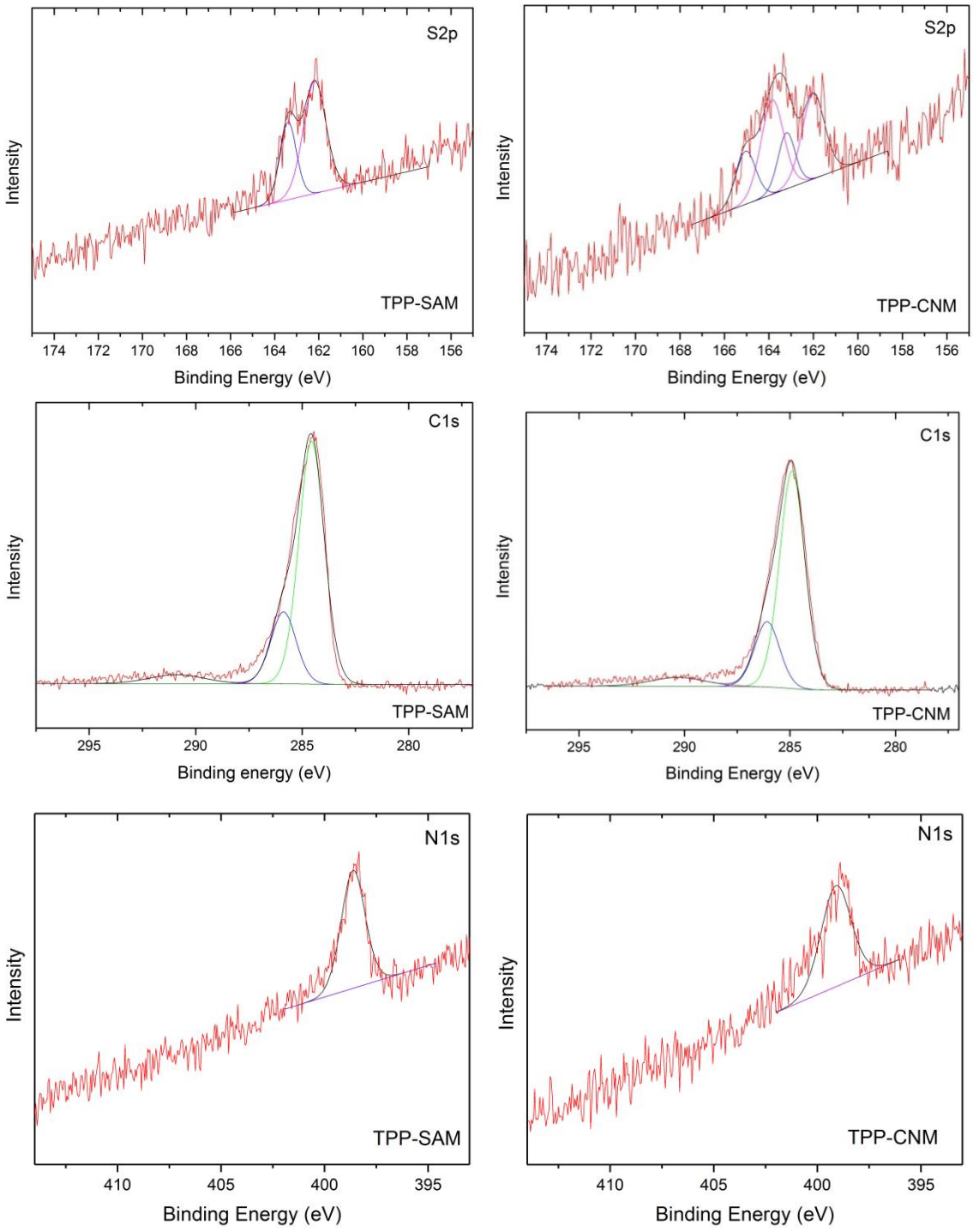

Fig.41 The XPS spectrum of N1s, C1s, and S2p signals of the TPP-SAM are depicted before (left side) and after (right side) irradiation with a 50 mC/cm^2 dose.

In addition, the samples of TPP-CNMs were imaged by a light optical microscope after their transfer onto a silicon oxide (Fig.42). These images indicated that TPP-CNMs showed full coverage for both cases, and micro-sized defects were not detected at higher magnification. This confirms that 24 hours of immersion of a TPP in a DMF solution is sufficient for TPP-SAM formation, and subsequently TPP-CNM formation.

a)

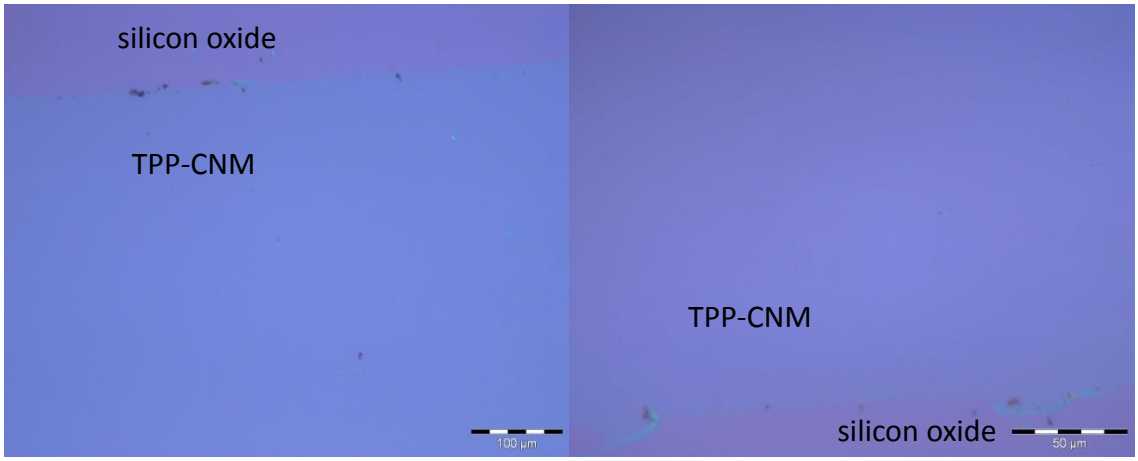

b)

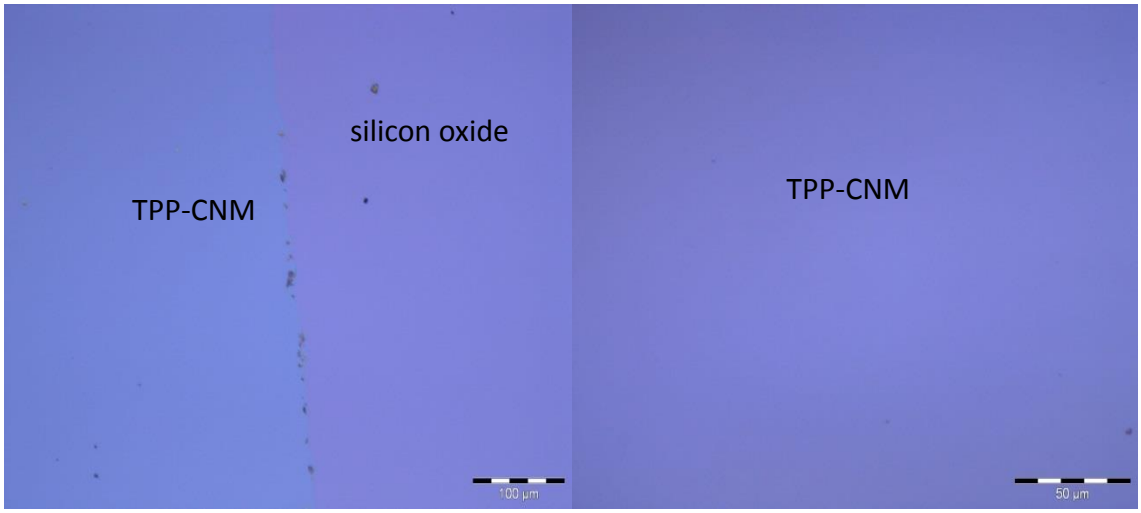

Fig.42 Optical microscope images of a TPP-CNM at different magnifications**:** TPP-CNM made from TPP-SAM immersed into a DMF solution of TPP molecules for a) 24 hours and b) 72 hours.

Moreover, a TPP-CNM was transferred onto copper TEM grids and carbon lacey, and was investigated by an HIM to examine for a freestanding CNM. The HIM images on copper TEM grids showed that a free-standing CNM can form from a TPP-CNM with 40

μm regular openings (Fig.43). Furthermore, the images depicted in Fig.44 reveal a freestanding CNM on carbon lacey grids.

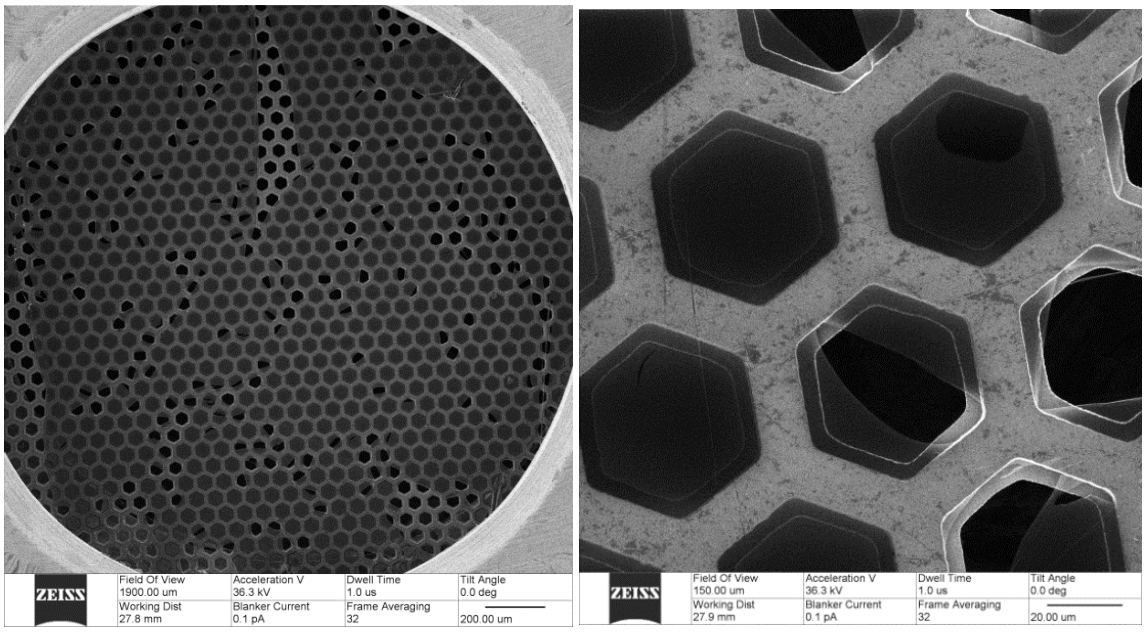

Fig.43 HIM images of a TPP-CNM on copper TEM grids with 40 μm regular openings. It exhibits a free-standing CNM.

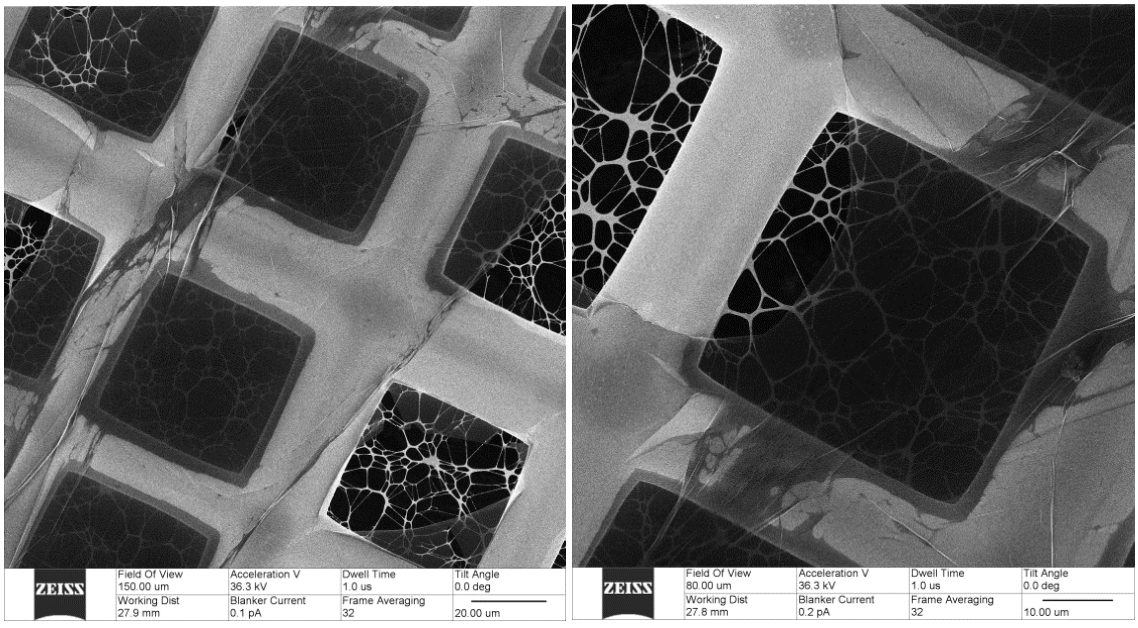

Fig.44 HIM images of a TPP-CNM on carbon lacey grids. It exhibits a free-standing CNM.

Based on the XPS observations of TPP-SAMs and the HIM and XPS observations of irradiated TPP-SAMs, it was concluded that a free-standing TPP-CNM can be fabricated. Following the fabrication of freestanding TPP-CNMs, single- and double-layer TPP-CNMs were fabricated and transferred onto PDMS-TFC membranes to test for gas permeation with regard to the eight gases (He, H_2, CO_2, Ar, O_2, N_2, CH_4, C_2H_6). The measured gas permeance of single- and double-layer TPP-CNMs on a PDMS-TFC yields that the gas permeance of a PDMS-TFC is slightly decreased after the deposition of a double-layer TPP-CNM onto it. This slight decrease appeared in the case of all three copies of double-layer TPP-CNM onto a PDMS-TFC (Fig.45). This can be interpreted by difficulties that occur during the stacking of multi-layer of TPP-CNM, particularly considering the successful transfer of a single-layer TPP-CNM onto a PDMS-TFC. In the case of the deposition of a single-layer of TPP-CNM onto a PDMS-TFC, the decrease of permeance of a PDMS-TFC is distinct, in the range of ~ 50 % (Fig.45).

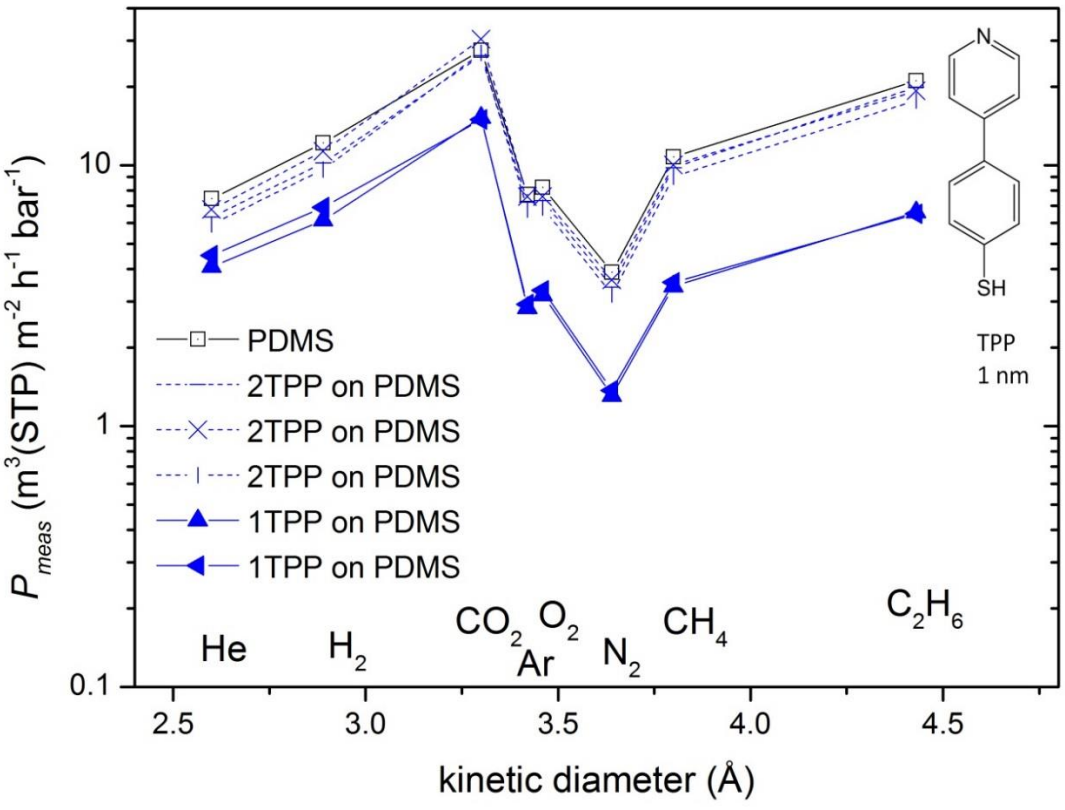

Fig.45 Measured gas permeance of copies of single- and double-layer TPP-CNMs on a PDMS-TFC support in relation to the kinetic diameters of gases (He, H_2, CO_2, Ar, O_2, N_2, CH_4, C_2H_6).

The shape of the gas permeance curve for a measured single-layer TPP-CNM on a PDMS-TFC looks similar to the shape of a bare PDMS-TFC, with the only difference being a shift to lower values. The same changes were noticed after the deposition of a single-layer NBPT-CNM on a bare PDMS-TFC. The relative permeance of a TPP-CNM-PDMS in relation to a bare PDMS is depicted in Figure 46, which emphasizes small reduction of gas permeance in the case of small gases (He, H_2 and CO_2) in comparison with the larger ones (Ar, O_2, N_2, CH_4 and C_2H_6). This behavior is consistent with the assumption that TPP-CNMs also act as molecular sieves.

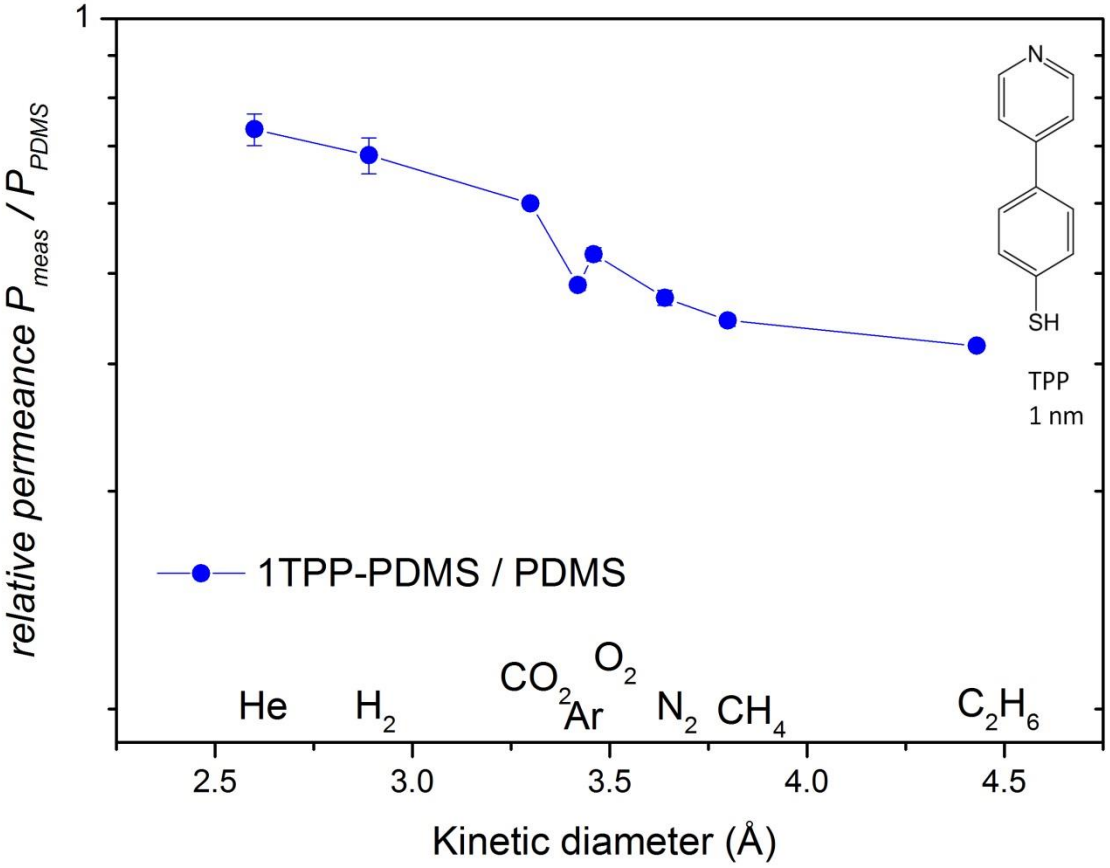

Fig.46 Relative gas permeance of a single-layer TPP-CNM on a PDMS compared with a bare PDMS, which is the ratio of the measured permeance values to the corresponding values of the bare PDMS.

Additionally, the changes in ideal gas selectivity with small gases are considered. In particular, H_2/N_2 or He/N_2 selectivity of a bare PDMS increases after the deposition of a single-layer TPP-CNM. The CO_2/N_2 selectivity, also, increases after the deposition of a single-layer TPP-CNM onto a PDMS (Table 4). These findings indicate molecular

sieving-like properties of TPP-CNMs. In addition, the changes of gas selectivity of a PDMS-TFC are compared in Table 4, after the deposition of single-layer NBPT- and TPT-CNMs. As can be seen in Table 4, the gas selectivity of the PDMS-TFC increases with the variation of the CNMs transferred onto PDMS-TFC, in particular from TPP- to NBPT- to TPT-CNMs.

Sample name	H_2/N_2	H_2/CO_2	He/H_2	He/N_2	CO_2/N_2
PDMS	3.13	0.37	0.6	1.89	8.44
single-layer TPP/CNM on PDMS	4.92±0.16	0.43±0.02	0.65±0.004	3.24±0.08	11.41±0.37
single-layer NBPT/CNM on PDMS	7.15±1,11	0.46±0.04	0.68±0.03	4.96±1.02	15.15±0.89
single-layer TPT/CNM on PDMS	19.68±2.41	1.03±0.17	0.8±0.04	15.87±2.74	19.16±0.84

Table 4 Changes of ideal gas selectivity of a PDMS-TFC after the deposition of a single-layer TPP-, NBPT-, and TPT-CNMs onto it.

The intrinsic properties of TPP-CNMs show the actual performance of the membrane, which is obtained by applying the resistance model, described above (Fig.47).

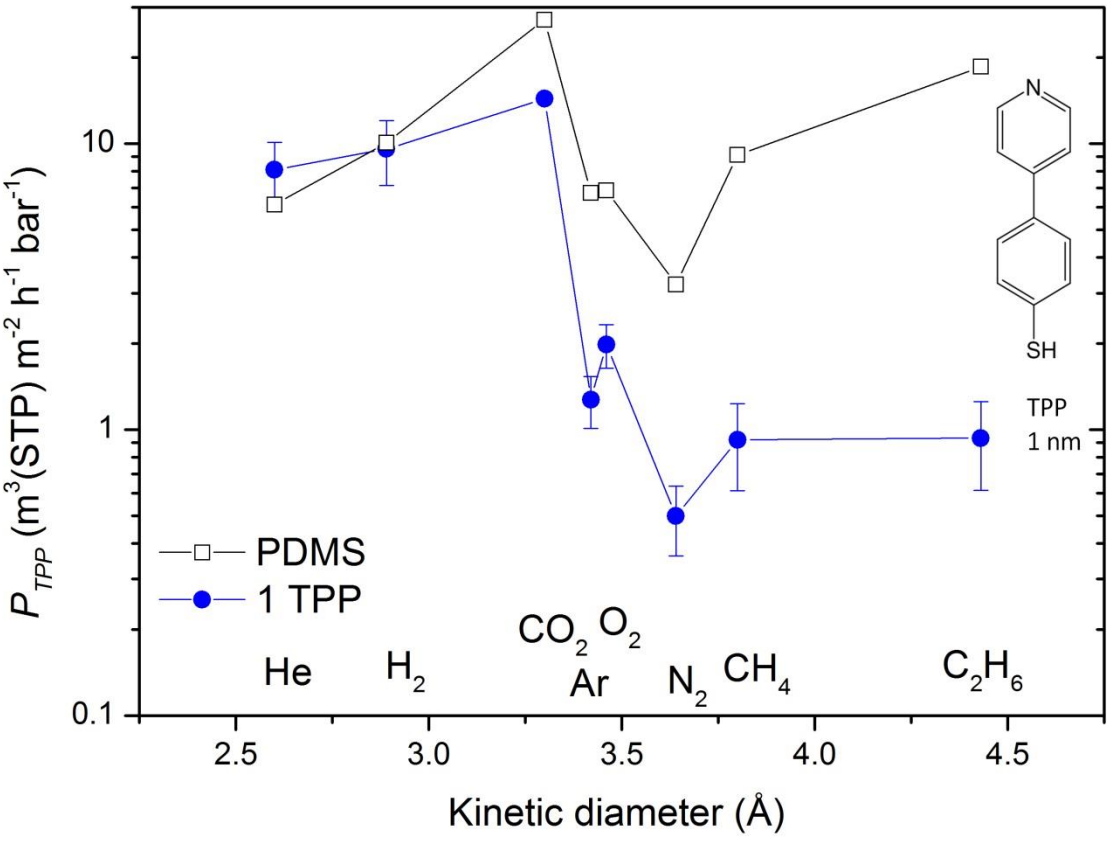

Fig.47 The intrinsic gas permeance P_{CNM} for a single-layer TPP-CNM in relation to the kinetic diameters of gases (He, H_2, CO_2, Ar, O_2, N_2, CH_4, C_2H_6).

The intrinsic gas permeance curve of TPP-CNM, depicted in Figure 47, exhibits high permeance for He, H_2 and CO_2 gases in comparison with the large gases (Ar, O_2, N_2, CH_4 and C_2H_6). Taking into consideration the increase in selectivity with smaller gases after the deposition of a single-layer TPP-CNM on a PDMS-TFC, and the high permeance of these gases (He, H_2 and CO_2), it can be said that TPP-CNMs show molecular sieving-like properties, as well.

If we compare the intrinsic gas permeance of the so far examined CNMs made from different precursors, we find that these CNMs show the same molecular sieving-like properties. The only difference among them being that the gas permeance of CNMs decreases when the thickness of single-layer CNMs is increased (Fig.48).

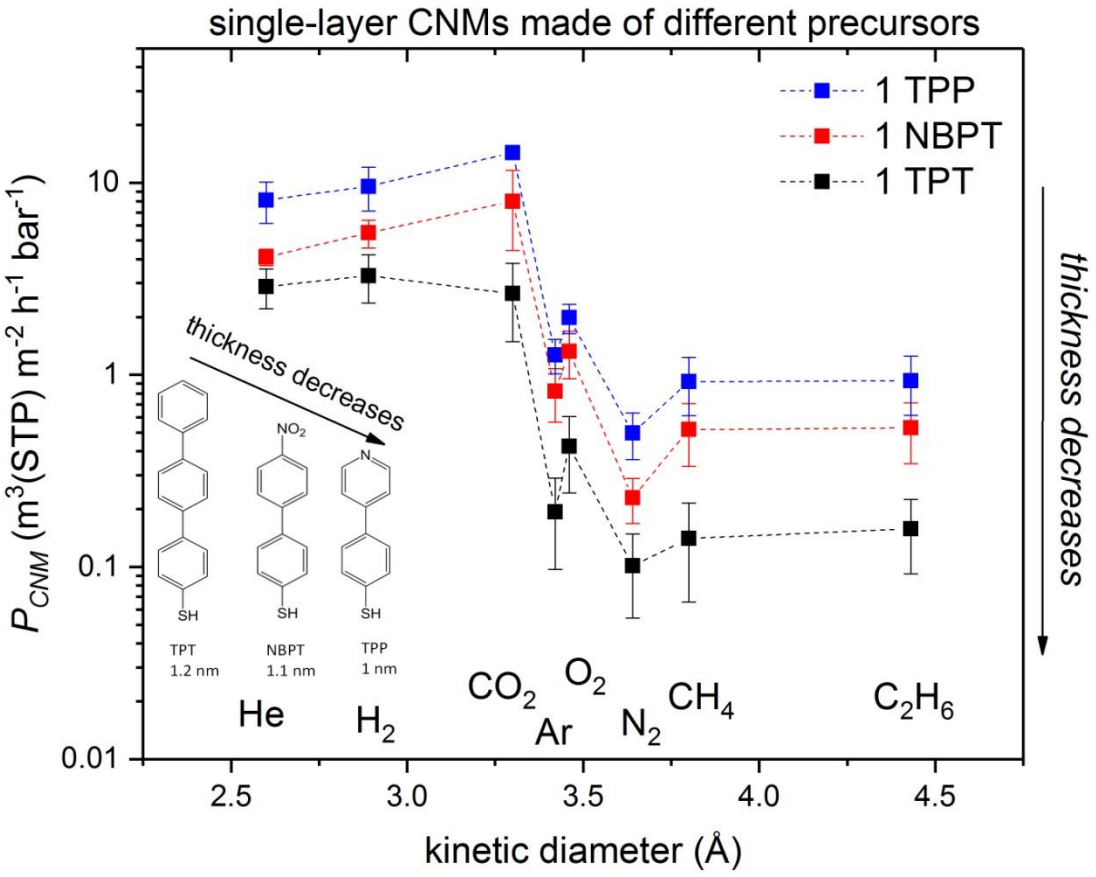

Fig.48 Comparison of the intrinsic gas permeance among single-layer TPT-, NBPT-, and TPP-CNMs.

5.5 Gas permeation of NPTH-CNMs

As was mentioned above, the freestanding CNMs with thicknesses between 0.6 and 1.7 nm were fabricated from SAMs of different polyaromatic precursors via low-energy electron-induced cross-linking [90]. It was reported that more densely-packed SAMs are formed from TPT and naphthalene-2-thiol (NPTH) precursor molecules. Additionally, the carbon densities of SAMs, which are the number of carbon atoms per unit volume, were estimated from the area per molecule and the thickness of the SAMs (Table 2). As can be seen from Table 2, the carbon density of NPTH-SAMs is higher than in the case of TPT-SAMs. Thus, it was assumed that the NPTH-SAM, with the highest carbon density and densely-packed structure, will form even smaller "openings," which, in turn, will likely improve gas selectivity.

The single- and double-layer NPTH-CNMs were fabricated and transferred onto PDMS-TFC supports and were sent to Helmholtz-Zentrum Geesthacht to test for single gas permeation with regard to the eight gases (He, H_2, CO_2, Ar, O_2, N_2, CH_4 and C_2H_6).

The measured gas permeance of single- and double-layer NPTH-CNMs on a PDMS-TFC are depicted in Figure 49. It shows that the decrease of gas permeance of the PDMS is very small after the deposition of single- and double-layer NPTH-CNMs on it. The decrease is $\sim 15\,\%$ after the deposition of the single-layer NPTH-CNM on the PDMS-TFC. While, in the case of the double-layer NPTH-CNM deposition onto the PDMS-TFC, the decreases of gas permeance is $\sim 30\%$. This is relatively higher in comparison with the single-layer, but it is still very small (Fig.49).

The slight decrease of gas permeance can be explained due to the thickness of the NPTH-CNM, which is 0.6 nm. The NPTH-CNM is the thinnest CNM examined in this work (Fig.40). Therefore, it can be assumed that the reason for the slight decrease is due to the many defects on NPTH-CNMs that appear during the transfer process. Taking into consideration the probability of having less defects in the case of multi-layer NPTH-CNMs, it was proposed to fabricate a stack of three-layer of NPTH-CNMs, and to test for gas permeation. Thereby, the two copies of triple-layer NPTH-CNMs were fabricated and transferred onto PDMS-TFCs. The measured gas permeance of triple-layer NPTH-CNMs on a PDMS-TFC showed more than $\sim 60\,\%$ and $\sim 80\,\%$ reduction of gas permeance in

comparison with a bare PDMS-TFC for each copy of the triple-layer CNMs, respectively. The measured gas permeance of triple-layer NPTH-CNMs on a PDMS-TFC is depicted in Figure 49. It shows that in the case of the three-layer, defects are fewer and the decrease of gas permeance of the PDMS-TFC is explicit after the deposition of three-layer NPTH-CNMs, although, the shape of the gas permeance curve looks similar to that of the bare PDMS (Fig.49).

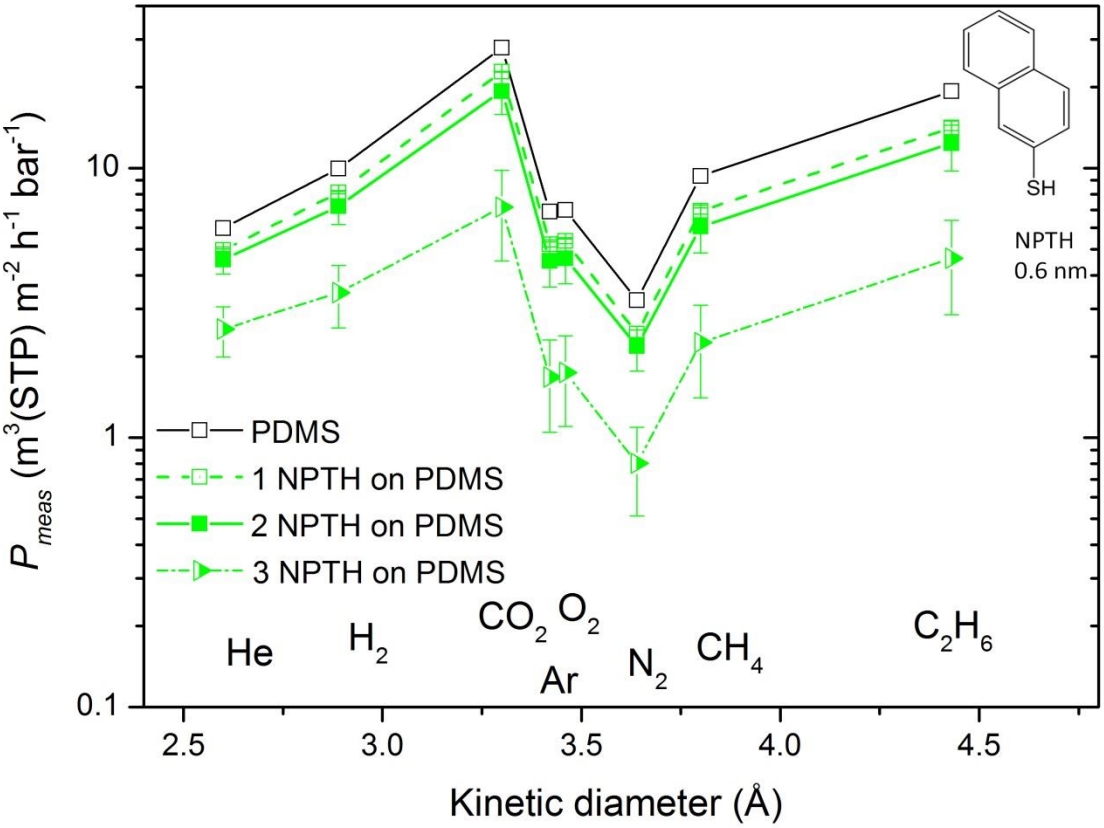

Fig.49 Measured gas permeance of single-, double- and triple-layer NPTH-CNMs on a PDMS support in relation to the kinetic diameters of gases (He, H_2, CO_2, Ar, O_2, N_2, CH_4, C_2H_6).

However, the intrinsic properties of NTPH-CNM are more interesting. These properties can be found by applying the resistance model to the measured permeance values of three-layer NPTH-CNMs on a PDM-TFC. (Fig.50).

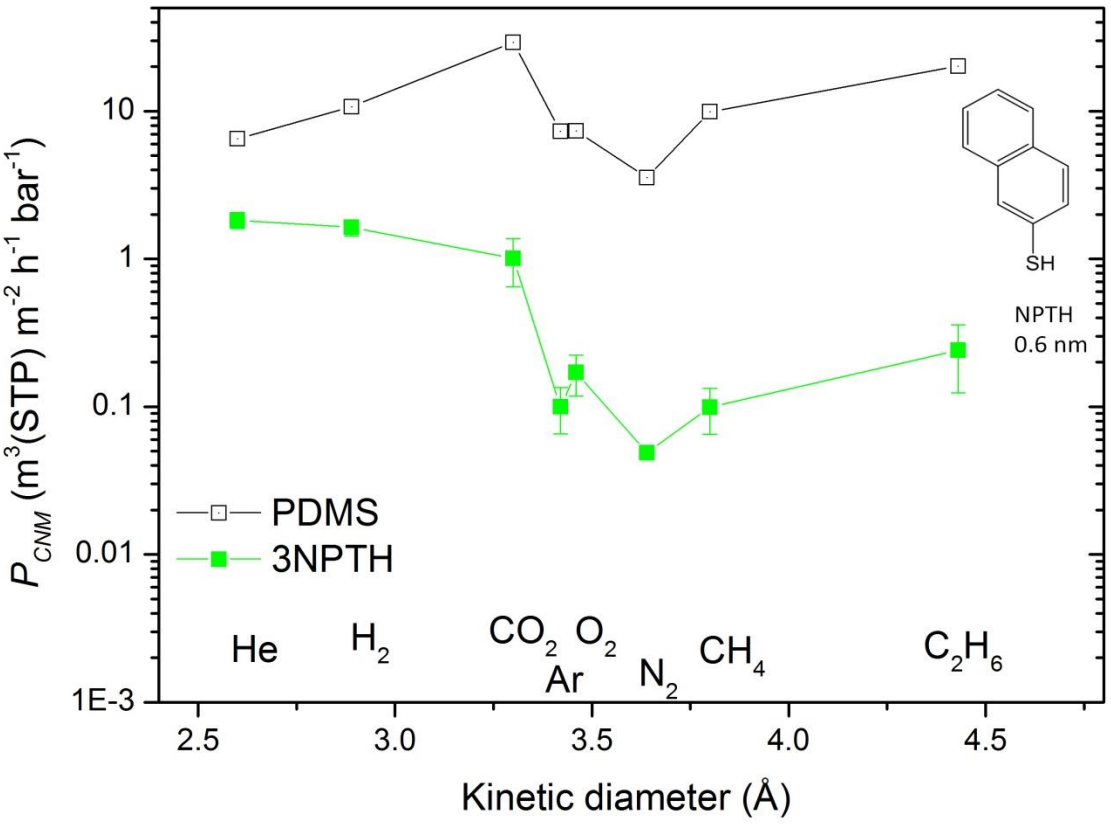

Fig.50 Intrinsic gas permeance P_{CNM} for triple-layer of NPTH-CNMs in relation to the kinetic diameters of gases (He, H_2, CO_2, Ar, O_2, N_2, CH_4, C_2H_6).

As can be seen in Figure 50, the intrinsic gas permeance of three-layer NPTH-CNMs reveals more than one order of magnitude higher values for the gases with the smallest kinetic diameters (He and H_2) in comparison with the gases with the larger kinetic diameters (Ar, O_2, N_2, CH_4 and C_2H_6). An exception is intrinsic the gas permeance of CO_2 gas, which is less than the permeance of He and H_2, but, higher compared with the rest of the gases. The three-layer NPTH-CNM performs as the other multi-layer CNMs made of different precursors. This behavior shows that it is more likely that lateral diffusion is involved between the layers, which can also explain the decrease of CO_2 gas permeance.

When comparing the intrinsic gas permeance of three-layer CNMs made from different precursors, it becomes apparent that the intrinsic gas permeance decreases when the thickness of CNMs is increased by varying the precursor molecules (Fig.51). The same behavior was observed in the case of single-layer CNMs (Fig.48).

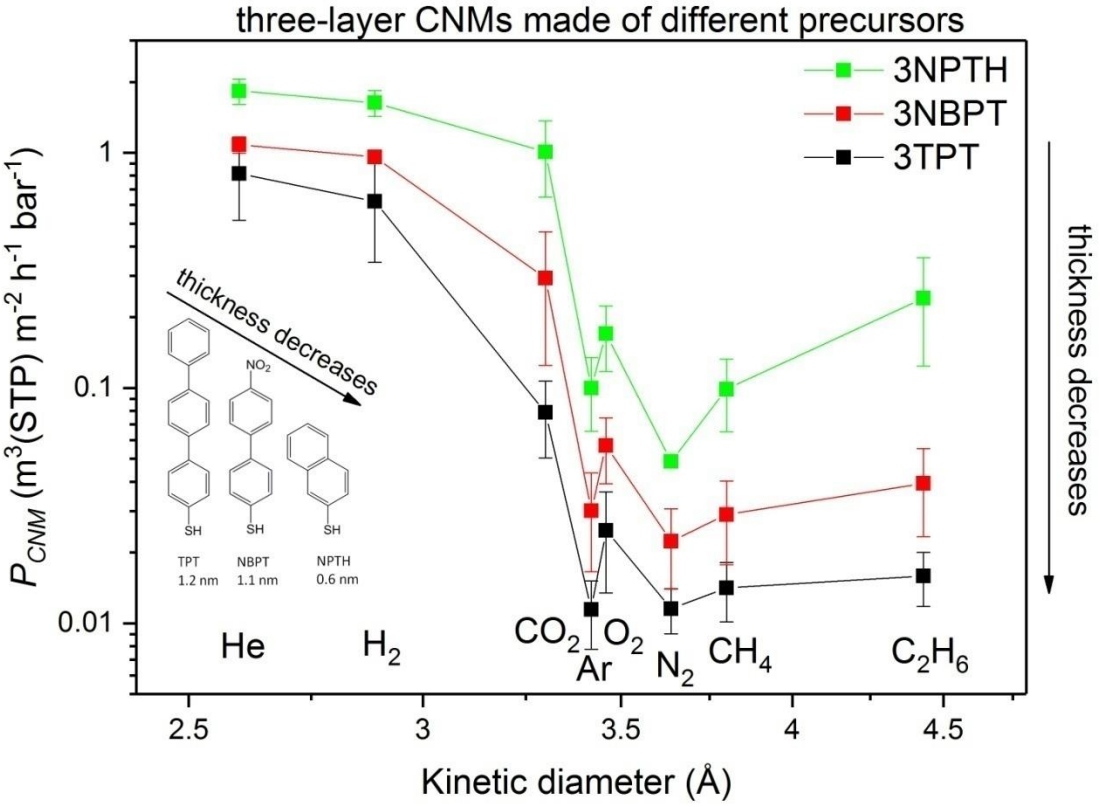

Fig.51 Comparison of intrinsic gas permeances among triple-layer NPTH-, NBPT-, and TPT-CNMs.

To sum up the gas permeation results of CNMs yield that all single-layer CNMs, made from different precursor molecules, show the same gas permeation characteristics, which are molecular sieving-like properties. In addition, the results obtained for single-layer CNMs show no evidence of Knudsen diffusion. For multi-layer CNMs, it is concluded that lateral diffusion can be involved among the CNMs, which can be described by Knudsen-like diffusion or by condensation and surface flow. The findings also reveal that intrinsic gas permeance of multilayer CNMs decreases with increasing the thickness of CNMs. This behavior is observed in both cases of CNMs, in particular single- and multi-layer ones.

Chapter 6

Gas permeation of multilayer CNMs with varying number of layers

6.1 Gas permeation of multilayer CNMs with varying number of layers

As shown in Chapter 5, a lateral diffusion mechanism may be involved in between the CNMs, in the case of multilayer CNMs. It is justified by the need of horizontal transport for gases in between the CNMs after passing through the proposed vertical molecular-sized channels, as it is less likely that these channels and defects are found at the exact same location on different CNMs (Fig.52). The origin of these "openings" or "channels" might be interpreted by the cross-linking process due to its statistical nature, which results in a random variation of intermolecular distances.

In order to investigate and understand the mechanism of gas permeation of multi-layer CNMs, single-, double-, triple-, and four-layer NBPT-CNMs were fabricated and transferred onto a PDMS-TFC.

Initially, a multilayer CNM is mechanically stacked and then transferred onto a PDMS-TFC support. Then single gas permeation measurements were conducted with multilayer NBPT-CNMs with regard to the eight gases (He, H_2, CO_2, Ar, O_2, N_2, CH_4, C_2H_6).

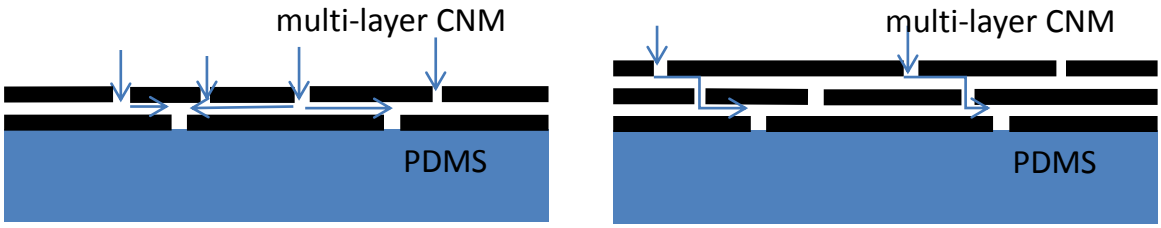

Fig.52 Schematic representation of proposed mechanism of gas permeation through multilayer CNMs. It indicates that lateral diffusion may additionally be involved.

The measured gas permeances of multilayer NBPT-CNMs on a PDMS-TFC are depicted in Figure 53. When considering the reduction of gas permeance of a bare PDMS-TFC after the successful deposition of multilayer NBPT-CNMs, from a single-layer to a four-layer NBPT-CNMs, the largest and most significant drop occurs between single- and double-layer NBPT-CNMs (Fig.53).

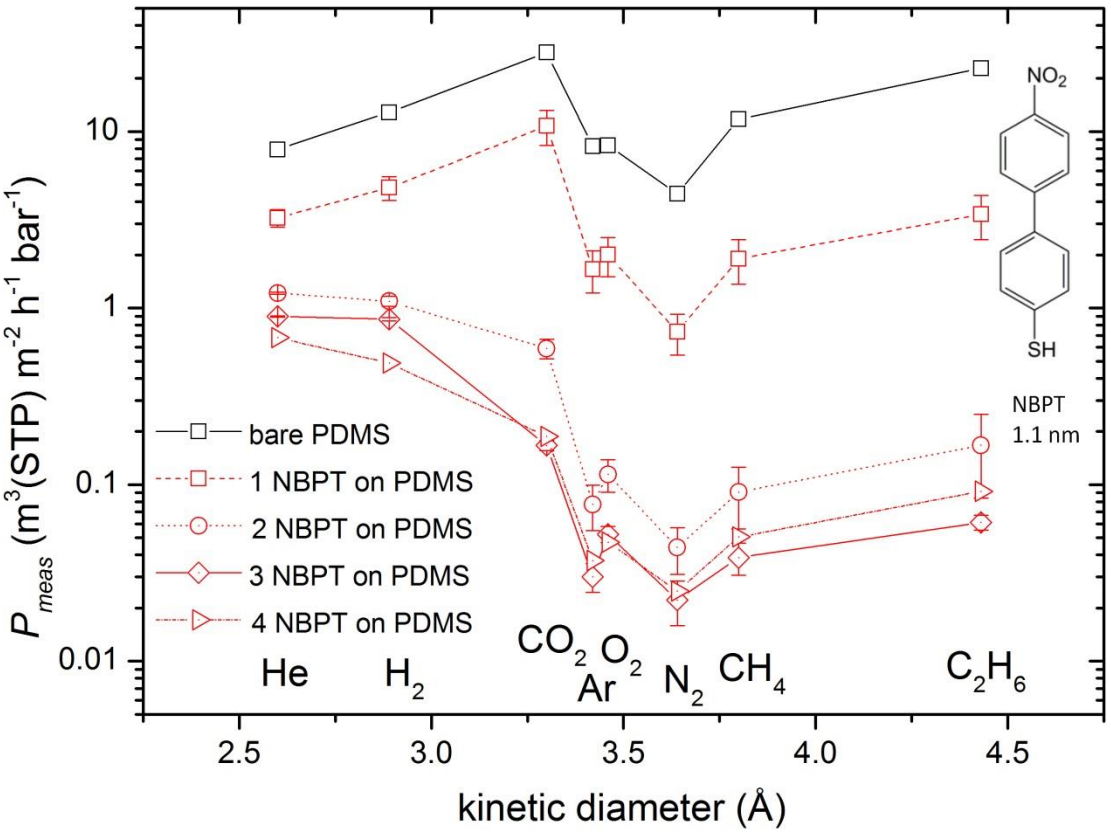

Fig.53 The measured gas permeance of multilayer NBPT-CNMs with a varying number of layers.

The tendency of the reduction of gas permeance becomes explicit when plotting the relative permeance of multilayer NBPT-CNMs, which is the ratio of the measured gas permeance of multilayer NBPT-CNM-PDMS-TFCs to the corresponding permeance of the reference PDMS-TFC (Fig.54). As can be seen from Figure 54, the reduction of gas permeance between the single- and double-layer NBPT-CNMs is significantly higher than the reduction between the other three NBPT-CNMs. Nevertheless, when comparing the ratio between the single- and double-layer NBPT-CNMs on a PDMS-TFC, the values vary in the range of 2 to 4 for the smallest gases (He and H_2), and for the rest of the gases (CO_2, Ar, O_2, N_2, CH_4 and C_2H_6), the ratios vary in the range of 16 to 21. In the case of the other multilayers, the ratio of the gas permeance is comparably smaller. The values between double-/triple-layer and triple-/four-layer NBPT-CNMs vary in the range of 1.5 to 3. The ratio is the smallest in the case of triple/four-layer CNMs.

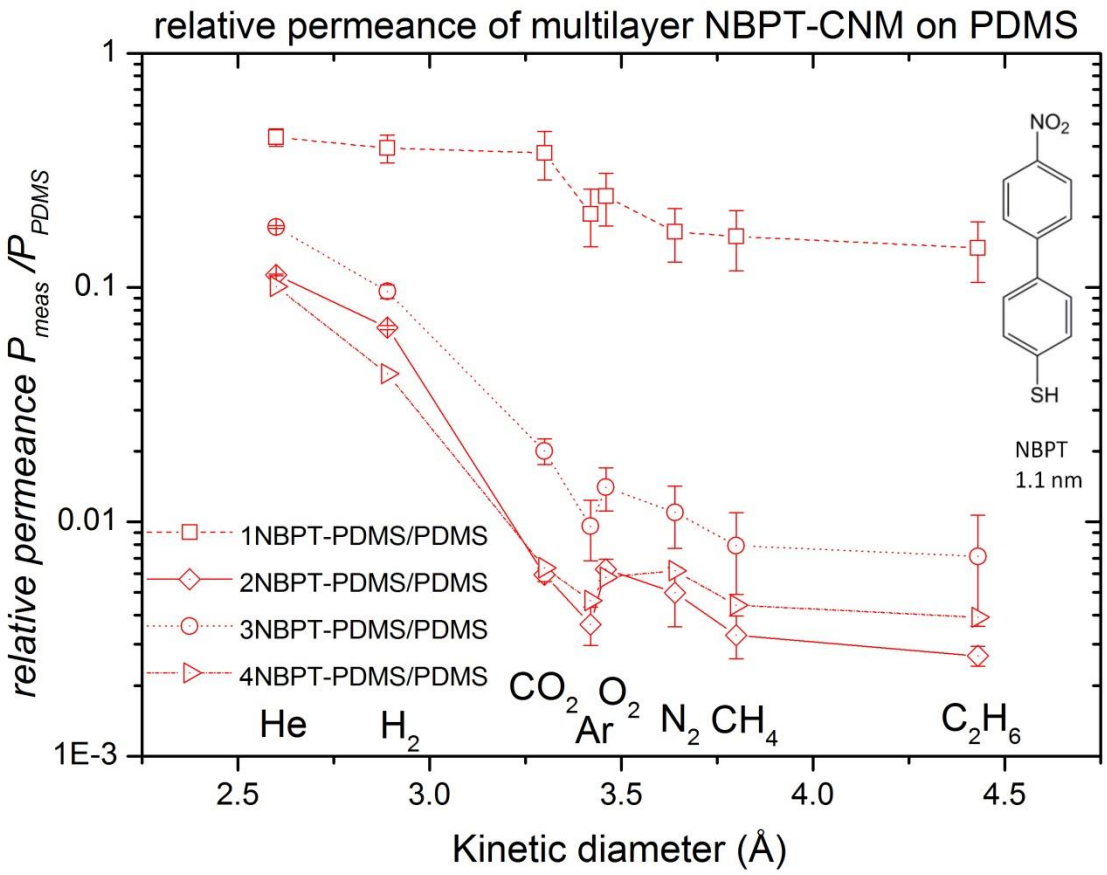

Fig.54 Relative gas permeance of multilayer NBPT-CNMs on a PDMS-TFC, which is ratio of the measured permeance values to the corresponding permeance of the reference PDMS-TFC.

Taking into consideration the significant drop of gas permeance for all gases, and in particular, the big drop of CO_2 gas permeance during the transition from single- to double-layer CNMs, the probability of the emergence of an additional new mechanism of gas permeation in between the CNMs becomes apparent. This finding, again, supports the idea that lateral diffusion in between the CNMs may be involved, as proposed in Chapter 5. Moreover, when assuming that there is only vertical gas transport in between the CNMs in the case of multilayer ones, then the drop of gas permeance would have been proportional to the number of layers in a multilayer. Nevertheless, that is not the case. The obtained results are consistent with the assumption that lateral diffusion in between the CNMs can be described by Knudsen-like diffusion or by condensation and surface flow of gas molecules, as it was proposed in Chapter 5.

In order to obtain a clear picture of the intrinsic gas permeance of multilayer CNMs, the "resistance model" was applied to the measured gas permeance values. The intrinsic gas permeance of the multilayer NBPT-CNMs is depicted in Figure 55.

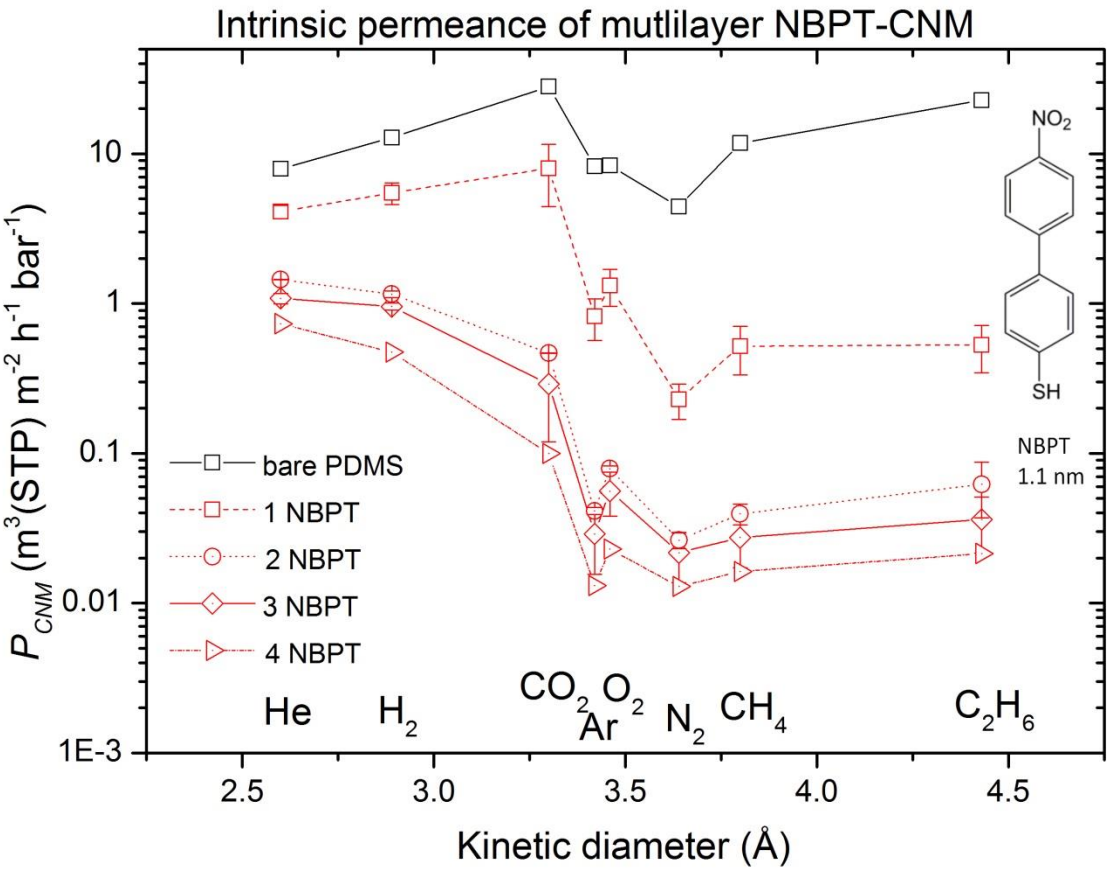

Fig.55 The intrinsic gas permeance of multilayer NBPT-CNMs with a varying number of layers.

As can be seen in Figure 55, the drop of intrinsic gas permeance of multilayer NBPT-CNMs is the biggest in between the single- and double-layer CNMs. The drop of gas permeance varies in the range of 2.7 to 4.8 for the two gases with the smallest kinetic diameters, He and H_2, and for the rest of the gases (CO_2, Ar, O_2, N_2, CH_4 and C_2H_6), the drop varies in the range of 9 to 26. The drop between double-/triple-layer and triple-/four-layer NBPT-CNMs varies in the range of 1.5 to 2.2. This finding again reaffirms the assumption of lateral diffusion in between the CNMs. In particular, when plotting the intrinsic gas permeance of multilayers in relation to the number of layers, the big drop of

permeance during transition from single-layer to double-layer NBPT-CNMs can be noticed (Fig.56).

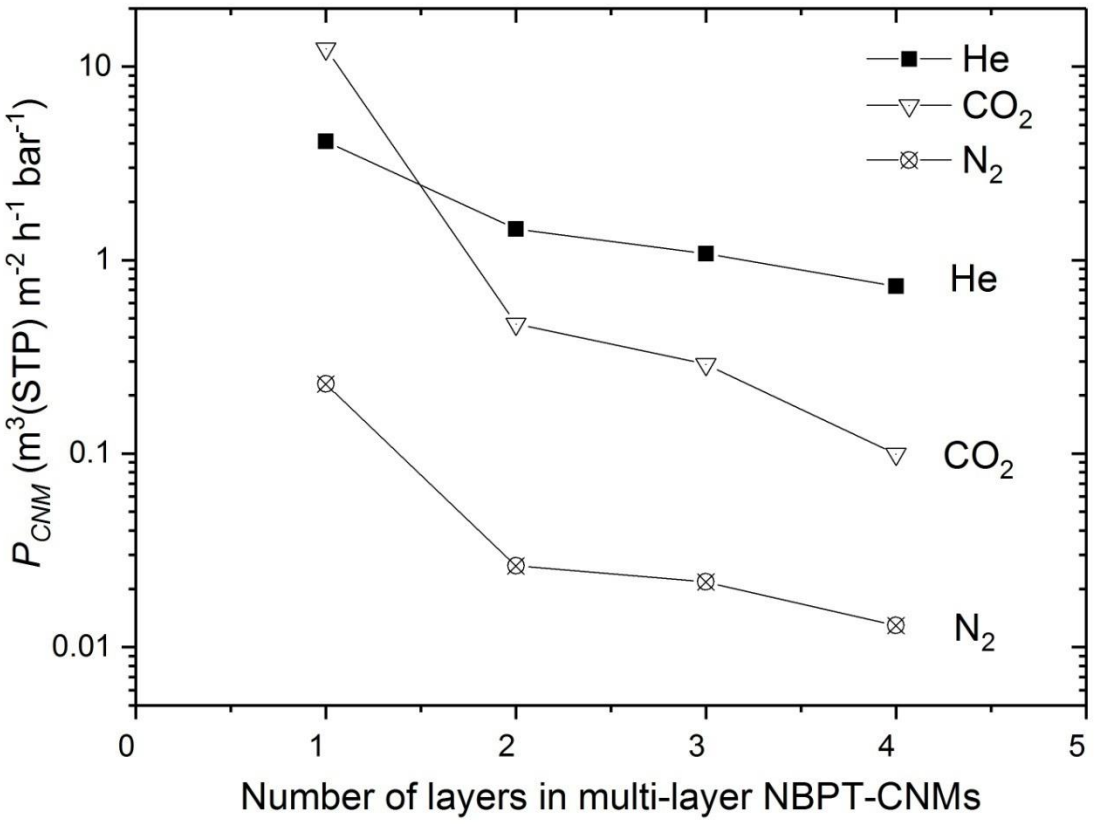

Fig.56 The intrinsic gas permeance of a multi-layer NBPT-CNM in relation to the number of layers.

In Figure 56 the permeance is depicted in a logarithmic scale. Moreover, the drop of gas permeance between single- and double-layer NBPT-CNMs becomes more apparent when plotting gas permeance in a linear scale (Fig.57). In addition, one can notice that gas permance is linearly decreasing, beginning with the double-layer NBPT-CNMs. The linear dependence is clearly observed when plotting gas permeance starting with the double-layer NBPT-CNM (Fig.58).

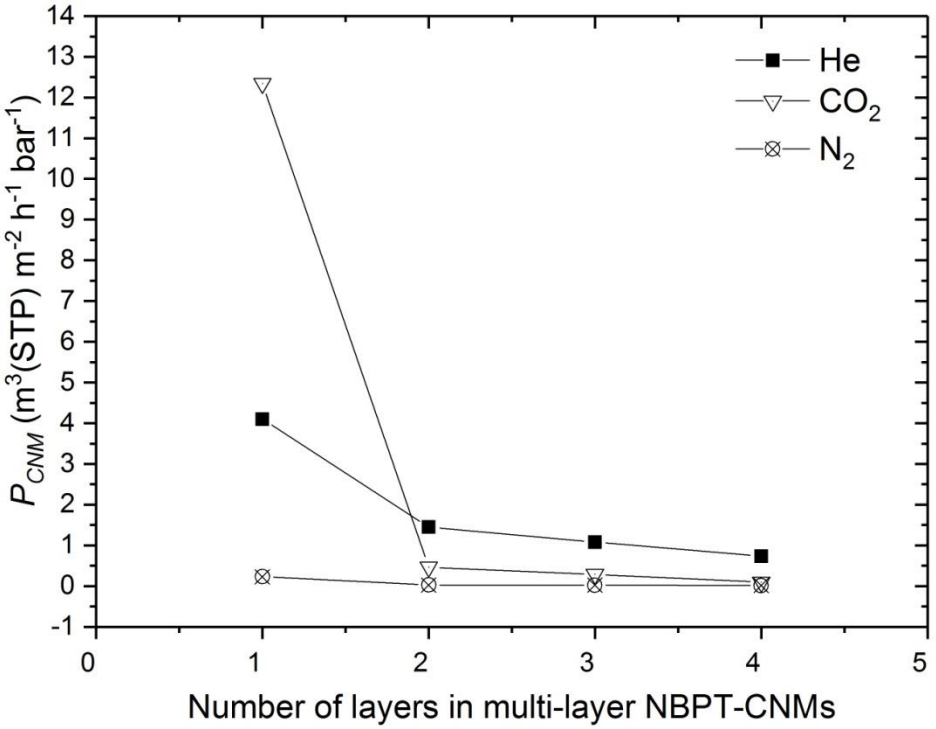

Fig.57 The intrinsic gas permeance of a multi-layer NBPT-CNM in relation to the number of layers.

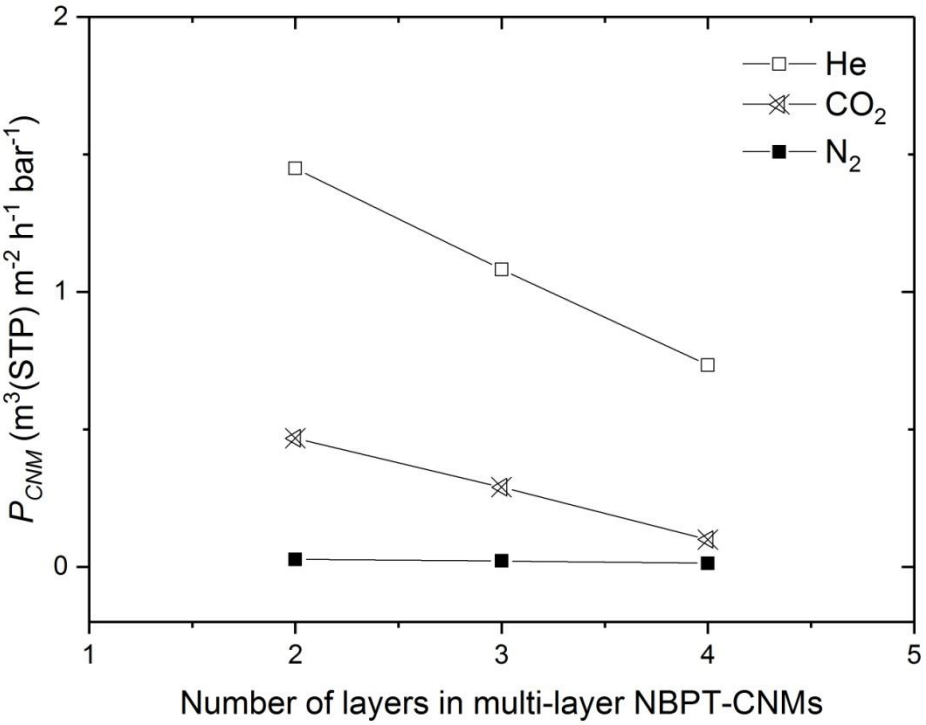

Fig.58 The intrinsic gas permeance of a multilayer NBPT-CNM in relation to the number of layers, starting with a double-layer NBPT-CNM.

The result depicted in Figure 58 reveals the linear dependence of gas permeance of multilayer NBPT-CNMs in relation to the number of layers. This can be interpreted as follows: the mechanism of gas permeation in between the CNMs in multilayers is the same, which definitely differs from the mechanism that exists in the case of a single-layer CNM. It has been observed that a single-layer CNM, made from different precursor molecules, shows molecular sieving-like properties upon gas permeation through the CNMs. Therefore, in the case of multilayer CNMs, gases initially require a vertical transport mechanism through the first layer of a CNM. Thereafter, there should be a different mechanism of gas transport, which is horizontal transport. Otherwise, there would be a linear dependence starting from the single-layer NBPT-CNM. Nevertheless, the big drop of CO_2 gas permeance in the case of multilayer CNMs in comparison with the single-layer CNM, and the big decrease of gas permeance for all gases, lead to the assumption the occurrence of lateral diffusion in between CNMs. This indicates the need for horizontal transport of gases in between the CNMs, which can be explained by Knudsen-like diffusion. As He and H_2 are easily condensable gases, in contrast to CO_2, Ar, O_2 and N_2, lateral diffusion can also be described by condensation and surface flow. The need for lateral diffusion has been described and proposed in other works, particularly in the work of graphene derivatives and its applications [107]. In another work, it has been proposed that metal permeates horizontally through GO interlayers due to defects and/or edges [108].

Chapter 7

Gas permeation of porous CNMs made from “mixed” SAMs

7.1 Introduction to the fabrication of pores in CNMs

Another promising approach to improving the characteristics of gas separation through CNMs, is the formation of molecular-sized pores in CNMs. The concept of fabrication of pores in CNMs is based on the exchange of molecules of a SAM with another type of precursor molecule. Several studies have been reported around this. For instance, as it was shown in Chapter 2, molecules of an NBPT-SAM can be exchanged with BPT molecules in the non-cross-linked regions, and from the subsequent exposure to the electron irradiation, a fully cross-linked patterned CNM is formed [95]. Other examples include, the insertion of aromatic molecules into the monolayer of an alkanethiolate or the asphaltene adsorption into a mixed SAM of aliphatic and aromatic trichlorosilanes [109, 110]. It has also been reported as a synthesis of a mixed SAM of alkanethiol molecules on gold [111]. All these abovementioned examples show the possibility of exchange of molecules after the formation of a SAM.

Previously, the electron irradiation of an alkanethiolate SAM was investigated. It resulted in the destruction of alkyl chains of the alkanethiol molecules (Fig.59). It was shown that low energy electron irradiation of a SAM of alkanethiolates resulted in the pronounced desorption of hydrogen and carbon containing fragments, the appearance of C-C/C=C crosslinks, the partial cleavage of Au-thiolate bonds, and the formation of a new sulfur species [87].

Taking into consideration these two arguments, it was planned to fabricate porous CNMs for gas separation experiments. The fabrication of the porous CNM is as follows: first, the SAM of NBPT will be prepared, and then it will be immersed into an octadecanethiol (ODT) solution in the ethanol, where the exchange of ODT molecules with some NBPT molecules will occur. Afterwards, the mixed SAM will be exposed to low-energy electron irradiation at a dose of 50 mC/cm^2. This dose of electron irradiation is sufficient for the complete cross-linking the NBPT-SAM and likely enough to detach or destroy alkyl chains of the ODT molecule. Eventually, after transferring the mixed SAM onto a preferable substrate, pores will be induced in the places of ODT molecules, as after electron exposure, alkyl chains are destroyed and remaining thiolate species will detach. The schematic representation of the fabrication of a porous CNM by a mixed SAM is depicted in Figure 60.

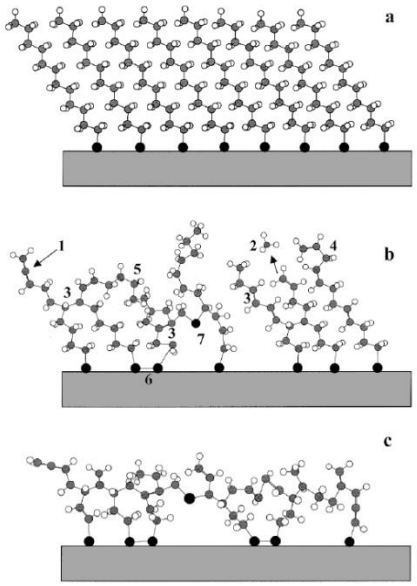

Fig.59 Schematic visualization of electron irradiation induced damage in an alkanethiolate film: (a), (b), and (c) represent the pristine and slightly/strongly irradiated films, respectively. Different irradiation induced defects are marked in (b): 1, cleavage of C-H bond; 2, cleavage of C-C bond and desorption of the cut fragment; 3, the appearance of C-C/C=C crosslinks; 4, a conformational defect; 5, chain reorientation; 6, formation of disulfide; 7, incorporation of sulfur in alkyl matrix [87].

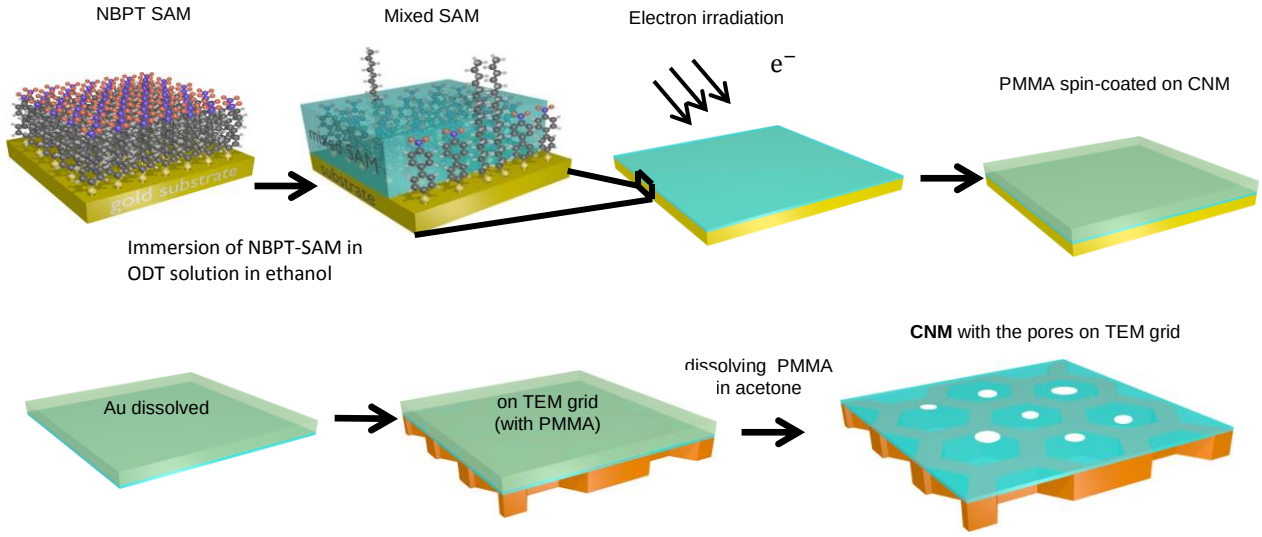

Fig.60 Schematic representation of the preparation of a porous CNM from mixed SAMs on the TEM grid.

7.2 Fabrication of a mixed SAM and control of exchange rate by an XPS

The exchange procedure of NBPT molecules with ODT molecules was controlled and characterized by an XPS and an HIM. Since the NBPT molecule consists of nitrogen in contrast to the ODT molecule, it is possible to control the exchange procedure due to the variation of the nitrogen peak intensity. The HIM helps to image and detect pores, and evaluate them. The first step was to check the possibility of exchange of the NBPT molecules with the ODT molecules. To do this, a 1mM high concentration of octadecanethiol solution in ethanol was prepared and samples of NBPT-SAMs were immersed into the solution for different time periods, which were as follows: 5-minute, 10-minute, 20-minute, and 30-minute. After immersion, the samples were rinsed with ethanol and stored under argon environment in petri-dishes for further XPS characterization. Subsequently, the XPS characterization was employed. It showed disappearance of the nitrogen peak beginning with 5-minute immersion time (Fig.61). This might be explained with the complete exchange of aromatic NBPT molecules with aliphatic ODT molecules in the NBPT-SAM. Moreover, the shift of the binding energy of carbon C1s peak from 284.5 eV to 285 eV, which corresponds to the aliphatic molecules, confirms the complete exchange of the molecules (Fig.62). In addition, the vanishing of O1s oxygen peak also reaffirms our conclusion (Fig.63).

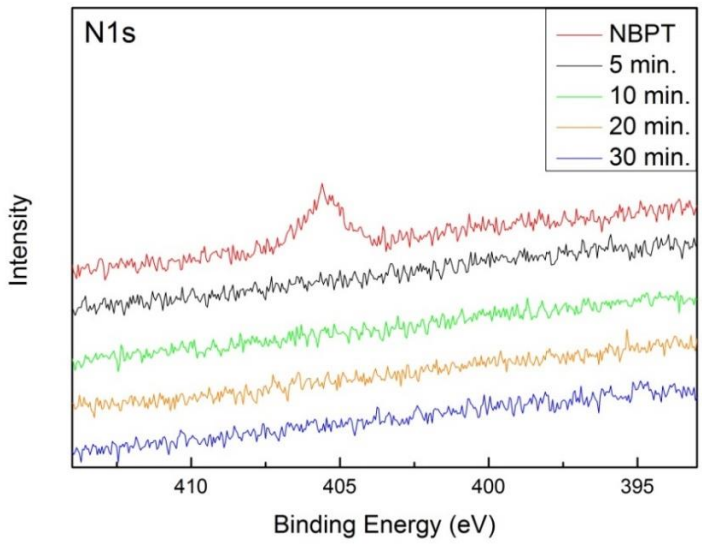

Fig.61 Disappearance of the nitrogen N1s signal after 5-minute immersion time indicates complete exchange of ODT molecules with NBPT molecules (1mM concentration of ODT in ethanol).

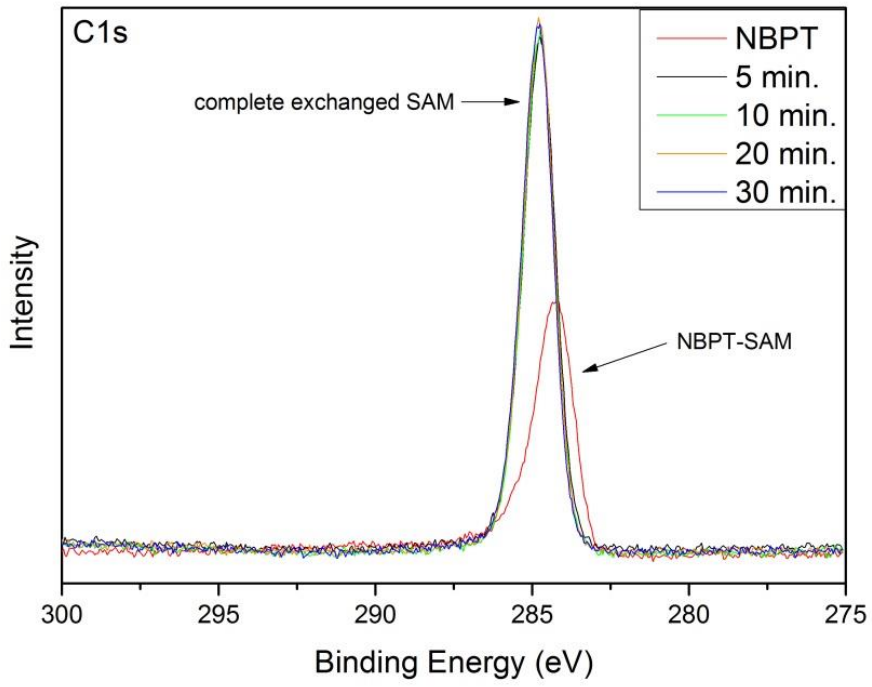

Fig.62 Shift of the binding energy of aromatic carbon C1s signal to the aliphatic carbon indicates complete exchange of ODT molecules with NBPT molecules (1mM concentration of ODT in ethanol).

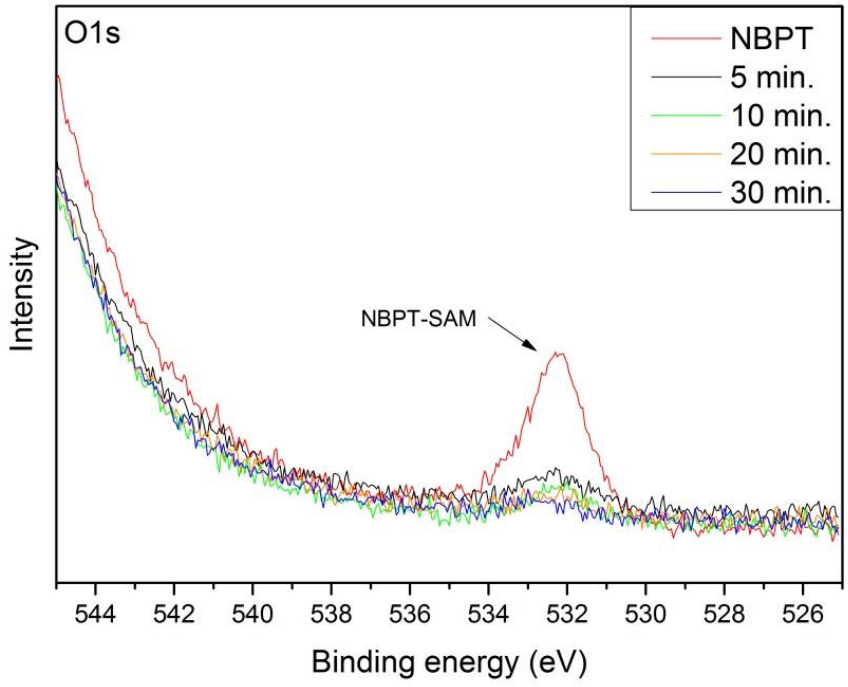

Fig.63 Complete disappearance of the oxygen O1s signal after 5-minute immersion time indicates complete exchange of ODT molecules with NBPT molecules (1mM concentration of ODT in ethanol).

7.3 Complete exchange time of NBPT molecules with ODT ones in NBPT-SAMs

The next step was to find the starting point of the exchange of molecules in order to fabricate a porous membrane and define the complete exchange time. To do this, the time of immersion (i.e. the exchange time) of the NBPT-SAM into 1mM concentration of ODT solution in ethanol would need to be decreased. Therefore, the immersion time was reduced from 5-minute to 1-minute, with 1 minute intervals. The XPS measurements showed almost complete disappearance of the N1s peak at 5-minute immersion time, which defines the complete exchange time (Fig.64). Additionally, it showed that starting from 1-minute immersion time there is already a big decline of the nitrogen peak, which indicates considerable exchange of the molecules. This was confirmed with the shift of the binding energy of the carbon C1s peak from the aromatic 284.2 eV value to the aliphatic 284.6 eV (Fig.65). The vanishing of the O1s peak reaffirms the same observation (Fig.66). The XPS showed that either concentration of ODT is still high enough to obtain small exchange or time immersion needs to be reduced.

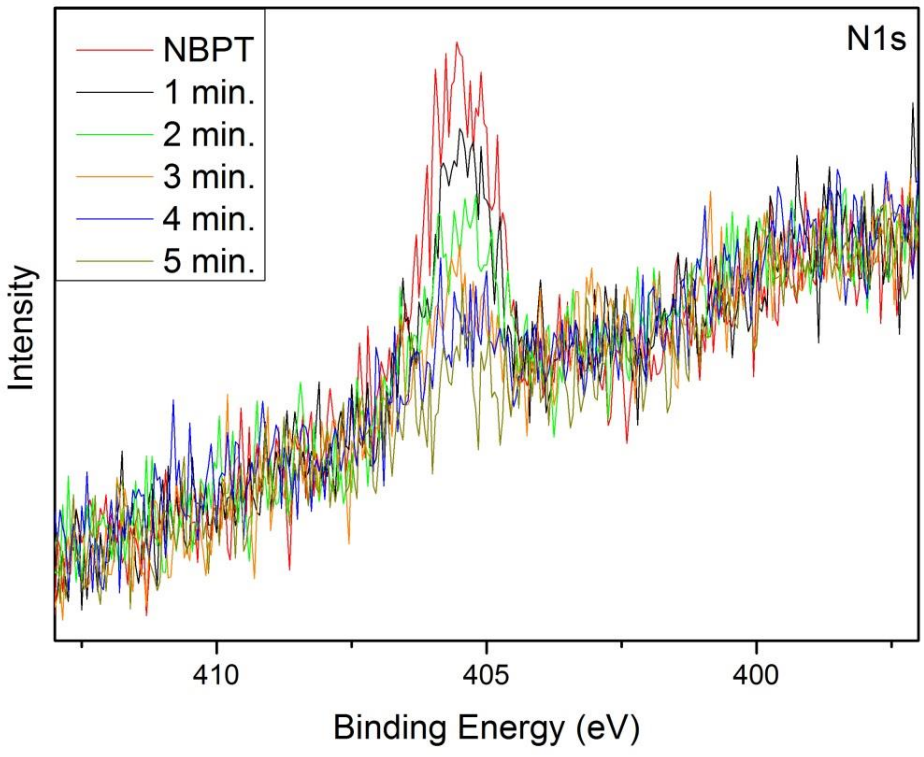

Fig.64 Disappearance of the nitrogen N1s signal after 5-minute immersion time indicates complete exchange of ODT molecules with NBPT molecules (1mM concentration of ODT in ethanol).

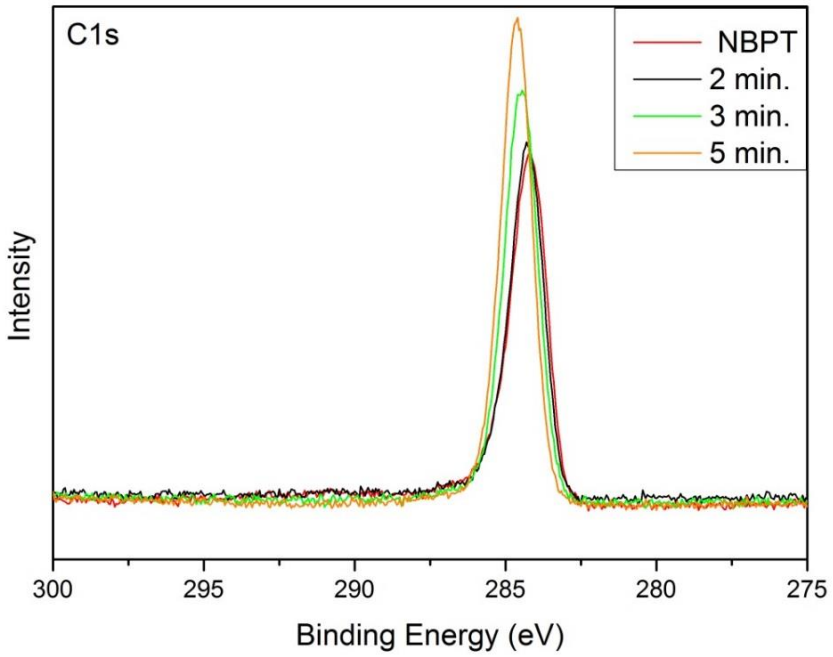

Fig.65 Gradual shift of the binding energy of carbon C1s signal to higher values with increasing immersion time corresponds to the exchange of aromatic molecules with aliphatic ones (1mM concentration of ODT in ethanol).

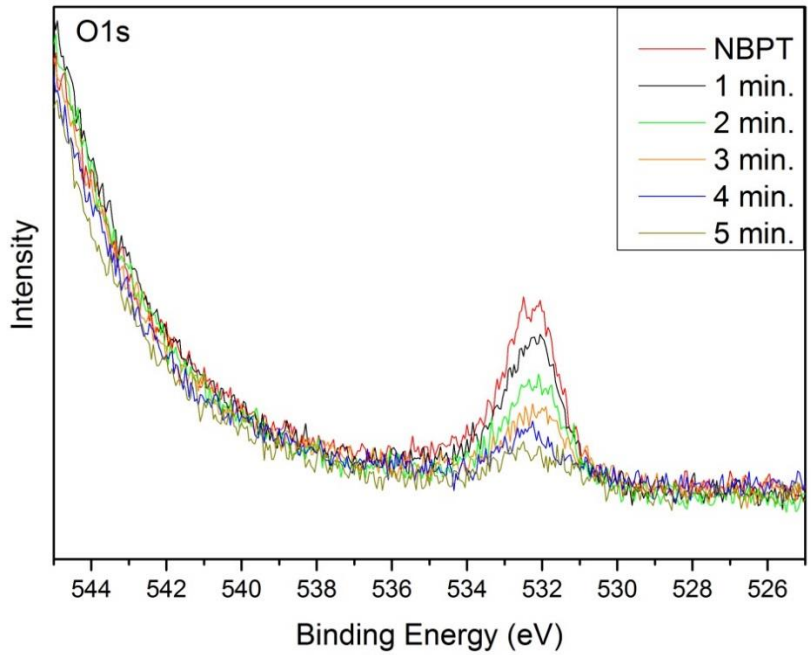

Fig.66 Gradual decrease of intensity in the oxygen O1s signal, indicating that 5-minute immersion time is enough for the complete exchange of ODT molecules with NBPT molecules (1mM concentration of ODT in ethanol).

7.4 Freestanding porous CNMs

The XPS observation mentioned above shows that 1-minute immersion time is sufficient for considerable exchange of the molecules in the NBPT-SAM. Hence, to induce small, molecular-sized pores in the CNM, the time immersion needs to be reduced. Taking into consideration this fact, the immersion time was again reduced in the following sequence: 1-minute, 30-second, and 15-second in 1 mM concentration of ODT solution in ethanol. The XPS spectrum of N1s showed almost no decline in intensity, which corresponds to a small exchange of the molecules (Fig.67).

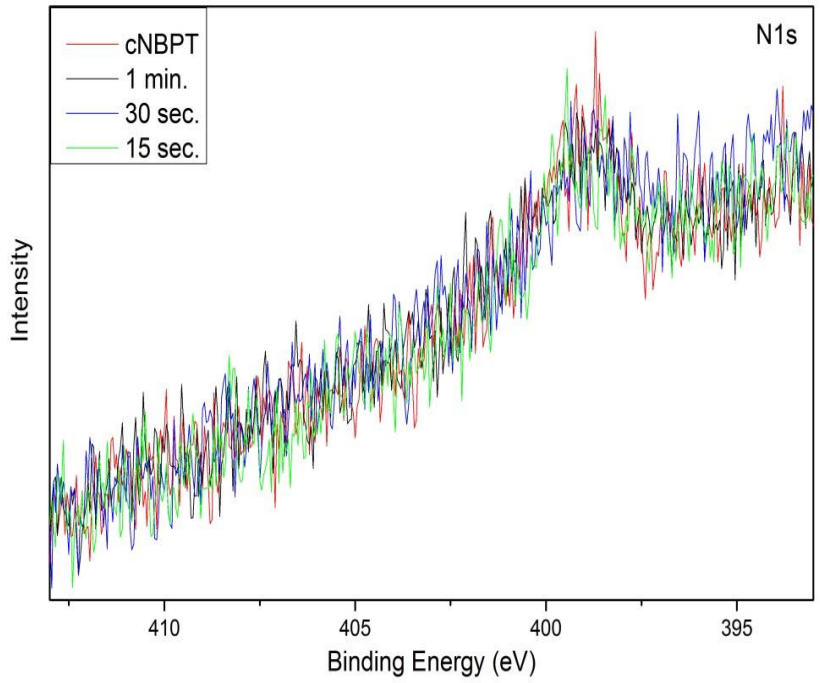

Fig.67 XPS spectrum of the N1s signal is depicted (after cross-linking), indicating almost no exchange of the molecules from few seconds to 1-minute immersion time (1mM concentration of ODT in ethanol).

The mixed SAMs, presented in Figure 67, were irradiated for $50 mC/cm^2$, and then transferred onto TEM grids to be examined by an HIM for coverage and pores. The images, depicted in Figure 68, show TEM grids covered with CNMs made of mixed SAMs. Based on these images, one can conclude that TEM grids are well covered in all cases, which indicates the possibility of fabrication of intact freestanding CNMs from mixed SAMs.

a)

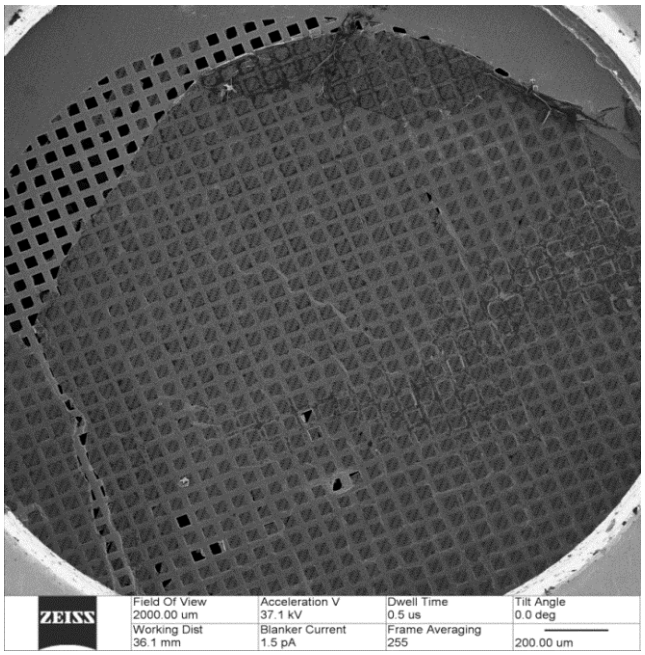

b)

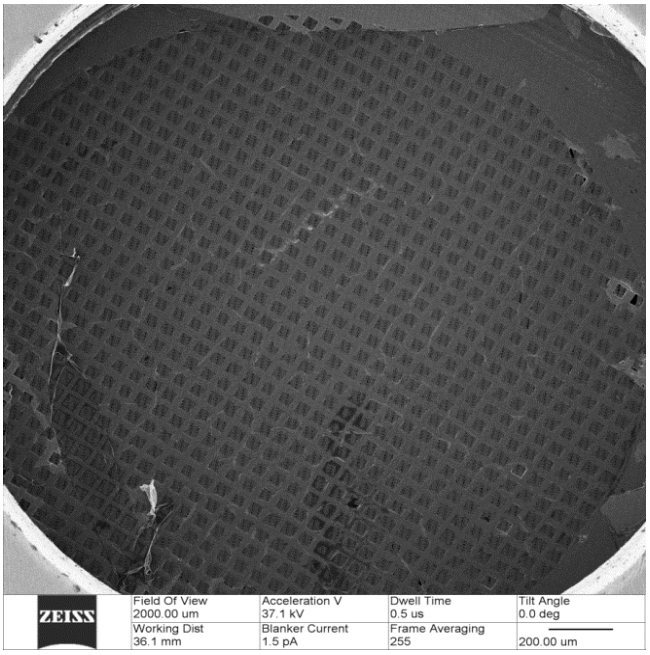

c)

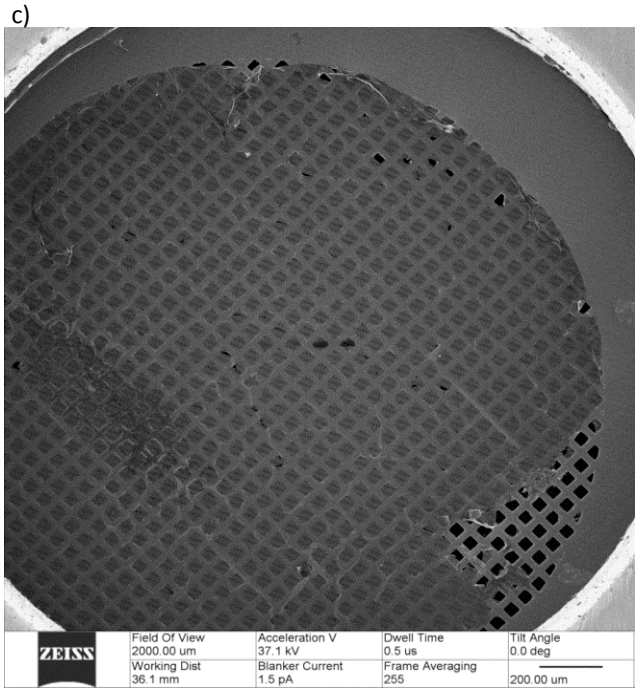

d)

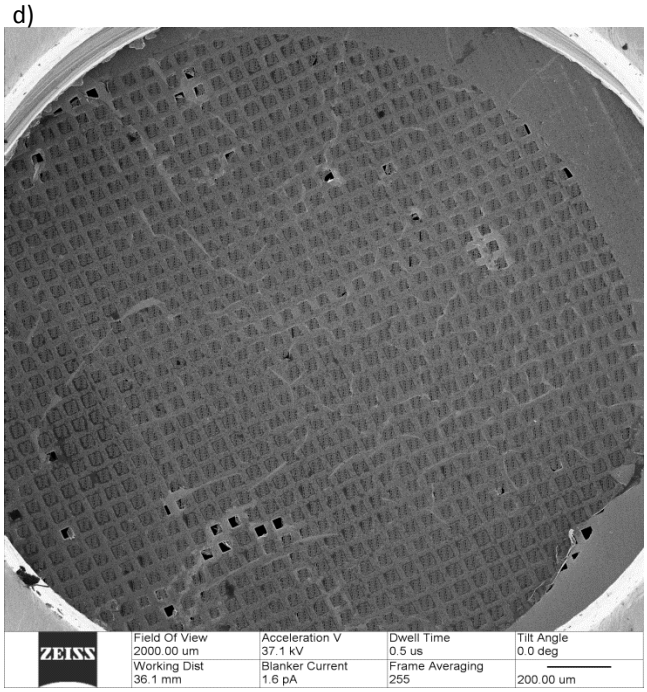

Fig.68 HIM images of CNMs made from mixed SAMs, and then exposed to electron irradiation of $50 mC/cm^2$ dose and transferred onto TEM grids. Mixed SAMs were prepared via immersion of an NBPT-SAM into 1 mM ODT solution in ethanol for the following periods of time: a) 15-second, b) 30-second, c) 1-minute, and d) 2-minute.

Furthermore, detailed investigation revealed nm-sized pores in the CNMs made of mixed SAMs (Fig.69). The evaluation of the pore sizes was done for porous CNMs immersed for 15-second, 30-second, and 1-minute, respectively, in a 1 mM ODT solution (Fig.69).

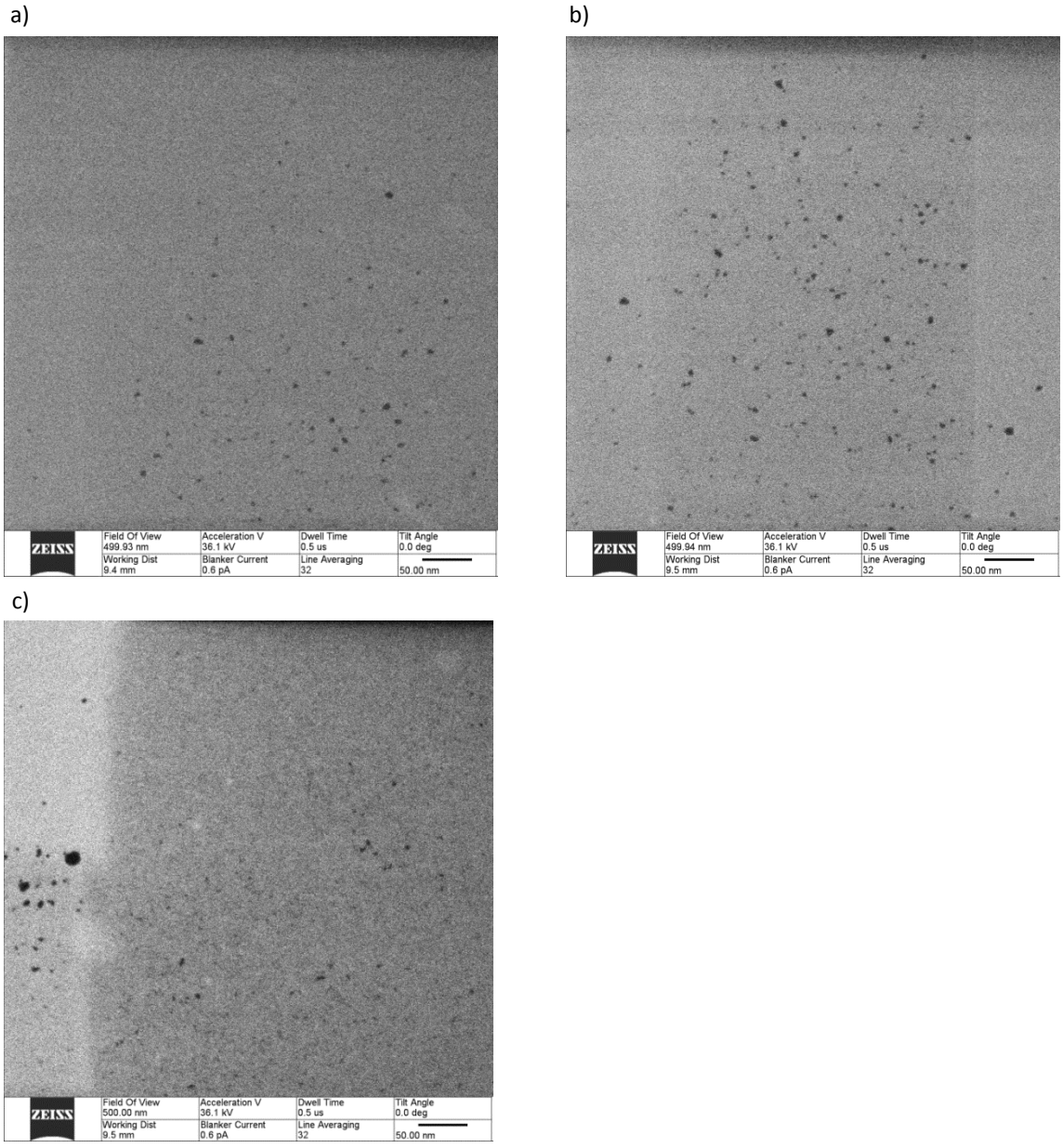

Fig.69 HIM zoomed images of CNMs immersed into 1 mM ODT solution for a) 15-second, b) 30-second, and c) 1-minute.

A Gwyddion program was implemented to evaluate the pore sizes. The pores in the images were magnified, marked, and subsequently analyzed regarding their area distribution with automatic particle analysis. The mean diameter was then deducted

assuming a circular shape for each imaged pore. From the images shown in Fig.70, Fig.71, and Fig.72, it can be seen that the maximum pore size is slightly increased when immersion time increases from 15-second to 1-minute. The aforementioned conclusion is based on the evaluation of areas that were randomly selected and imaged by an HIM for each case of immersion time.

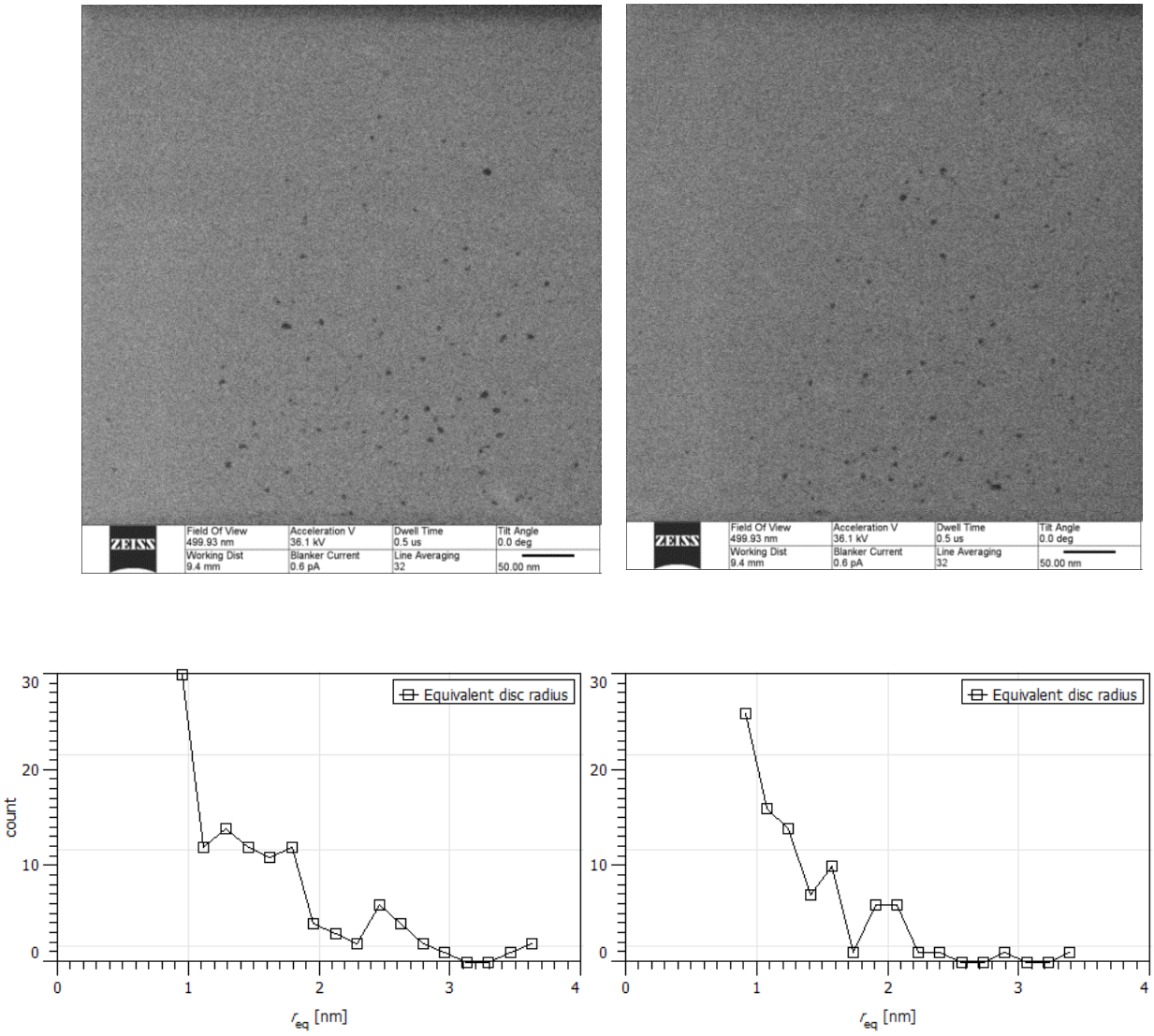

Fig.70 Distribution of the pores in the case of 15-second immersion time. Depicted areas were randomly selected.

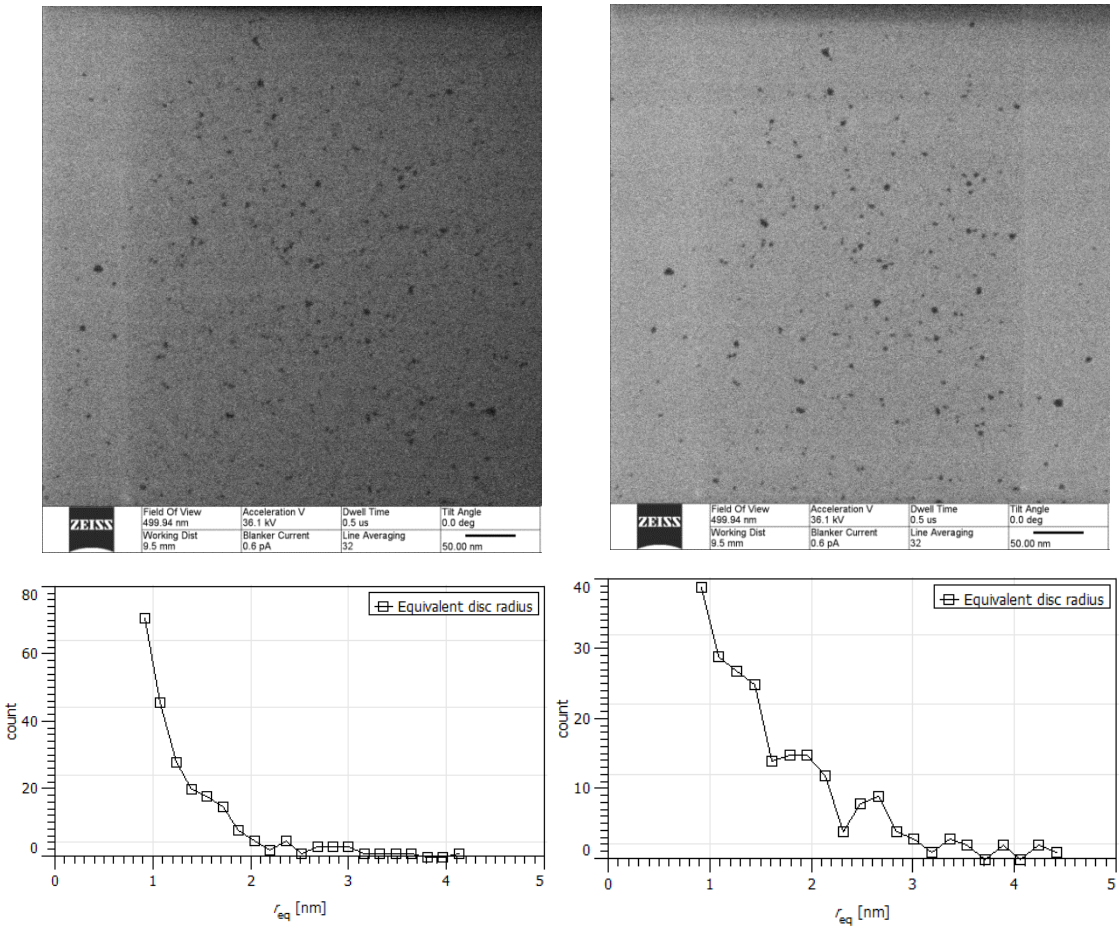

Fig.71 Distribution of the pores in the case of 30-second immersion time. Depicted areas were randomly selected.

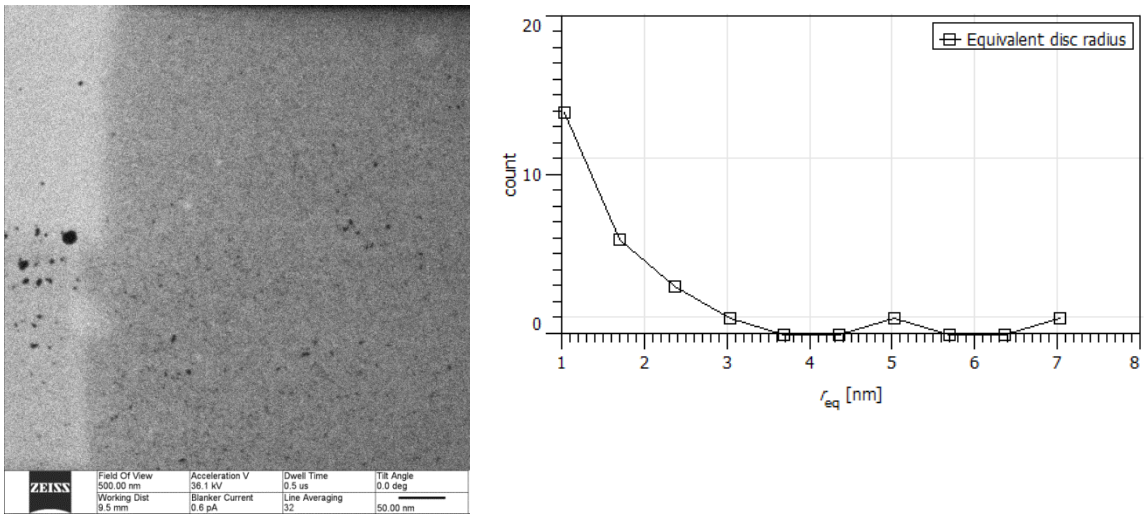

Fig.72 Distribution of the pores in the case of 1-minute immersion time. Depicted area is randomly selected.

The summary of pore size distribution is presented in Table 5. It is important to consider that the smallest pore, which was possible to detect, had approximately 2nm diameter.

Immersion time	Minimum diameter	Maximum diameter
CNM – 15-second	~ 2nm	~ 7.4 nm
CNM – 30-second	~ 2nm	~ 8.8 nm
CNM – 1-minute	~ 2nm	~ 14 nm

Table 5 Distribution of the pores based on the differences of the immersion time.

7.5 Decrease of the concentration of ODT solution down to 1 µM for smaller pores

Since the ultimate goal is to induce molecular-sized pores in CNMs for membrane gas separation, the pores need to be smaller than were obtained above. Thus, the concentration of ODT molecules in ethanol solution was reduced down to micromoles in order to mitigate the exchange of NBPT molecules with ODT molecules. It was assumed that the reduction of the concentration of ODT in ethanol solution may reduce the exchange rate of molecules, and hence the number of molecules in the exchange, which would result in smaller pores. Therefore, the concentration of ODT molecules in ethanol solution was reduced from 1 millimoles to 6.7 micromoles. The exchange of molecules was again examined by an XPS. The mixed SAMs were fabricated by immersing NBPT-SAMs into 6.76 µM ODT solution in ethanol for different time periods, and subsequently observed with an XPS. The XPS spectrum of N1s signal showed gradual decrease of intensity, which corresponded to the exchange of NBPT molecules with ODT molecules (Fig.73). The exchange of molecules was observed in the O1s and C1s spectrums (Fig.74 and Fig.75). In the case of the C1s signal, the shift of the binding energy to higher values, which corresponds to aliphatic molecules, reaffirms the exchange of the molecules. The decrease of the oxygen intensity also confirms the successful exchange of aromatic NBPT molecules with aliphatic ODT molecules. Since 10- to 30-minute immersion times showed small exchanges of the molecules, mixed SAMs were irradiated and then transferred onto the TEM grids to be examined for pores (Fig.76).

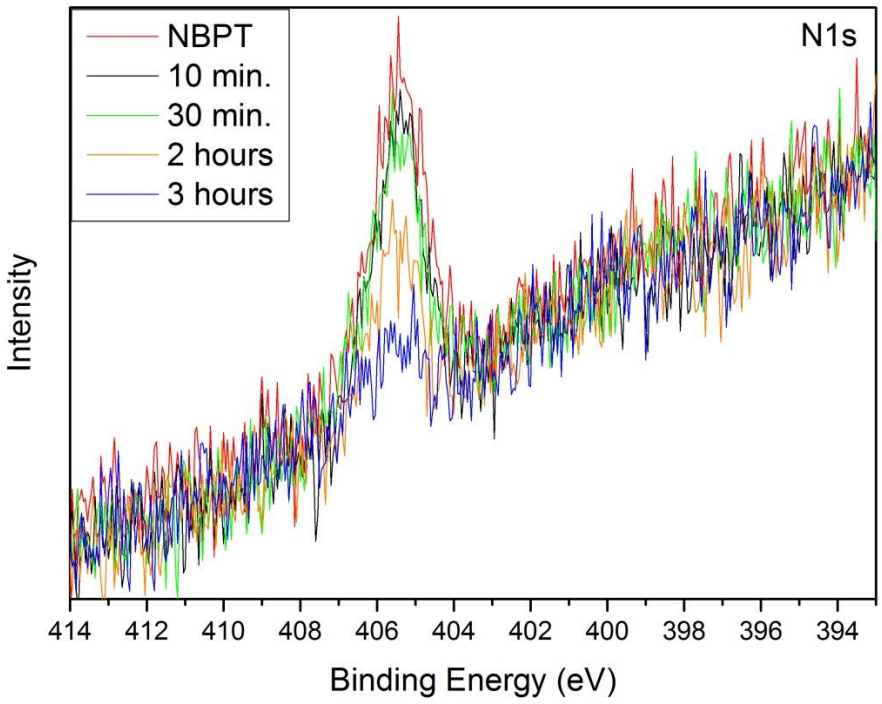

Fig.73 XPS spectrum of the N1 signal shows decrease of intensity when exchange time increases from 10-minute to 3-hour (6.76 µM concentration of ODT in ethanol).

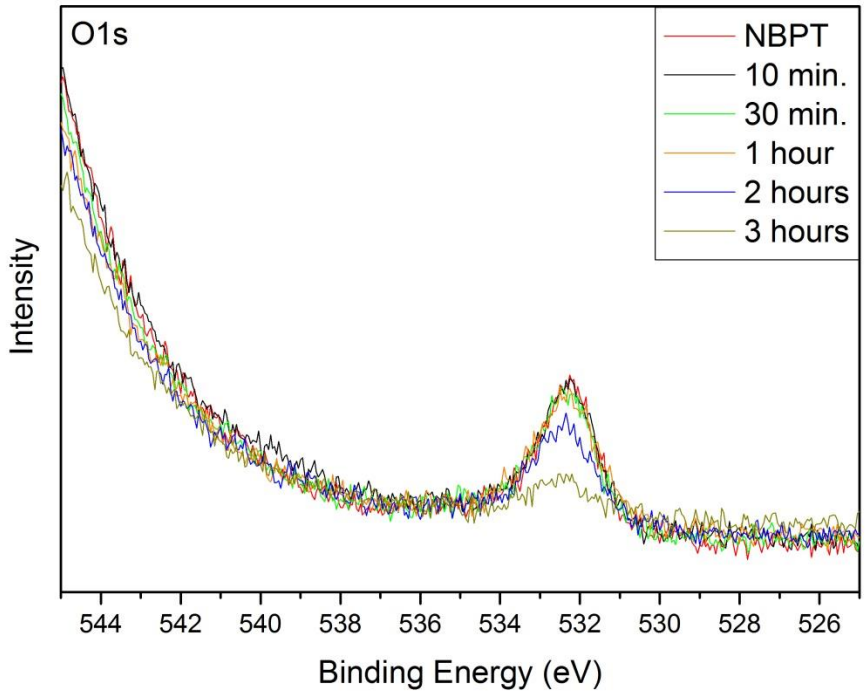

Fig.74 XPS spectrum of the O1s signal. Gradual decrease of the signal of oxygen from 10-minutes to 3-hour confirms the exchange of molecules (6.76 µM concentration of ODT in ethanol).

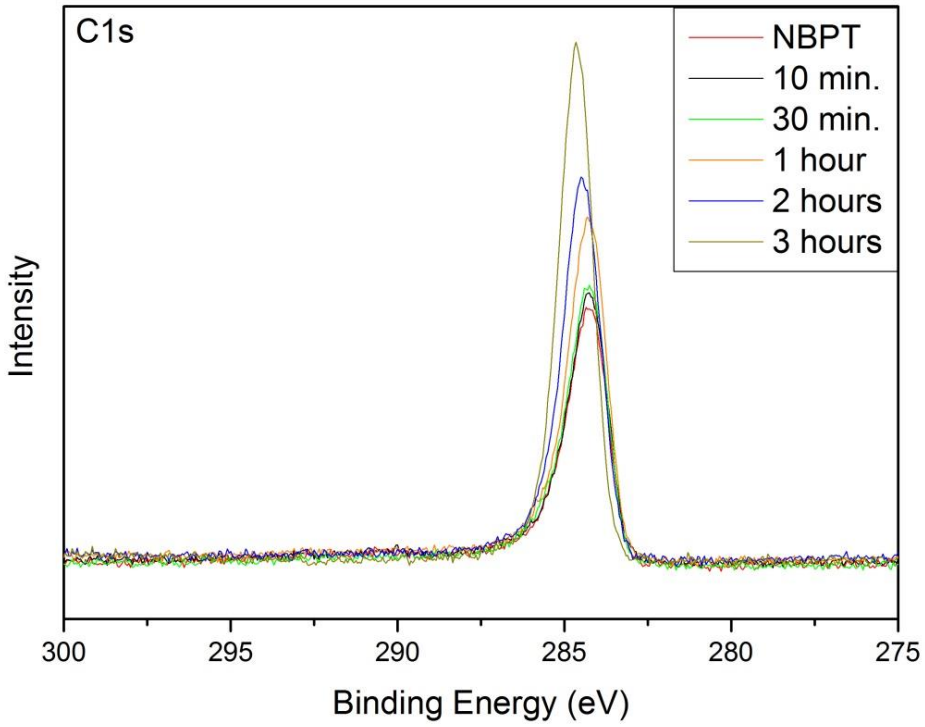

Fig.75 XPS spectrum of the C1s signal. Gradual shift to higher binding energy from 10-minute to 3-hour shows the exchange of molecules from aromatic to aliphatic ones (6.76 µM concentration of ODT in ethanol).

The HIM observation showed an increase of pore sizes when immersion time was increased from 10-minute to 30-minute. The images presented in Figure 76 confirm this hypothesis.

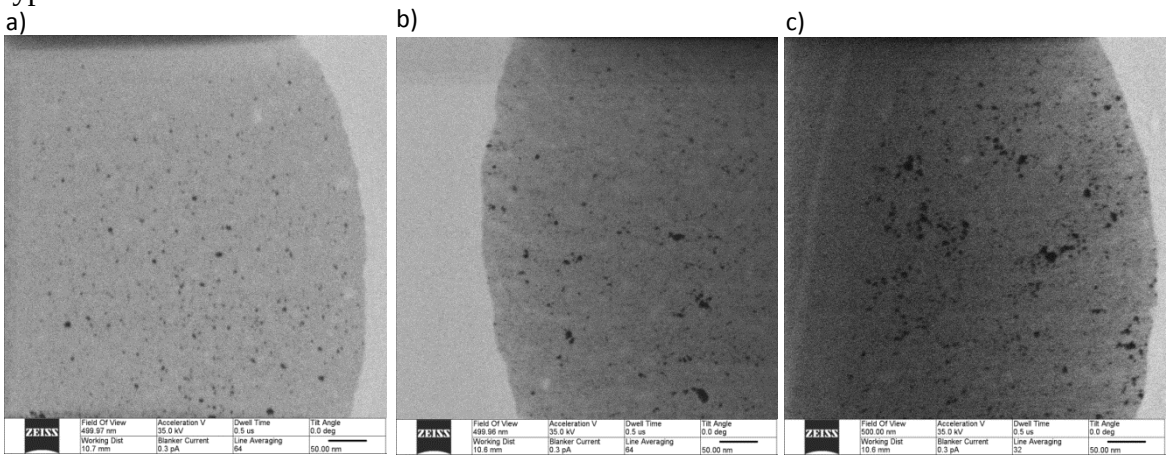

Fig.76 HIM images of porous CNMs made of mixed SAMs. Images are from samples made at 6.76 µM concentration of ODT in ethanol for immersion times of a) 10-minute, b) 20-minute, and c) 30-minute.

7.6 Detection of the smallest exchange, and hence the smallest pores

The results presented in Figure 76, once again, indicate the possibility of fabrication of pores in CNMs by exchanging the aromatic molecules of SAMs with aliphatic ones, although, the pores presented in the images are large enough for the separation of small gases with diameters up to 5 angstroms. Therefore, to form smaller pores in CNMs, the exchange rate of the molecules need to be reduced, again. Hence, the ODT concentration was further reduced to 1.76 µM. The exchange time periods, which correspond to the immersion time of NBPT-SAMs in the ODT solution in ethanol, were also reduced from 20-minute to 3-minute. This was done to obtain smaller pores. The XPS spectrum of the N1s signal showed no change of intensity from 3- to 20-minute exchange time (Fig.77). The same result was obtained in the case of C1s and O1s spectrums (Fig.78).

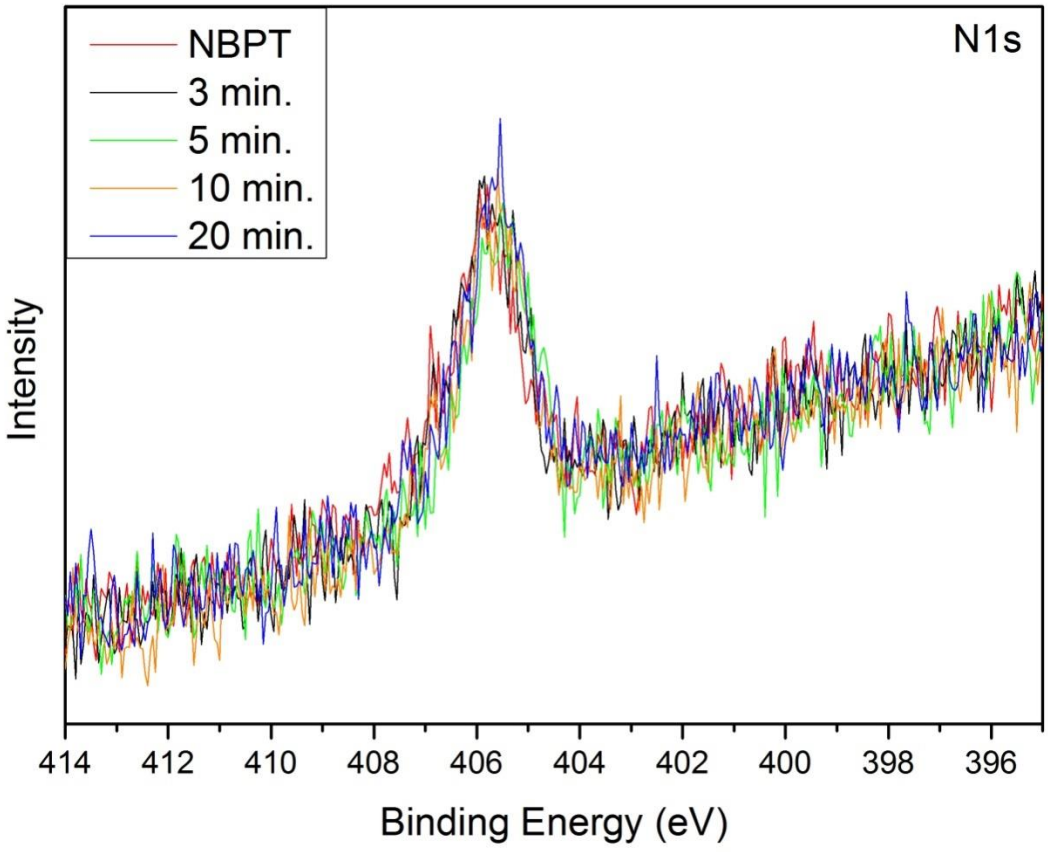

Fig.77 XPS spectrum of the N1 signal shows no change of intensity when the exchange time is increased from 3- to 20-minute (1.76 µM concentration of ODT in ethanol).

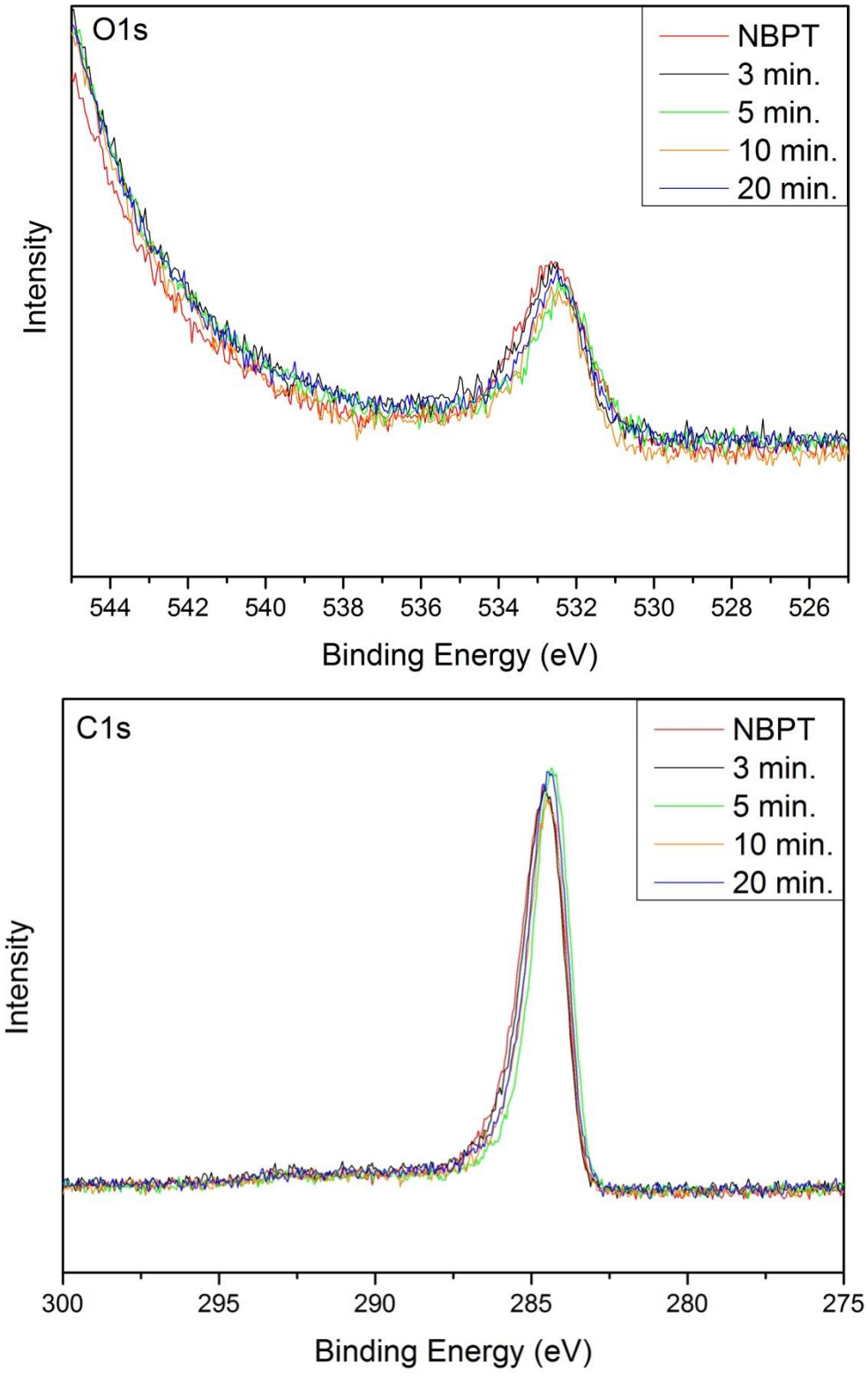

Fig.78 XPS spectrums of O1s (upper) and C1s (lower) signals show no change of intensity when the exchange time is increased from 3- to 20-minute (1.76 μM concentration of ODT in ethanol).

Since 20-minute of immersion of the NBPT-SAM into 1.76 µM concentration of ODT solution did not detect any exchange of molecules, an HIM observation was employed to explore for pores. The HIM observation indicated no pores for the sample with 3-minute exchange time (Fig.79).

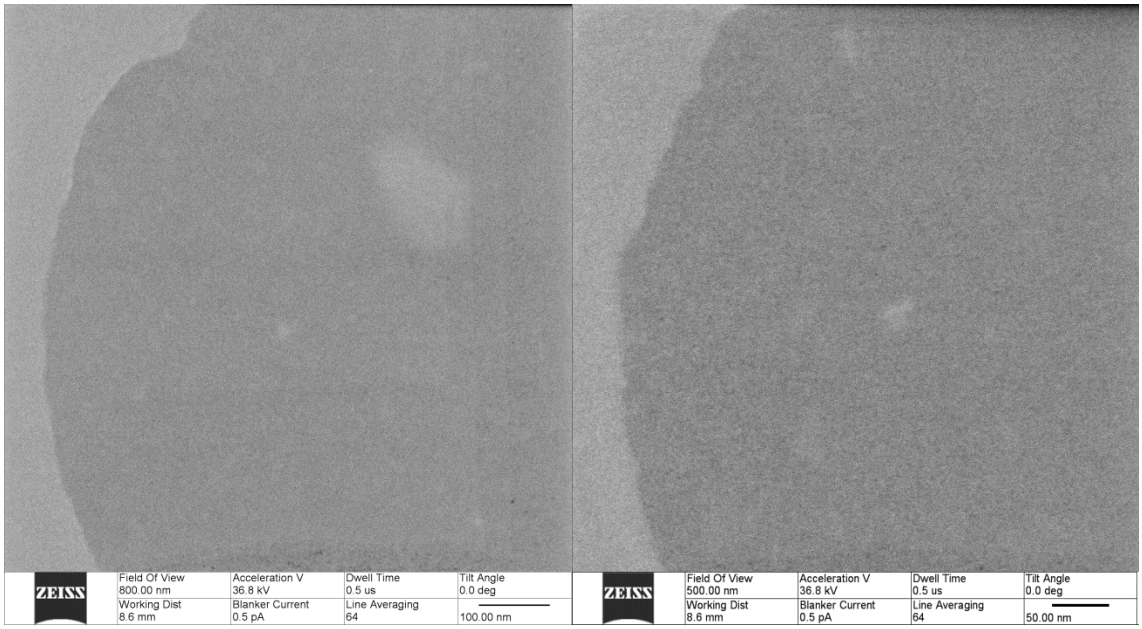

Fig.79 HIM images taken from CNMs made of mixed SAMs. Images are taken from the sample with 3-minute exchange time in 1.76 µM concentration of ODT in ethanol solution.

Nevertheless, images taken in the case of 5-minute exchange time reveal pores with maximum sizes up to 8 nm (Fig.80). Even bigger pores with higher distribution were detected in the case of 10-minute immersion time.

To verify the formation and distribution of pores for samples immersed 3- and 5-minute, CNMs were fabricated following the same recipe. The HIM observation, again, showed the same outcome at 5-minute immersion time, which was the appearance of pores up to 8 nm (Fig.81). For the 3-minute exchange time, pores were not observed, as was the case in Figure 79. As a reminder, the minimum detectable pore size is in the range of 2 nanometers. Therefore, the absence of the observation of pores at 3-minute immersion time could mean that there are smaller than 2nm pores, and it is not possible to detect them.

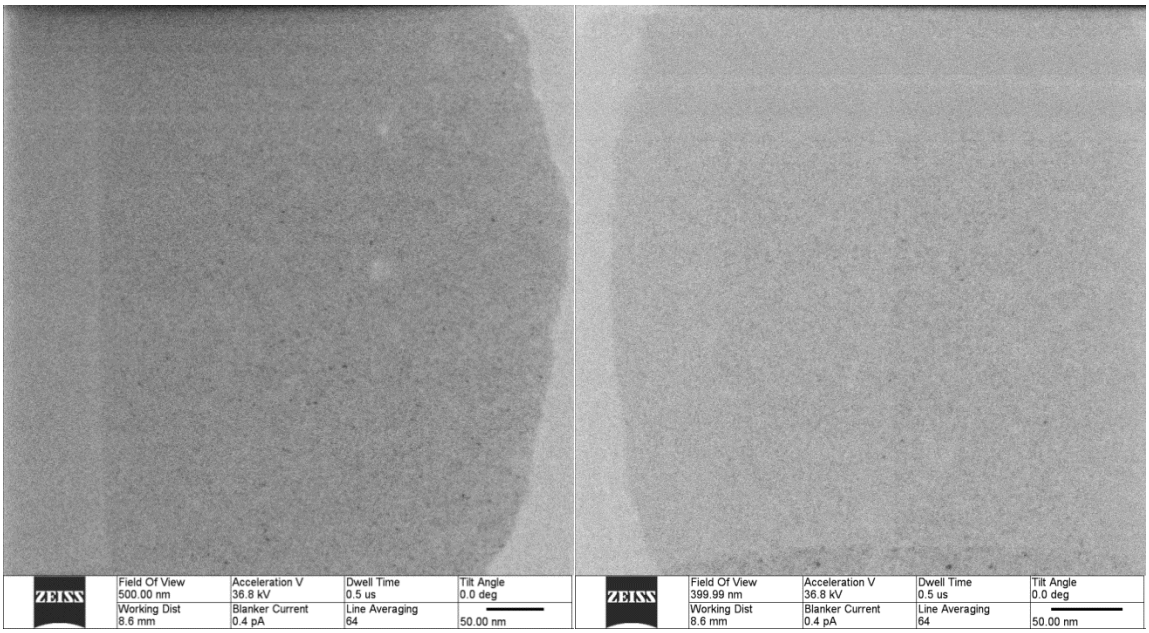

Fig.80 HIM images taken from CNMs made of mixed SAMs. Images are taken from samples with 5-minute exchange time in 1.76 µM concentration of ODT in ethanol solution.

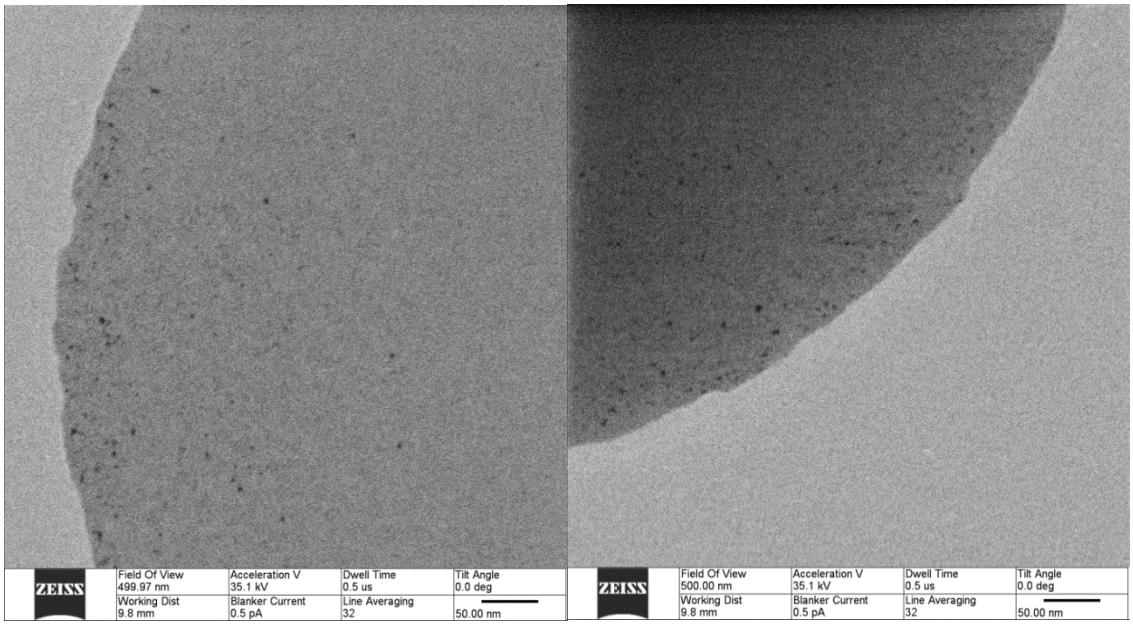

Fig.81 HIM images taken from CNMs made of mixed SAMs. Verification of the results for the sample with 5-minute immersion time (1.76 µM concentration of ODT in ethanol solution). It shows reproducible results.

To summarize, it has been shown that through the exchange of molecules in SAMs, and the subsequent irradiation of exchanged SAMs, pores in CNMs can be induced. Furthermore, the absence of pores in HIM images of NBPT-CNMs, in comparison with porous CNMs made of mixed SAMs, confirms the efficiency of the fabrication of pores with the method of mixed SAMs (Fig.82). It also confirms that pores are the result of the exchange of molecules and not defects that are formed during the fabrication of CNMs.

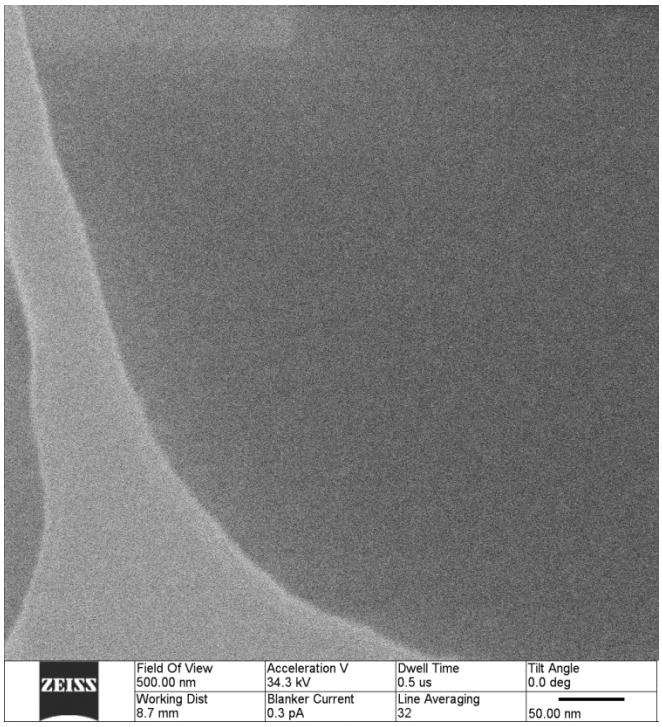

Fig.82 HIM image of an NBPT-CNM that confirms the absence of pores in comparison with CNMs made of mixed SAMs.

7.7 Gas permeation of porous CNMs made of mixed SAMs

Taking into consideration the HIM observation of the sample of mixed SAM, which was made by the immersion of an NBPT-SAM into a 1.76 μM ODT solution for 3-minute, it was decided to examine the porous CNMs for gas permeation. Therefore, NBPT-SAMs were immersed for 3-, 5-, and 10-minute into 1.76 μM ODT solution and then exposed to electron irradiation at dose of 50 mC/cm^2. Subsequently, these CNMs were transferred onto a PDMS-TFC. The CNM-PDMS composites and reference PDMS-TFC supports

were examined for gas permeation with regard to the eight gases (He, H_2, CO_2, Ar, O_2, N_2, CH_4 and C_2H_6). The results of gas permeation are depicted in Figure 83. Based on the results in Figure 83, gas permeance of porous CNMs increases when the immersion time of NBPT-SAMs in ODT solution is increased. This confirms the assumption that increasing the exchange time will create bigger pores in CNMs. From the ideal gas selectivity table, (Table 6) one can observe the reduction of ideal gas selectivity with increasing exchange times, which corresponds to the creation of bigger pores in CNMs. In addition, the gas selectivity of the sample with 3-minute immersion time is lower in comparison with the NBPT-CNM. This indicates that despite the fact that it was impossible to detect pores for the sample immersed for 3-minute in ODT solution, the 3-minute immersion is sufficient to exchange molecules and, subsequently, to induce pores in CNMs.

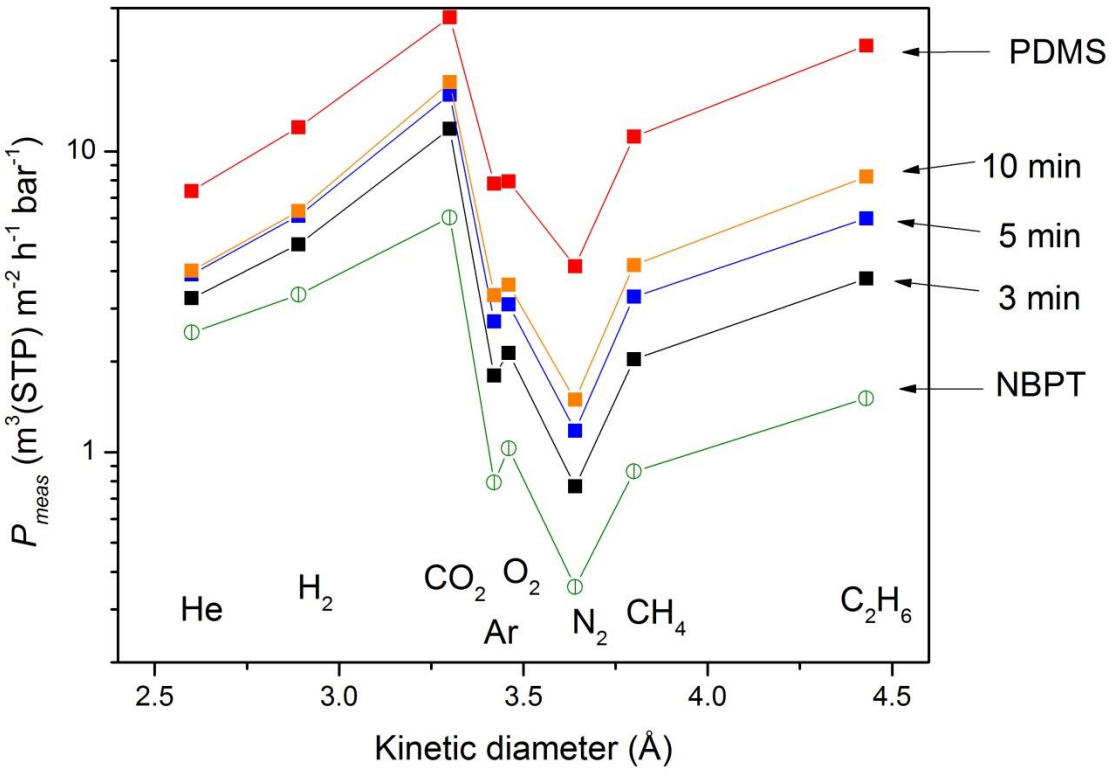

Fig.83 Gas permeation results for the samples with 3-minute, 5-minute, and 10-minute immersion times compared with the mean value of gas permeation of the NBPT-CNM samples.

Sample	H_2/N_2	H_2/CO_2	He/H_2	He/N_2	CO_2/N_2
PDMS	2,89	0.43	0,61	1,77	6.73
porous-CNM on PDMS 10 min. in ODT	4.24	0.37	0.63	2.68	11.35
porous-CNM on PDMS 5 min. in ODT	5.066	0.39	0.63	3.23	12.8
Porous-CNM on PDMS 3 min. in ODT	6.36	0.41	0.66	4.21	15.41
1NBPT-CNM on PDMS	9.35	0.55	0.74	7.006	16.89

Table 6 Ideal gas selectivity of CNMs with 3-minute, 5-minute, and 10-minute immersion times compared with an NBPT-CNM and a bare PDMS, as a reference.

The comparison of gas permeance of CNMs on a PDMS made either from different precursors (NBPT and TPT molecules) or from mixed SAMs is presented in Figure 84. The increase of measured gas permeance of CNMs on a PDMS indicates an increase of "defects/pores" in CNMs. This implies that the smallest pores that are formed by the exchange of molecules are bigger than the "natural" ones in NBPT-CNMs.

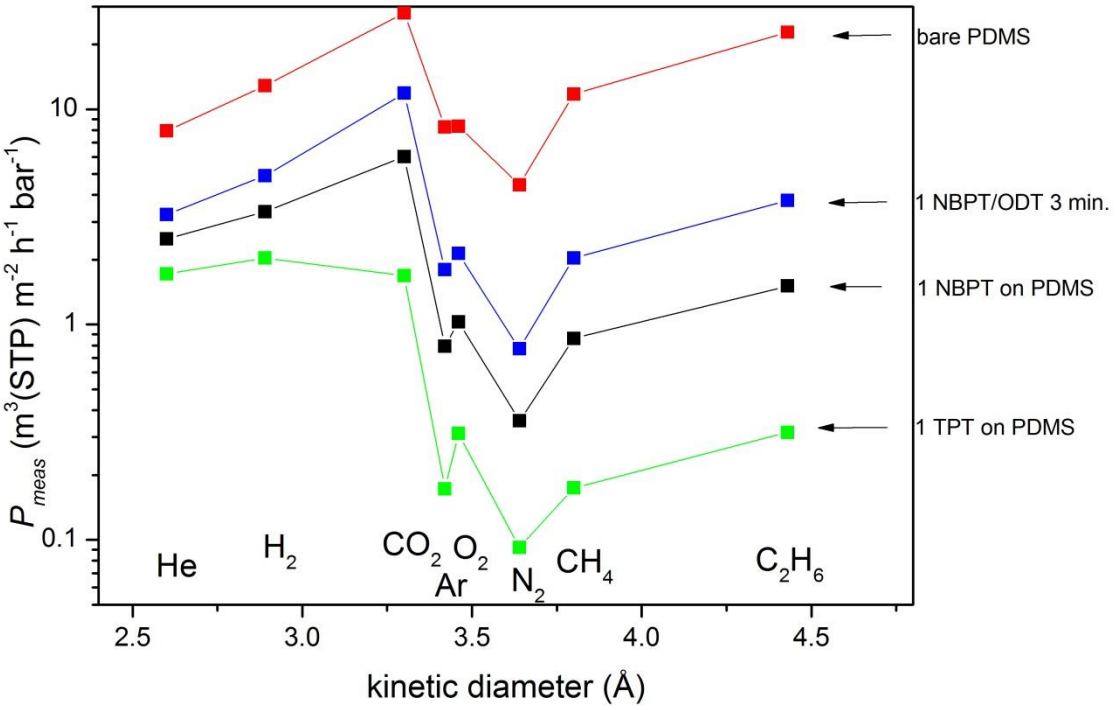

Fig.84 Comparison of gas permeance between the different types of CNMs.

Our initial goal was to try to induce small pores in CNMs for membrane gas separation, in order to improve the gas selectivity of CNMs. Apparently, the results obtained for porous CNMs indicate no better gas separation for the gases in comparison with NBPT-CNMs, which is consistent with our assumption of the origin of "molecular-sized" channels in CNMs.

It has been shown in a number of studies, which relate to the exchange of alkanethiol molecules on gold substrate, that the exchange of molecules first occurs in the more defective regions of a SAM. These are domain boundaries, where the packing of the molecules is of lower density. It is impossible to avoid defective regions for "real world" substrates, such as evaporated or sputtered gold surfaces, for which grain boundaries and varying grain orientation limit the size and quality of SAM domains. Therefore, it is assumed that the rate of exchange of molecules can be reduced by working at low temperatures instead of at room temperature [111, 112]. Furthermore, it is energetically favorable for the molecules to participate in the exchange as clusters, which means that the molecules will most likely be exchanged as groups, and therefore the induced pores will be larger. In addition, if it is possible to reach exchange of only one molecule, the cross-sectional area of that molecule will be in the range of 5Å, which is already large for separation of small gases, such as CO_2, N_2, etc. In the study of the exchange of alkanethiol monolayers on gold, electron and helium atom diffraction indicates a hexagonal lattice with an S-S distance of 5Å, which corresponds to the Au-Au (111) face lattice spacing [111, 112].

Although, the porous CNM made from the mixed SAM, and with pores in the range of 1nm, is not efficient for the separation of small gases, it can be employed for membrane gas separation processes for large gases or for DNA sequencing.

Chapter 8

Summary and Conclusion

Summary and Conclusion

The goal of this work was to study gas permeation of carbon nanomembranes (CNMs), and on the basis of the results, to determine a mechanism of gas permeation through one atom thick CNMs. Moreover, by the modification of CNMs and variation of precursor molecules, which alter the properties of self-assembled monolayers (SAMs) and hence the properties of CNMs, to enhance gas selectivity of CNMs.

Single- and multi-layer CNMs, made of four different aromatic molecules, were examined for single gas permeation measurements. Moreover, porous CNMs made from mixed SAMs were fabricated and examined for gas permeation.

For CNMs made of different precursors, the choice of precursor molecules was based on the initial interpretation of a possible mechanism of gas permeation of 4'-nitro-1,1'-biphenyl-4-thiol-CNMs (NBPT-CNMs), which assumes that a single-layer CNM shows molecular sieving-like behavior. The precursor molecules were chosen based on their polarity and length, as well as the packing density of SAMs. These properties can alter the gas permeation characteristics of a CNM. The 1-terpheny-4-thiol (TPT) and naphthalene-2-thiol (NPTH) molecules were chosen because they form densely-packed SAMs, which might vary the sizes of proposed "molecular-sized" channels through which gas permeates. The 4-(4-thiophenyl)-pyridine (TPP) molecule was chosen due to the nitrogen atom doped in phenyl ring, which may alter the gas permeation characteristics by changing the polarity of a CNM.

The results obtained for different types of CNMs showed the same gas permeation behavior, with a small difference, in the case of eight gases (He, H_2, CO_2, Ar, O_2, N_2, CH_4 and C_2H_6). For single-layer CNMs, the results indicated features that are consistent with molecular sieving-like properties. This is due to an increase of ideal gas selectivity towards small gases after the deposition of single- and multi-layer CNMs. In addition, the extraction of the intrinsic gas permeance of CNMs, from the measured permeance of a stack of CNM-polydimethylsiloxane-thin-film-composite (CNM-PDMS-TFC) membranes, shows preference for small gases (He, H_2 and CO_2) to permeate through single-layer CNMs. Therefore, it has been interpreted that single-layer CNMs show molecular-sieving like properties. The only difference in gas permeance among CNMs, made of different precursors, is the reduction of the intrinsic gas permeance of a CNM

when the thickness of a CNM is increased (Fig.48). This means by changing the precursor molecules one can vary the absolute value of the intrinsic gas permeance of a single-layer CNM.

For multi-layer CNMs, results reveal higher gas permeance for the two smallest gases (He and H_2) in comparison with the larger gases, including CO_2. This indicates a preference for small gases to permeate through multi-layer CNMs (Fig.51). However, a big drop of CO_2 gas permeance was observed in multi-layer CNMs in comparison with single-layer CNMs. This indicates that the mechanism of gas permeation is different in the case of multi-layer CNMs. As it is less likely that proposed openings or channels in single-layer CNMs are found at the exact same location in different CNM layers in multi-layer CNMs, gases will require lateral transport after passing through the vertical "openings" in a single-layer CNM. Furthermore, He and H_2 are easily condensable gases, hence, the lateral transport of gases might be described by condensation and surface flow. This mechanism is also consistent with an increase in the CO_2/N_2 gas selectivity of a PDMS-TFC by the deposition of a single-layer CNM, and the absence of an increase of selectivity after the deposition of a multi-layer CNM.

In order to clarify the mechanism of gas permeation for multi-layer CNMs, NBPT-CNMs from a single- to a four-layer were fabricated and examined for gas permeation on PDMS-TFC supports. The results for the multi-layers assume that the mechanism of gas permeation between the CNM layers, in a multi-layer, repeats and differs from the mechanism in the case of a single-layer CNM. The variation of number of layers in a multi-layer NBPT-CNM, once again, brings us to the conclusion that lateral diffusion exists in between the CNM layers in a multi-layer. This observation is consistent with the existence of lateral transport of gases in between the CNM layers in multi-layer CNMs, which might be explained by Knudsen-like diffusion.

Another goal of this work was to induce small pores in a CNM, and subsequently enhance gas selectivity of the CNM. Therefore, mixed SAMs were fabricated by an exchange of precursor molecules. In particular, aromatic NBPT molecules were exchanged with aliphatic octadecanethiol (ODT) ones in a NBPT-SAM. Afterwards, the mixed SAM was exposed to low energy electron irradiation, which induced pores at the

places where ODT molecules were detached due to their inability to resist electron irradiation.

To determine the optimal parameters for the smallest exchange of molecules, X-ray photoelectron spectroscopy (XPS) and helium ion microscopy (HIM) techniques were employed. They showed the following results: the smallest exchange was defined by the inability to detect any changes in an XPS and by no detection of pores by an HIM (3-minute immersion time in 1.76 μM concentration of ODT solution in ethanol). Afterwards, the porous CNMs were examined for gas permeation. The gas permeation results showed a difference in gas permeation characteristics in comparison with an NBPT-CNM, particularly a decrease in ideal gas selectivity in porous CNMs (Table 6). Therefore, it can be interpreted that even though XPS and HIM did not detect any changes, small pores were induced in an NBPT-CNM, which decrease the selectivity of gases. These "invisible" pores should be in the range of ∼2 nm, since pores bigger than 2 nm are possible to detect by an HIM. However, if it might be possible to obtain a minimum amount of exchange of molecules, which is 1 molecule, the cross-sectional area of one molecule would be large enough for the gases used in this work.

Nevertheless, porous CNMs, which have been fabricated by the exchange of molecules in a SAM, can be utilized for gas separation for bigger gases and for deoxyribonucleic acid (DNA) sequencing. To achieve high-quality DNA sequencing performance, the nanopores should be comparable to the DNA molecule diameter (∼1 nm for single-stranded DNA and ∼2 nm for double-stranded DNA) [117].

In the future, in order to clarify gas permeation properties of CNMs, and to precisely determine the mechanism of gas transport of CNMs, a free-standing CNM can be examined for gas permeation and new types of supports can be employed. However, the biggest disadvantage of a free-standing CNM is the high probability of ruptures and defects that can hinder reproducibility and validity of results.

Appendix

Substrates

Substrates: 300 nm thermally evaporated gold on mica substrates (Georg Albert PVD-Coatings) were employed for the preparation of self-assembled monolayers (SAMs).

Cleaning of gold substrates and glassware

The substrates were cleaned in a UV/ozone-cleaner (FHR) for 3 minutes, immersed in ethanol for at least 20 minutes, and blown dry in a stream of nitrogen. All the glassware, used for preparation of SAMs, were cleaned with freshly prepared "piranha" solution for 40 minutes: (30%) H_2O_2 : H_2SO_4 (95%) = 3 : 1.

Preparation of self-assembled monolayers

Monolayer from 4'-nitro-1,1'- biphenyl- 4- thiol (NBPT): The cleaned gold substrates were immersed in a ~ 10 mmol solution of NBPT in dry, degassed dimethylformamide (DMF) in a sealed flask under nitrogen. After 72 hours, the samples were removed from the solution, rinsed with DMF and ethanol, and blown dry with nitrogen.

Monolayer from [1'', 4', 1', 1]-terphenyl-4-thiol (TPT):

The cleaned gold substrates were immersed in ~ 1 mmol solution of TPT in dry and degassed DMF. The solution was heated at 70°C under inert atmosphere. After 24 hours, the samples were removed from the solution, rinsed with DMF and ethanol, and blown dry with nitrogen.

Monolayer from naphthalene-2-thiol (NPTH):

The cleaned gold substrates were immersed in ~ 1 mmol solution of NPTH in dry and degassed ethanol in a sealed flask at room temperature under inert atmosphere in the dark. After 24 hours, the samples were removed from the solution, rinsed with ethanol and dichloromethane, and blown dry with nitrogen

Monolayer from 4-(4-thiophenyl) pyridine (TPP):

The cleaned gold substrates were immersed in ~ 1 mmol solution of TPT in dry, degassed DMF in a sealed flask under nitrogen. After 24 hours, the samples were removed from the solution, rinsed with DMF and ethanol, and blown dry with nitrogen.

Electron irradiation, formation of CNMs

Electron irradiation of SAMs was achieved using an electron flood-gun in an ultra-high vacuum (UHV) (< 10-9 mbar, SL1000, Omicron) chamber, employing 100 eV electrons and a dose of 50 mC/cm^2. In the case of NPTH-SAM irradiation, the dose is 60 mC/cm^2. This irradiation results in a two-dimensional cross-linked CNM through dehydrogenation and recombination mechanisms.

Transfer of a CNM onto a preferable support or TEM grids

The CNMs were transferred onto a preferable support by using a protecting layer of polymethyl-methacrylate (PMMA) dissolved in chlorobenzene or ethyl acetate. Two layers of this polymer with different molecular weights, 50 K and 950 K, of an overall thickness of ~ 400 nm were spin-coated in sequence onto the CNM. Each layer was spin-coated for 40 seconds at 4000 rpm and heated on a hot plate at 90°C for 5 minutes. The underlying mica support was separated from the gold/CNM/PMMA structure by a slight dipping of one of the edges/corners of the mica/gold/CNM/PMMA sample into water. Afterwards, the gold/CNM/PMMA structure floats onto the air/water interface after separation. The sample was then transferred by using a mica piece from the water surface to I_2/KI/H_2O etching bath (1:4:10), where the gold film dissolves within 10 minutes. Then the CNM was transferred to a KI solution (1:10) for 5 minutes, and then to pure water for complete cleaning of the CNM/PMMA structure from iodine contamination. Afterwards, the CNM/PMMA structure was fished out with a preferable support by dipping it into the water and lifting it up perpendicularly to the water surface. Eventually, the support/CNM/PMMA samples were immersed into glassware filled with acetone in order to dissolve PMMA layer. The immersion time for dissolution of the PMMA layer is ~ 1 hour. Finally, the CNM on the preferable support was ready to be examined. For the gas permeation studies, samples with an area at a minimum of 1.2 cm² were fabricated.

Multi-layer CNMs were formed by mechanically stacking the layers, which were then transferred onto the preferable support as follows: CNM/PMMA structure was transferred onto another CNM, which still adhered onto the gold on mica substrate. The underlying mica support was separated as described above. Repetition of this step yielded a stack of

multilayer CNMs on the gold on mica substrate. Finally, this stack was transferred onto a preferable support.

Relative surface coverage and number of samples used in this work

NBPT-CNM

The results illustrated in Fig.30, Fig.31, and Fig.33 are based on three copies of single- and three-layer NBPT-CNMs onto a PDMS-TFC support. The obtained relative surface coverage A_{CNM}/A_{PDMS} values vary from 96.6 to 99.8 % for the three-layer CNM samples and from 82.5 to 94.7 % for the single-layer CNM samples.

TPT-CNM

The results illustrated in Fig.37 and Fig.38 are based on three copies of single- and three-layer NBPT-CNMs onto a PDMS-TFC support.

The obtained relative surface coverage A_{CNM}/A_{PDMS}values vary from 99.7 to 99.9% for the three-layer CNM samples and from 98 to 99 % for the single-layer CNM samples.

TPP-CNM

The results illustrated in Fig.45, Fig.46, and Fig.47 are based on three copies of double-layer TPP-CNMs and two copies of single-layer TPP-CNMs. The obtained relative surface coverage A_{CNM}/A_{PDMS} values vary from 66.6 to 69.3% for the single-layer CNM samples.

NPTH-CNM

The results illustrated in Fig.49 and Fig.50 are based on two copies of single-layer NPTH-CNMs, four copies of double-layer NPTH-CNMs, and two copies of three-layer TPP-CNMs. The obtained relative surface coverage A_{CNM}/A_{PDMS} values vary from 69.6 to 86.4% for the three-layer CNM samples.

The permeances P_{CNM} were averaged for all samples of the same type. The ideal gas selectivity values were calculated for each sample and averaged for all samples of the same type. Measurement uncertainties of averaged quantities were estimated by employing the standard deviation.

References

[1] S. George, S. Thomas, **Prog. Polym. Sci**., 26, 985-1017, 2001

[2] S. Sridhar, S. Bee and S. K. Bhargava, **Chem. Ind. Dig.**, 2014

[3] M. G. Buonomenna, **RSC Adv**., 3, 5694–5740, 2013

[4] P. Bernardo, E. Drioli, **Petrol. Chem**., 50, 271-282, 2010

[5] R.W. Baker, **Membrane Technology and Applications,** 2002

[6] L. Silva, A. Plaza, J. Romero, J. Sanchez, and G. M. Rios, **J. Chil. Chem. Soc**., 53, 2008

[7] P. Bernardo, G. Clarizia, **Chem. Engin. Trans.**, vol. 32, 2013

[8] R. R. Nair, H. A. Wu, P. N. Jayaram, I. V. Grigorieva, A. K. Geim, **Science**, 335 , 442, 2012

[9] J. S. Bunch, S. S. Verbridge, J. S. Alden, A. M. Van der Zande, J. M. Parpia, H. G. Craighead, P. L. McEuen, **Nano Lett.**, 8, 2458, 2008

[10] O. Leenaerts, B. Partoens, F. M. Peeters, **Appl. Phys. Lett.**,93, 193107, 2008

[11] S. P. Koenig, L. Wang, J. Pellegrino, J. S. Bunch,**Nat. Nanotechnol**., 7, 728-732, 2012

[12] H. Li, Z. Song, X. Zhang, Y. Huang, S. Li, Y. Mao, H. J. Ploehn, Y. Bao, M. Yu, **Science**, vol.342, 95-98, 2013

[13] S. C. O'Hern, C. A. Stewart, M. S. H. Boutilier, J. C. Idrobo, S. Bhaviripudi, S. K. Das, J. Kong, T. Laoui, M. Atieh, R. Karnik, **ACS Nano**, 6 , 10130, 2012

[14] G. Ozaydin-Ince, A. M. Coclite, K. K. Gleason, **Rep. Prog. Phys,**75 , 016501, 2012

[15] S. P. Koenig , L. D. Wang , J. Pellegrino , J. S. Bunch , **Nat. Nanotechnol.** 7, 728, 2012

[16] G. Gee, **Proceedings of the Royal Society of London. Series A, Mathematical and Physical Sciences**, Vol. 153, No. 878, 129-141, 1935

[17] G. Gee, E. K. Rideal, **Proceedings of the Royal Society of London. Series A, Mathematical and Physical Sciences**, 153(878), 116-128, 1935

[18] M. Ai, S. Shishatskiy, X. Zhang, C. T. Nottbohm, N. Mellech, A. Winter, H. Vieker, J. Qiu, J. Wind, K.-J. Dietz, A. Gölzhäuser, A. Beyer,**Advanced Materials**. 26(21), 3421–3426, 2014

[19] W. Adamson, A. P. Gast,**Phys. Chem. Surf.**, 6th ed., 1997

[20] A. Ulman, **Chem. Rev.**, 96 (4), 1533–1554, 1996

[21] A. Ulman, **J. Phys.: Condens. Matter**, 16, R881–R900, 2004

[22] J. C. Love , L. A. Estroff , J. K. Kriebel , R. G. Nuzzo , G. M. Whitesides, **Chem. Rev**., 105 (4), 1103–1170, 2005

[23] G. E.Poirier, E.D. Pylant, **Science**, 272, 1145, 1996

[24] R. G. Nuzzo, D. L. Allara, **J. Am. Chem. Soc**., 105, 4481, 1983

[25] M. D. Porter, T.B. Bright, D.L. Allara, C.E.D. Chidsey, **J. Am. Chem. Soc.**, 109, 3559. 1987

[26] L.H. Dubois, R.G. Nuzzo, **Annu. Rev. Phys. Chem**., 43, 437, 1992

[27] C. D. Bain, J. Evall, G. M. Whitesides, **J. Am. Chem. Soc.,**111, 7155, 1989

[28] C. D. Bain, G. M. Whitesides, **Science,**240, 62, 1988

[29] H. A. Biebuyck, C. D. Bain, G. M. Whitesides, **Langmuir,** 10, 1825, 1994

[30] P. E. Laibinis, G. M. Whitesides, D. L. Allara, Y. T. Tao, A. N. Parikh, R. G. Nuzzo, **J. Am. Chem. Soc**., 113, 7152, 1991

[31] L. H. Dubois, B. R. Zegarski, R. G. Nuzzo, **J. Chem. Phys**., 98, 678, 1993

[32] M. M. Walczak, C. Chung, S. M. Stole, C. A. Widrig, M. D. Porter, **J. Am. Chem. Soc.**, 113, 2370, 1991

[33] P. Fenter, P. Eisenberger, J. Li, N. Camillone, S. Bernasek, G. Scoles, T. A. Ramanarayanan, K. S. Liang, **Langmuir**, 7, 2013. 1991

[34] J. C. Love, D. B. Wolfe, R. Haasch, M. L. Chabinyc, K. E. Paul, G. M. Whitesides, R. G. Nuzzo, **J. Am. Chem. Soc.**,125, 2597, 2003

[35] A. Carvalho, M. Geissler, H. Schmid, B. Micel, E. Delamarche, **Langmuir**, 18, 2406, 2002

[36] Z. Li, S. C. Chang, R. S. Williams, **Langmuir**, 19, 6744, 2003

[37] N. Muskal, I. Turyan, D. J. Mandler, **Electroanal. Chem**., 409, 131, 1996

[38] M. Himmelhaus, F. Eisert, M. Buck, M. Grunze, **J. Phys. Chem. B**, 104, 576, 2000

[39] S. Frey, V. Stadler, K. Heister, W. Eck, M. Zharnikov, M. Grunze, B. Zeysing, A. Terfort, **Langmuir**, 17, 2408, 2001

[40] A. Turchanin, A. Gölzhäuser, **Progress in Surface Science,** 87, 108–162, 2012

[41] L. Kankate, A. Turchanin, A. Gölzhäuser, **Langmuir**, 25, 10435–10438, 2009

[42] X.L. Fan, Q. Chi, C. Liu, W.M. Lau, **J. Phys. Chem. C**, 116, 1002–1011, 2012

[43] A. Cossaro, R. Mazzarello, R. Rousseau, L. Casalis, A. Verdini, A. Kohlmeyer, L. Floreano, S. Scandolo, A. Morgante, M.L. Klein, G. Scoles, **Science**, 321, 943–946, 2008

[44] A. Chaudhuri, T.J. Lerotholi, D.C. Jackson, D.P. Woodruff, V. Dhanak, **Phys.Rev. Letters**, 102, 12610, 2009

[45] E. Sabatani, J. Cohenboulakia, M. Bruening, I. Rubinstein, **Langmuir,** 9, 2974–2981, 1993

[46] C.D. Bain, E.B. Troughton, Y.T. Tao, J. Evall, G.M. Whitesides, R.G. Nuzzo, **J. Am. Chem. Soc.,** 111, 321–335, 1989

[47] R.G. Nuzzo, B.R. Zegarski, L.H. Dubois, **J. Am. Chem. Soc.**, 109, 733–740, 1987

[48] T.Y.B. Leung, P. Schwartz, G. Scoles, F. Schreiber, A. Ulman, **Surface Science**, 458, 34–52, 2000

[49] P. Cyganik, M. Buck, **J. Amer. Chem. Soc.,** 126, 5960–5961, 2004

[50] W. Azzam, C. Fuxen, A. Birkner, H.T. Rong, M. Buck, C. Wöll, **Langmuir**, 19, 4958–4968, 2003

[51] T. Ishida, W. Mizutani, U. Akiba, K. Umemura, A. Inoue, N. Choi, M. Fujihira, H. Tokumoto, **J. Phys. Chem. B**, 103, 1686–1690, 1999

[52] V. Batz, M.A. Schneeweiss, D. Kramer, H. Hagenstrom, D.M. Kolb, D. Mandler, **J. Electroanal. Chem.,** 491, 55–68, 2000

[53] P. Cyganik, M. Buck, T. Strunskus, A. Shaporenko, J. Wilton-Ely, M. Zharnikov, C. Wöll, **J. Amer. Chem. Soc.**, 128, 13868–13878, 2006

[54] G.J.J. Su, R. Aguilar-Sanchez, Z.H. Li, I. Pobelov, M. Homberger, U. Simon, T. Wandlowski, **Chem.phys.chem.**, 8, 1037–1048, 2007

[55] B. Lussem, L. Muller-Meskamp, S. Karthauser, R. Waser, M. Homberger, U. Simon, **Langmuir**, 22, 3021–3027, 2006

[56] V.V. Korolkov, S. Allen, C.J. Roberts, S.J.B. Tendler, J. Phys. Chem. C, 115, 14899–14906, 2011

[57] G.H. Yang, Y.L. Qian, C. Engtrakul, L.R. Sita, G.Y. Liu, **J. Phys. Chem. B**, 104, 9059–9062, 2000

[58] W. Azzam, P. Cyganik, G. Witte, M. Buck, C. Wöll, **Langmuir**, 19, 8262–8270, 2003

[59] H.J. Himmel, A. Terfort, C. Wöll, **J. Amer. Chem. Soc.**, 120, 12069–12074, 1998

[60] W. Geyer, V. Stadler, W. Eck, M. Zharnikov, A. Gölzhäuser, M. Grunze, **Appl. Phys. Lett.**, 75, 2401–2403, 1999

[61] K. Heister, M. Zharnikov, M. Grunze, L.S.O. Johansson, **J. Phys. Chem. B**, 105, 4058–4061, 2001

[62] H.T. Rong, S. Frey, Y.J. Yang, M. Zharnikov, M. Buck, M. Wühn, C. Wöll, G. Helmchen, **Langmuir**, 17, 1582–1593, 2001

[63] A. Shaporenko, K. Adlkofer, L.S.O. Johansson, A. Ulman, M. Grunze, M. Tanaka, M. Zharnikov, **J. Phys. Chem. B**, 108, 17964–17972, 2004

[64] H. Hamoudi, P. Kao, A. Nefedov, D.L. Allara, M. Zharnikov**, Beilstein J. Nanotech.**, 3, 12–24, 2012

[65] J.F. Kang, A. Ulman, S. Liao, R. Jordan, G.H. Yang, G.Y. Liu, **Langmuir**, 17, 95–106, 2001

[66] W. Azzam, B.I. Wehner, R.A. Fischer, A. Terfort, C. Wöll, **Langmuir**, 18, 7766–7769, 2002

[67] W. Azzam, A. Bashir, A. Terfort, T. Strunskus, C. Wöll, **Langmuir**, 22, 3647–3655, 2006

[68] S. Stoycheva, M. Himmelhaus, J. Fick, A. Kornviakov, M. Grunze, A. Ulman, **Langmuir**, 22, 4170–4178, 2006

[69] D. Käfer, G. Witte, P. Cyganik, A. Terfort, C. Wöll, J. Amer. Chem. Soc., 128, 1723–1732, 2006

[70] A. Turchanin, D. Käfer, M. El-Desawy, C. Wöll, G. Witte, A. Gölzhäuser, **Langmuir**, 25, 7342–7352, 2009

[71] Q. Sun, A. Selloni, G. Scoles, **J. Phys. Chem. B**, 110, 3493–3498, 2006

[72] G. Heimel, L. Romaner, J.L. Bredas, E. Zojer, **Langmuir**, 24, 474–482, 2008

[73] G. Heimel, F. Rissner, E. Zojer, **Advanced Materials**, 22, 2494–2513, 2010

[74] A.M. Track, F. Rissner, G. Heimel, L. Romaner, D. Käfer, A. Bashir, G.M. Rangger, O.T. Hofmann, T. Bucko, G. Witte, E. Zojer, **J. Phys. Chem. C**, 114, 2677–2684, 2010

[75] S. Krämer, R.R. Fuierer, C.B. Gorman, **Chem. Rev.,** 103, 4367–4418, 2003

[76] R.D. Piner, J. Zhu, F. Xu, S.H. Hong, C.A. Mirkin, **Science**, 283, 661–663, 1999

[77] A. Turchanin, M. Schnietz, M. El-Desawy, H.H. Solak, C. David, A. Gölzhäuser, **Small**, 3, 2114–2119, 2007

[78] C.S. Dulcey, J.H. Georger, V. Krauthamer, D.A. Stenger, T.L. Fare, J.M. Calvert, **Science**, 252, 551–554, 1991

[79] W.J. Dressick, C.S. Dulcey, S.L. Brandow, H. Witschi, P.F. Neeley, **J. Vac. Sci. Technol. A**, 17, 1432–1440, 1999

[80] M.J. Lercel, G.F. Redinbo, F.D. Pardo, M. Rooks, R.C. Tiberio, P. Simpson, H.G. Craighead, C.W. Sheen, A.N. Parikh, D.L. Allara, **J. Vac. Sci. Technol. B**, 12, 3663–3667, 1994

[81] A. Gölzhäuser, W. Geyer, V. Stadler, W. Eck, M. Grunze, K. Edinger, T. Weimann, P. Hinze, **J. Vac. Sci. Technol. B**, 18, 3414–3418, 2000

[82] E.T. Ada, L. Hanley, S. Etchin, J. Melngailis, W.J. Dressick, M.S. Chen, J.M. Calvert, **J. Vac. Sci. Technol. B,** 13, 2189–2196, 1995

[83] W. Eck, V. Stadler, W. Geyer, M. Zharnikov, A. Gölzhäuser, M. Grunze, **Advanced Materials**, 12, 805–808, 2000

[84] S.A.A. Ahmad, L.S. Wong, E. Ul-Haq, J.K. Hobbs, G.J. Leggett, J. Micklefield, **J.Amer. Chem. Soc.**, 131, 1513–1522, 2009

[85] N. Ballav, H. Thomas, T. Winkler, A. Terfort, M. Zharnikov, **Angew. Chemi. Int. Ed.**, 48, 5833–5836, 2009

[86] L. Kankate, U. Werner, A. Turchanin, A. Gölzhäuser, H. Grossmann, R. Tampe, **Biointerphases**, 5, 30–36, 2010

[87] M. Zharnikov, W. Geyer, A. Gölzhäuser, S. Frey, M. Grunze, **Phys. Chem. Chem. Phys**., 1, 3163–3171, 1999

[88] A. Gölzhäuser, W. Eck, W. Geyer, V. Stadler, T. Weimann, P. Hinze, M. Grunze, **Advanced Materials**, 13, 806–809, 2001

[89] A. Turchanin, M. El-Desawy, A. Gölzhäuser, **Applied Physics Letters**, 90, 053102, 2007

[90] P. Angelova, H. Vieker, N.-E. Weber, D. Matei, O. Reimer, I. Meier, S. Kurasch, J. Biskupek, D. Lorbach, K. Wunderlich, L. Chen, A. Terfort, M. Klapper, K. Müllen, U. Kaiser, A.Golzhauser, A. Turchanin, **ACS Nano**, 7, 6489–6497, 2013

[91] A. Turchanin, A. Beyer, C. Nottbohm, X. Zhang, R. Stosch, A. Sologubenko, J. Mayer, P. Hinze, T. Weimann, A. Gölzhäuser, **Advanced Materials**, 21, 1233–1237, 2009

[92] X. Zhang, A. Beyer, A. Gölzhäuser, **Beilstein J. Nanotechnology**, 2, 826–833, 2011

[93] A. Turchanin, D. Weber, M. Büenfeld, C. Kisielowski, M.V. Fistul, K.B. Efetov, T. Weimann, R. Stosch, J. Mayer, A. Gölzhäuser, **ACS Nano**, 5, 3896–3904, 2011

[94] C.T. Nottbohm, A. Turchanin, A. Beyer, R. Stosch, A. Gölzhäuser, **Small,** 7, 874–883, 2011

[95] A. Beyer, A. Godt, I. Amin, C.T. Nottbohm, C. Schmidt, J. Zhao, A. Gölzhäuser, **Phys. Chem. Chem. Phys.**, 10, 7233–7238, 2008

[96] A. Turchanin, A. Tinazli, M. El-Desawy, H. Großmann, M. Schnietz, H.H. Solak, R. Tampé, A. Gölzhäuser, **Advanced Materials**, 20, 471–477, 2008

[97] Universal curve:
http://www.phys.au.dk/~philip/pictures/physicsfigures/physicsfigures.html

[98]Y. Hu, Z. Li, H. Li, Y. Liu, S. Song, **RSC Adv.**, 6, 14859–14867, 2016

[99] J. Morgan, J. Notte,R. Hill, B. Ward, **Microsc. Today**, 22, 2006

[100] J. Notte, B. Ward, N. Economou, R. Hill, R. Percival, L. Farkas, S. McVey, **AIP Conference Proceedings**, vol. 931, 489–496, 2007

[101] D. Cohen-Tanugi, N. Yao, **J. Appl. Phys.**, 104, 063504, 2008

[102] A. Beyer, H. Vieker, R. Klett, H. Meyer zu Theenhausen, P. Angelova, A. Gölzhäuser, **Beilstein J. Nanotechnology**,6, 1712–1720, 2015

[103] A. M. Shishatskii, Y. P. Yampolskii, K.-V. Peinemann, **J. Membr. Sci.**, 112, 275-285, 1996

[104] W. Yave, A. Car, J. Wind, K. V. Peinemann, **Nanotech**, 21, 395301, 2010.

[105] J. W. Zhou, D. A. Khodakov, A. V. Ellis, N. H. Voelcker, **Electrophoresis**, 33, 89-104, 2012

[106] P. Kofinas, R. E. Cohen , A. F. Halasa, **Polymer**,35, 1229, 1994

[107] Z. Terzopoulou, G. Z. Kyzas, D. N. Bikiaris, **Materials**, 8, 652-683, 2015

[108] C. Ogata, M. Koinuma, K. Hatakeyama, H. Tateishi, M. ZainulAsrori, T. Taniguchi, A. Funatsu, Y. Matsumoto,**Sci. rep.**, 43647, 2014

[109] M. T. Cygan, T. D. Dunbar, J. J. Arnold, L. A. Bumm, N. F. Shedlock, T. P. Burgin, L.Jones II, D. L. Allara, J. M. Tour, P. S. Weiss, **J. Am. Chem**. Soc.120, 2721- 2732, 1998

[110] S. Turgman-Cohen, M. B. Smith, D. A. Fischer, P. K. Kilpatrick, J. Genzer, **Langmuir**, 25 (11), 6260-6269, 2009

[111] R. G. Chapman, E. Ostuni, L. Yan, G. M. Whitesides, **Langmuir**, 16, 6927-6936, 2000

[112] G. G. Baralia, A.-S. Duwez, B. Nysten, A. M. Jonas, **Langmuir**, 21, 6825-6829, 2005

[113] D.M.Collard, M. A. Fox,**Langmuir**, 7, 1192-1197, 1991

[114] Zeiss. Carl Zeiss Press Release: New Benchmark http://www.smt.zeiss.com/C1256A770030BCE0/WebViewAllE/F4BF4E46C9379912C1257508002B9F7C

[115] R. Hill, J. Notte, B. Ward, **Phys. Procedia**, 1, 135–141, 2008

[116] X. Zhang. C. Neumann, P.Angelova, A. Beyer, A. Gölzhäuser, **Langmuir,** 30, 8221−8227, 2014

[117] Z. Liu, Y. Wang, T. Deng, Q. Chen, **J. Nanomater.**, 2016

Abbreviations

2D – Two-dimensional

AFM – Atomic force microscope

BE – Binding energy

BPT – 1,1'-biphenyl-4-thiol

CNM – Carbon nanomembrane

DNA – Deoxyribonucleic acid DNA

DPN – Dip-Pen-Nanolithography

GO – Graphene oxide

HIM – Helium ion Microscopy

NBPT – 4'-nitro-1,1'-biphenyl-4-thiol

NPTH – Naphthalene-2-thiol

ODT – Octadecanethiol

PAN – Polyacrylonitrile

PDMS-TFC – Polydimethylsiloxane thin film composite

PMMA – Polymethyl-methacrylate

PTMSP-TFC – poly(1-trimethylsilyl-1-propyne)

SAM – Self-assembled monolayer

SEM – Scanning electron microscopy

TEM – Transmission electron microscopy

TPP – 4-(4-thiophenyl)pyridine

TPT – 1-terpheny-4-thiol

UHV – Ultra-high vacuum

XPS – X-ray photoelectron spectroscopy

List of figures and tables

Acknowledgements

First of all, I would like to thank my advisor Prof. Dr. Armin Gölzhäuser for the chance to work and to pursue my PhD study in his group. I am very grateful for his guidance and support during my stay in the group. He was always supportive with his ideas and vision in science and helped a lot with his constructive criticism.

I would like, particularly, to thank my co-advisor PD Dr. André Beyer for his precise instructions in my experiments, support in data analysis, and his patience in supervising me. I would like also to thank Dr. Min Ai, who guided me during my first months in the group. I also want to thank Dr. Berthold Vökel for his guidance in using different equipment and assistance in solving problems. I am very thankful to Dr. Polina Angelova for her suggestions and help in my experiments as a chemist.

I want to thank Paul Penner, Emanuel Marschewski, Florian Paneff for lots of discussions and advices in our office. Big thanks to the rest of the group, particularly Henning Vieker, Natalie Frese, and Daniel Emmrich in their help of HIM imaging of the samples, Nils-Eike Weber and Andreas Winter for the guidance in the laboratory, particularly to maintain the XPS, Dr. Xianghui Zhang for discussions and constructive criticism. It was always nice to work with all of them.

I especially want to thank Ursula Lorentzen and Karin Lacey for their help with all the administrative paperwork and support in everything.

Special thanks to the collaborators from the Institute of Polymer Research at Helmholtz-Zentrum, Geesthacht, particularly Dr. Muntazim Khan and Dr. Sergey Shishatskiy. Gas permeation experiments were possible only with their help.

I would like to thank my cousin Aram Taslagyan, alumnus from the University of California, Berkeley, for a detailed correction of the English grammar of my thesis.

Finally, I want to thank my parents, who were always encouraging and motivating me in my decisions, for their patience and support through all these years. In addition, I am thankful to all my friends, who were always there when I needed advice and support.